Florida State University Libraries

Practical Applications of Excited State Proton Transfer: From Super Acidity and Enantioenrichment to White Light Emission and Sensors

Suliman Al-Hemali Ayad

FLORIDA STATE UNIVERSITY

COLLEGE OF ARTS AND SCIENCES

PRACTICAL APPLICATIONS OF EXCITED STATE PROTON TRANSFER: FROM SUPER

ACIDITY AND ENANTIOENRICHMENT TO WHITE LIGHT EMISSION AND SENSORS

By

SULIMAN AL-HEMALI AYAD

A Dissertation submitted to the
Department of Chemistry and Biochemistry
in partial fulfillment of the
requirements for the degree of
Doctor of Philosophy

2020

Suliman Al-Hemali Ayad defended this dissertation on March 31st, 2020. The members of the supervisory committee were:

Kenneth Hanson
Professor Directing Dissertation

Steven Lenhert
University Representative

Igor Alabugin
Committee Member

Thomas Albrecht-Schmitt
Committee Member

The Graduate School has verified and approved the above-named committee members and certifies that the dissertation has been approved in accordance with university requirements.

Dedicated to my Mother and Father
And to the long line of educators that came before me
I strive to continue our family legacy

TABLE OF CONTENTS

LIST OF TABLES

LIST OF FIGURES

ABSTRACT

In the present work, excited state proton transfer (ESPT) was investigated for a variety of applications with two main areas of focus; its excited state super acidity and its uniquely large apparent Stokes shift. When a molecule absorbs a photon in enters an excited state in which the electron density of the molecule rearranges. In some molecules this electron density shift occurs away from a proton which causes the proton to become more labile and therefore more acidic. The increased acidity allows for proton transfer to occur either inter or intramolecularly. In the first chapter of this work intermolecular ESPT was used to enantioselectively protonate a silyl enol ether to generate a chiral cyclic ketone. Utilizing the axial chirality of Br-VANOL coupled with its ESPT capable aromatic alcohols, 1-phenyl-2-(trimethylsiloxy)cyclohexene was protonated to yield an enantiomeric excess (ee) of 35%. This property was extended to a variety of other silyl enol ethers to demonstrate the versatility of this method. During our investigations into this system we attempted to use BINOL, a compound with similar axial chirality to VANOL, but observed no ee under the same conditions. Later this was found to be the result of an excited state racemization process that occurs after BINOLs proton transfer.

Further attempting to use ESPT to influence the chirality of atropisomeric compounds we coupled chiral auxiliary groups to BINOL then irradiated the molecule to induce the racemization event which was detrimental to our last system mentioned above. In the presence of a suitable proton acceptor irradiating BINOL causes ESPT to occur, and BINOL enters a planar excited state. From this planar excited state BINOL relaxes then rotates one direction or the other as it reenters the ground state. The addition of a chiral auxiliary group induces a preference for rotating in one direction over the other initially resulting in ee of 25% for our prototypical system. Perhaps the most interesting aspect of this work was that the ee of the molecule was found to be entirely dependent on the nature of the chiral auxiliary group, and that starting from any other ee of BINOL coupled to the same chiral auxiliary group yields the same ee. These results indicate the presence of a photostationary equilibrium ee. Changing the chiral auxiliary group to Boc protected phenylglycine yielded an ee of up to 63%. After the generation of the enantioenriched compound the chiral auxiliary group is easily cleaved by LiOH at room temperature to yield pure enantioenriched BINOL.

The second half of this work is focused on the unique photophysical properties of ESIPT (excited state intramolecular proton transfer), most notably its potentially large apparent Stokes shift. When a fluorophore undergoes ESIPT the electron density shifts away from the proton containing moiety and towards a proton accepting moiety. The result of this reorganization is that the fluorophores tautomerizes into a "keto" form. From this keto state it may relax to the ground state by emitting a photon which can be red shifted by hundreds of nanometers which presents as an apparent stokes shift. Our first application of this feature was to utilize ESIPT dyes in a metal organic framework (MOF) to generate different colored emissive materials. By varying ratios of the R, G, and B linkers we were able to create a variety of different colored emissive materials including several shades of white with high color rendering index.

The final chapter of this work utilizes this same ESIPT apparent stokes shift as a highly versatile sensor for detection of metal ions and hydrazine. By designing a fluorophore with a chelating moiety, we observed large spectral shifts when metal ions were successfully bound to the fluorophore. The changes to the photophysical properties was found to be dependent upon which M^{II} ion was bound. Most notably Zn^{II} was found to increase the quantum yield (QY) of this molecule to a maximum of 60%. When the ESIPT active positions were protected the emission was turned off, allowing it to then be turned back on with a suitable cleaving agent. This allowed for the rapid visual detection of hydrazine.

CHAPTER 1

INTRODUCTION

1.1   Excited State Acidity

Proton transfer is among the most fundamental chemical transformations and is observed in everything from the hydrogen bonding of water to the cellular respiration of plants and animals. The ease of proton transfer is referred to as acidity. By the Brønsted-Lowry understanding of acidity, acids are proton donors and bases are proton acceptors[1]. The less covalent/more ionic character a bond between a proton and its parent molecule has the more acidic it is. This is commonly quantified by the acid dissociation constant K_a of the molecule. Acidity is typically studied with molecules in their ground state, however under specific circumstances molecules may enter an excited state with increased acidity.

The absorption and emission of light by organic molecules is a well understood process. When a photon of sufficient energy contacts a molecule, it can be absorbed by the molecule by promoting an electron from the ground state to a higher energy excited state. From this excited state the molecule must lose the newly gained energy through one or more relaxation mechanisms, such as thermalization, vibrational relaxation, intersystem crossing, energy transfer to another molecule, tautomerization, photon emission and others. These molecular excited states typically cause reorganization of the electronic structure of the molecule as the molecular orbitals rearrange to accommodate the new higher energy electron. For some molecules this means that the net electron density shifts from one side of the molecule to the other. This shift can weaken covalent bonds between protons and highly electronegative atoms thereby increasing the acidity of that proton.[2] The newly acidic proton is now capable of being transferred to either a different nearby molecule or to a different position on the same molecule. These two processes are known as excited state intermolecular proton transfer (ESPT) and excited state intramolecular proton transfer (ESIPT) respectively.

1.1.1   Excited State Intermolecular Proton Transfer

Excited State Intermolecular Proton Transfer occurs most commonly between aromatic alcohols and other molecules nearby which have a lone pair available to accept the proton. When the aromatic alcohol absorbs a photon an n-π^* electronic transition occurs between an electronegative atom lone pair and the aromatic ring. This causes the electron density to shift away from the alcohol as seen in Figure 1.1. The result is a weakened O-H bond which can be up to 13 orders of magnitude more acidic than in the ground state[3]. Typical proton acceptors may be
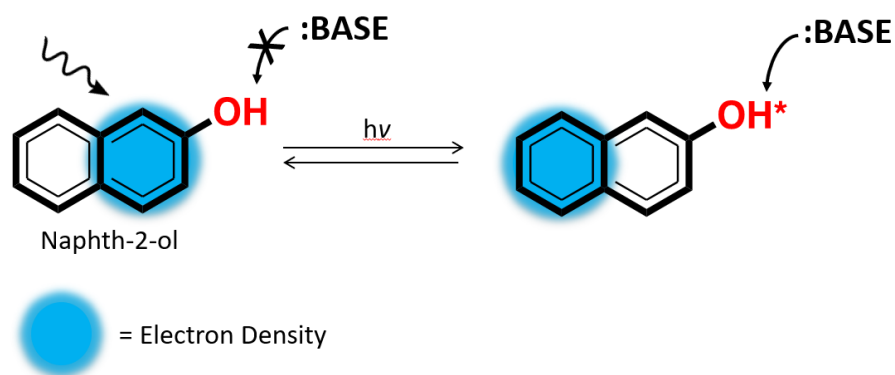
Figure 1.1 Generalized reaction scheme depicting the excited state intermolecular proton transfer reaction of Naphth-2-ol. Photon absorption causes an electron density shift away from the oxygen resulting in a proton labile enough to be removed by base in solution.

hydrogen bonded solvent molecules, organic bases, or aromatic moieties with electronegative atoms present.

After proton transfer the ESPT molecule undergoes a rapid tautomerization event to produce what is referred to as the keto form of the molecule. The excited state keto form is a lower energy species than the excited state enol. From the excited keto state either a radiative (emission) or nonradiative relaxation process returns the molecule to its ground state keto form. The keto ground state is necessarily more basic than the excited state keto form as the electron density has shifted back towards the aromatic oxygen. Proton transfer from the environment typically returns the ESPT molecule to its ground state enol form, however if the proton was consumed by some non-reversible process the molecule may persist in its anionic form.

It is important to note that proton transfer from the ESPT molecule to its environment is an energetically unfavorable process in the ground state however the proton donor and acceptor

often exist as a hydrogen bonded pair. After photoexcitation the enol form of the molecule may become the higher energy species and conversion to the keto form may proceed energetically downhill. The relative energies of the tautomers is conditional upon solvent, pH, hydrogen bonding, and other molecular interactions.

1.1.2 Excited State Intramolecular Proton Transfer
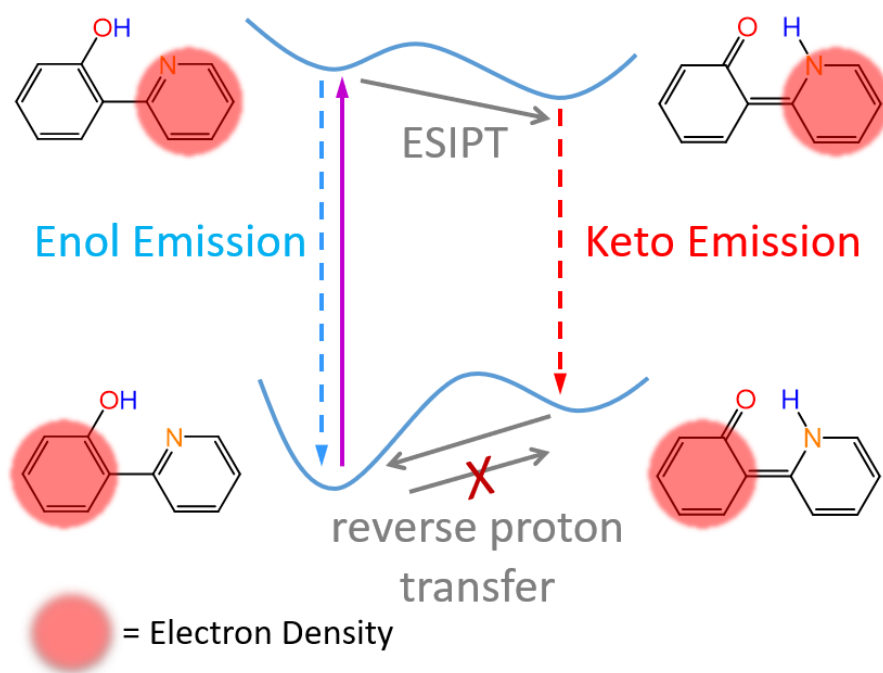
Figure 1.2 Generalized reaction scheme for the Förster cycle depicting the main photophysical processes in the four-step cycle. Dashed lines represent emissive processes.

Excited state intramolecular proton transfer proceeds in largely the same way as the intermolecular process with the exception that the proton is transferred within the ESIPT molecule typically between hydrogen bonded electronegative atoms (oxygen or nitrogen). Due to the proximity of the donor and acceptor pair the proton transfer process is particularly fast (100 fs)[4-6] The rapid proton transfer between intramolecular moieties gives rise to a unique excitation-relaxation process known as the Förster cycle.

The molecule begins in the enol ground state until photoexcitation induces the electron density shift away from the proton donor and towards the proton acceptor generating the enol

excited state. The hydrogen bonded proton is transferred between the electronegative atoms forming the excited state keto tautomer. Relaxation yields the ground state keto form until reverse proton transfer returns the molecule to its original state.

A particularly interesting effect of the Förster cycle is the dual fluorescence of ESIPT dyes. Upon excitation of a typical dye molecule an electron is promoted to some singlet excited state relative to the energy of the incident photon. From this state the electron rapidly relaxes to the lowest energy excited state of the same multiplicity through a process known as internal conversion as outlined by Kasha in his 1950 paper[7]. The result of this relaxation is a longer wavelength photon emission (bathochromic or red shift). The loss of energy and longer wavelength emission band maxima relative to the absorption band maxima are known as the Stokes shift[8]. Typically, the energy loss between absorption and emission results in a Stokes shift of ~20-50nm. However, for ESIPT molecules the proton transfer event results in a much lower energy keto excited state before emission occurs. When emission occurs the energy gap between the excited and ground state keto tautomer can be much smaller than the enol form. Smaller
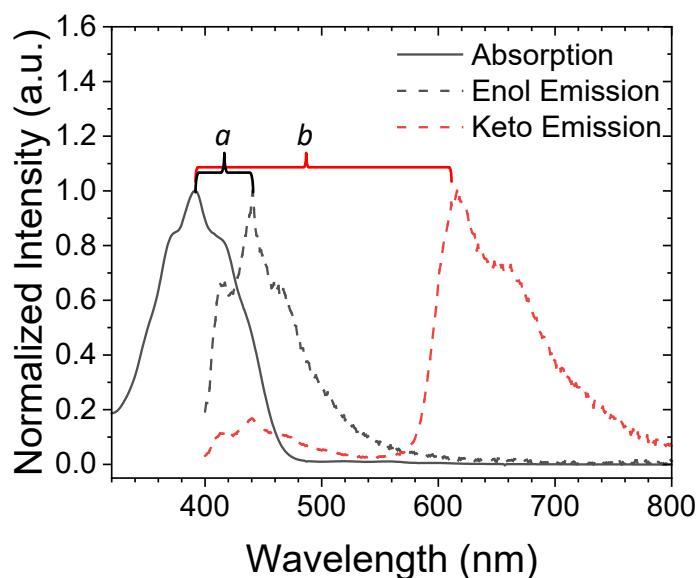
Figure 1.3 Normalized absorption (solid line) and emission (dashed lines) spectra of an ESIPT dye with inhibited proton transfer (black, enol emission only) and uninhibited proton transfer (red, keto emission). a) Stokes shift between absorption and enol emission of the protonated excited state dye and b) Apparent Stokes shift between absorption and keto emission of the deprotonated excited state species.

energy gaps result in lower energy photons which means the resultant photon will be of a much longer wavelength than if the molecule had emitted from the enol excited state. Because there is a possibility of emission from both the enol excited state and the keto excited state many ESIPT dyes exhibit dual fluorescence[5]. A typical spectrum may contain a peak with a normal Stokes shift and a peak with a much larger apparent Stokes shift.

There is a common nomenclature misconception in relation to the low-energy emission features of ESIPT dyes. Stokes shift is commonly used to refer to the gap between absorption and emission maxima, however, the original intention of the phrase refers to the difference between band maxima of the same electronic transition.[8] The reorganization of the molecule upon tautomerization means that it is emitting through a different electronic transition than it absorbed from and as a result it is no longer a Stokes shift. Throughout this work the difference between enol absorption and keto emission will be referred to as an "apparent Stokes shift" to differentiate from the original intention of the phrase.

1.2   A Brief History of Excited State Proton Transfer

While ground state proton transfer has been studied for more than two centuries, excited state proton transfer (ESPT) is a relatively young area of research.[5] The photophysical symptoms of ESPT were first reported in the 1930s by Weber who observed that for 1-naphthylamine-4-sulfonate in water, there was a pH dependent change in the fluorescence spectrum, but not the absorption spectrum.[9] Nearly 20 years later Förster was investigating the relationship between the newly formulated principles of quantum mechanics and chemistry. Through the course of this research Förster et al discovered that when 2-naphthol was irradiated in a solution of pH 2-3 the observed emission matched that of the dissociated anion despite the relatively acidic environment.[10] It was in 1950 that he definitively assigned this unusual behavior to the ESPT mechanism that bears his name.[11]

Since then, and in particular the last few decades, there has been increased interest in ESPT with applications in lasers, bio-imaging, fluorescent sensors, energy storage devices, and others.[12-14] ESPT has been demonstrated in solution,[2, 5, 15] solid state[16], host-guest complexes,[17] and MOFs.[18] Experimental and theoretical investigations of these systems by Förster, Weller,

Eigen, and others have dramatically increased our understanding of the mechanism and structure-property relationships that dictate ESPT.[11, 19-22]

1.2.1 Excited State pK_a

One of the most defining features of ESPT mechanisms is the increased acidity of aromatic proton donor groups. This increase in acidity can be quantified in terms of the acid dissociation constant Ka or more commonly as its cologarithm pK_a. The K_a is defined by equation 1.1:

$$K_a = [A^-][H^+]/[HA] \qquad (1.1)$$

where [A⁻] [H⁺] and [HA] represent the concentration of the conjugate base, protons, and acid at equilibrium. The more convenient pK_a is found by equation 1.2:

$$pK_a = -\log_{10} K_a \qquad (1.2)$$

Smaller pK_a values indicate increased acid strength on a logarithmic scale, meaning that a decrease of 1 pK_a unit corresponds to a 10x increase in the acidity of the system. Among the primary observations that led to the discovery of ESPT was emission from the anionic form of 2-naphthol even in a highly acidic environment. The pK_a of naphthol is reported to be ~9.6 making it a poor acid in its ground state. Förster experimentally determined the excited state pK_a (pK_a^*) of naphthol to be 2.8 and from this information was able to derive the first equation for determining pK_a^* known as the Förster equation (1.3).

$$pK_a^* = pK_a - (h\nu_{HA} - h\nu_{A-})/\ 2.3RT \qquad (1.3)$$

where R is the gas constant, T is temperature, $h\nu_{HA}$ and $h\nu_{A-}$ are the energy of the 0–0 electronic transition for the protonated and deprotonated forms of the dye, respectively.[11] With this method one only needs to know the ground state pK_a and measure the absorption and emission spectra of both the protonated and deprotonated forms of the dye. Because it does not account for dynamic

events like solvent relaxation, it is a reasonable but only approximate estimate of pK_a^*.[23] A more experimentally intensive and accurate means of determining pK_a^* is to measure time-resolved emission from the dye during an acid/base titration and then fit the decay kinetics to determine the rates of forward (k_{pt}) and reverse proton transfer (k_{rpt}) which are used to calculate pK_a^*.[24]

The strength of acids is of great general importance in chemistry. Strong acids are defined as being more acidic than the hydronium ion, and therefore must have a pK_a less than either 0 or -1.74 (typical reported pK_a for hydronium)[25]. The sometimes extreme pK_a changes of ESPT molecules can result in pK_a^*s below the threshold of many conventional strong acids making them relevant for applications which may utilize ground state strong acids. Tolbert and others have used the term "Super Photoacids" to describe this class of ESPT molecules which have a $pK_a^* < 0$ at room temperature in water. [6, 26] The earliest Super photoacids were cyano-naphthol derivatives with the most acidic of these being 5,8-dicyano-2-naphthol, with a pK_a^* of -4.5[27]. Since then N-methyl-6-hydroxyquinolinium iodide[4, 6], quinone cyanine[28], and pyranine[26] have found utility as super photoacids with drastically increased excited state acidity as low as $pK_a = -7$.

1.2.2   Solvent Dependence of Excited State Proton Transfer

Much research has been done to demonstrate the significant effect of solvent on the ESPT mechanism. Perhaps the most noteworthy feature of this solvent dependence is a shift in the emission spectra of ESIPT fluorophores in different solvent systems. While the ESIPT reaction is typically very efficient and fast, two different types of emission band (enol and keto) are often observed in ESIPT molecules depending on the nature of the chemical environment and in particular the fluorophores solvent sphere. ESIPT fluorophores are well known to exhibit dual fluorescence emitting from both their enol and keto excited states. It has been demonstrated that this dual emission is strongly dependent upon both the solvent polarity and upon its ability to hydrogen bond to the fluorophore. The keto emission band is predominantly observed in hydrocarbon and non-polar solvents, displays a large apparent Stokes' shift and is characteristically structureless.[29] The other band, resulting from enol emission, is observed either in protic or polar solvents with typical small Stokes' shift, is attributed to emission ESIPT

occurs.[30] The relative intensities of these two bands were found to vary according to the solvent conditions and molecular structure.[31]

The use of polar or protic solvents such as methanol, ethanol, water, or DMSO tends to inhibit the keto emission because the proton donor preferentially hydrogen bonds with the solvent instead of forming H-bonds between the intramolecular donor acceptor pair.[32] This perturbation transforms the normal E form into the solvated E form (E-solv), resulting in the significant rise of the E* emission band at the cost of suppressed K* emission band.[33]The solvent H-bonds typically reduce the rate of ESIPT.[31, 34, 35] As a result, the dual emission dominates and fluorescence appears drastically blue shifted from the increase of enol emission.

This dual emission behavior in ESIPT molecules possessing five-membered ring hydrogen-bonding structures such as 3-hydroxyflavone (3HF), due to the weak intramolecular H-bond between the 3-hydroxyl and 4-carbonyl groups.[33] Kasha et al reported that 3HF exhibits a π–π* from its 335 nm absorption band to the large apparent Stokes' shifted green K* emission at 520 nm in non-polar solvents such as 2-methylbutane.[36] In polar protic solutions, however, 3HF was found to exhibit both the violet E* -solv fluorescence at 405 nm and the green K* fluorescence at 528 nm. A striking feature of this dual emission is the large variation of the ratio between enol and keto emission bands according to the solvent polarity. Their ratio ranged from unity up to the complete disappearance of one of the forms.

Other ESIPT systems have shown strong emission from both the enol and keto tautomers with emission maxima relative to the polarity of their aprotic solvent. In particular 2-(2'-hydroxyphenyl)benzoxazole (HBO) and several of its analogs have been the subject of many solvent dependence studies. It is commonly observed for HBO and its analogs that in aprotic nonpolar solvents intramolecular H-bonding between phenolic proton and the ring heteroatom dominates and as a result rapid ESIPT yields exclusively keto emission. This was attributed to the prevalence of the anti-enol rotamer. However in DMSO and MeOH the solvent stabilizes the syn-enol rotamer through H bonding and therefore a drastically blue shifted keto emission was observed in both as well as a decrease in the ratio of keto to enol emission.[35]

However, the direction of solvatochromism (whether it is positively or negatively associated) varies from system to system. HBO derivatives with electron acceptors at the benzoxazole side were reported, HBOCE and HBODC, which dual emissions at room temperature, with one emission band at 430 nm and another one in the region beyond 500 nm.[37] Interestingly spectral positions of the

keto emission for these molecules were largely varied from the green to the orange range with increasing polarity in aprotic solvents. This positive solvatochromism of keto emission is just opposite to the spectral trend in nonsubstituted HBO mentioned above. The emission band above 500 nm showed large positive solvatochromism, moving to a longer wavelength in polar solvents. These features are drastically different from the properties of the unsubstituted HBO, which shows only the emission band of the keto tautomer, and with small negative solvatochromism. It was proposed that the extended π-conjugation framework of the substituted HBO may be responsible for the difference between these dyes and the unsubstituted HBO. [37]

Solvent dependent effects are not exclusive to ESIPT systems. ESPT has shown an "anomalous" solvent effect which has been the subject of much inquiry since the early days of the field. Naphthols typically exhibit efficient proton transfer to water, but not to alcohols or some other nonaqueous basic solvents. This result was initially unexpected due to the gas- phase proton affinity of several solvents listed being higher than that of water.[38] A key ingredient in the efficiency of proton transfer may be the degree of prior formation of the hydrogen-bonded complex. To examine this hypothesis Tolbert and Solntsev studied the solvatochromism of 2-naphthol,[39] while Pines et al. have conducted similar investigations of 1-naphthol[40] and pyranine[41]. Correlating spectral shifts with the Kamlet−Taft parameters (π^*, β, and α) of the solvents,[42] three types of H-bonding were identified between solvents and naphthol. In the ground state the hydroxyl group of naphthol can form two types of hydrogen bonds with solvent HS: ArOH···SH, where solvents act as proton acceptors, and ArHO···HS, where solvents donate a proton to naphthol. Solvents more basic than water, such as amides or DMSO, induce the largest solvatochromic shifts, but without deprotonation. A third type of H-bond, ArO⁻···HS, may also play a crucial role in the thermodynamics by stabilizing the anion. Thus, as a moderate proton acceptor (Taft parameter β), water is one of the strongest proton donors (parameter α) and is, therefore, the best for solvating *both* proton and anion.[2]

Aside from solvatochromic effects solvent has been known to influence the lifetime kinetics of ESIPT systems. In 3-hydroxyflavone, the proton transfer reaction occurs in ~100 fs in dry nonhydrogen bonding solvents.[43] In hydrogen bonding solvents the observed proton-transfer time in 3-hydroxyflavone reflects the time required for the displacement of the solvent hydrogen-bonded to the enol proton of the solute, thus permitting the proton to effect its transfer resulting in a drastically increased lifetime.[44]

Still other ESIPT systems have shown that their emission properties are not necessarily sensitive to the solvents, which contrasts with typical ESIPT chromophores. Several solvochromic effects observed for ESIPT dyes are caused by H-bonding interactions between the ESIPT site and solvent sphere. Possible explanations for the lack of shift mentioned before include strong H-bonding between the intramolecular proton donor and acceptor which is capable of preventing solvent interruption.[45]

1.2.3   pH Dependence of Excited State Proton Transfer

As with most systems in chemistry proton transfer moieties exist in an equilibrium with their surroundings either accepting them when there is an external excess or donating them when there is sufficient driving force. ESIPT molecules are no different. Since these dye molecules have both a proton donor and acceptor group, typical ESIPT molecules can also be protonated or deprotonated depending on the pH of the solution.[46] Among various ESIPT molecules, HBI was studied in aqueous solution as a model to investigate this prototropic equilibria and photophysical properties of its protonated, neutral, and deprotonated forms.[47]

In neutral aqueous solution, HBI showed a $\pi–\pi^*$ transition peak at 320 nm in the absorption spectrum and dual bands in the emission spectrum which comprise a weak enol emission at 350 nm and a large apparent Stokes shifted (>100 nm) keto emission at 450 nm, respectively.

In acidic solution, the absorption maxima of HBI were slightly red shifted compared to those in neutral solution, but the shape of the spectrum was almost identical. In highly acidic solutions, excited state *intramolecular* proton transfer cannot occur, because the proton acceptor is already protonated, however, fluorescence emission from cationic form can result from proton transfer to the hydrogen bond accepting solvent. This emission feature is almost identical to that of K* emission in neutral conditions. The extreme excited state acidity of the phenolic group allows for protonation of the acidic medium through ESPT and the resultant deprotonated excited state is functionally identical to the species formed from neutral conditions.

In basic solution the $\pi–\pi^*$ transition peak at 320 nm disappeared while a new band formed at 350 nm, which accompanied a blue-shifted fluorescence emission of 0.6 with a normal Stokes' shift. This means HBI forms the anion by deprotonation in basic solution, resulting in a

new absorption band that is red-shifted and new emission band that lies in the middle of its original enol and keto emission bands.[29]

Shi et al noticed unusual photophysical properties related to the ESIPT event in fluorescent green protein. In particular, deprotonation of the phenolic hydroxyl of the chromophore changed the spectra dramatically. Fluorescent proteins with a protonated (neutral) green chromophore possessed an absorption peak at about 400 nm, while chromophore deprotonation lead to an 80–90 nm absorption red shift. A similar dependence was observed for red fluorescent proteins: they absorb at about 450 and 550–600 nm with protonated and deprotonated chromophores, respectively. Protonated chromophores produced a corresponding short-wavelength emission (blue for green FPs or green for red FPs), but more typically they exhibit ultrafast excited-state proton transfer (ESPT) and emit at longer wavelengths, similar to emission of the corresponding anionic chromophore (keto emission).[48]

The Zhu group has demonstrated the somewhat counterintuitive effects pH change can have on ESIPT systems. They examined susceptibilities of the absorption spectrum of an HBO derivative to DBU (1,8-diazabicyclo[5.4.0]undec-7-ene), a base, and TFA (trifluoroacetic acid), an acid, in DMSO were examined. The addition of TFA did not significantly alter either absorption or emission spectra. Presumably this was because in DMSO excited state proton transfer to the solvent occurs preferentially to intramolecular proton transfer, and therefore the protonation state of the HBO acceptor is inconsequential. The addition of DBU amplified the 457 nm band of the anion (1-enolate) at the expense of the 1-enol band. An isosbestic point was developed during the titration experiment in the absorption mode, indicating that the neutral and anionic forms were the only two species interconverting in the ground state.[49]

1.2.4   Typical Excited State Proton Transfer Moieties and Rational Design

Intermolecular ESPT has relatively few design limitations since the proton accepting moiety is not a part of the dye structure. The most unifying feature of ESPT molecules is the presence of an aromatic alcohol, and less commonly aromatic amine. Extending the conjugation of the aromatic moiety is known to shift the absorption range of the dye further into the visible range, and therefore when applications necessitate excitation with near UV or visible light polyaromatic systems are commonly employed.
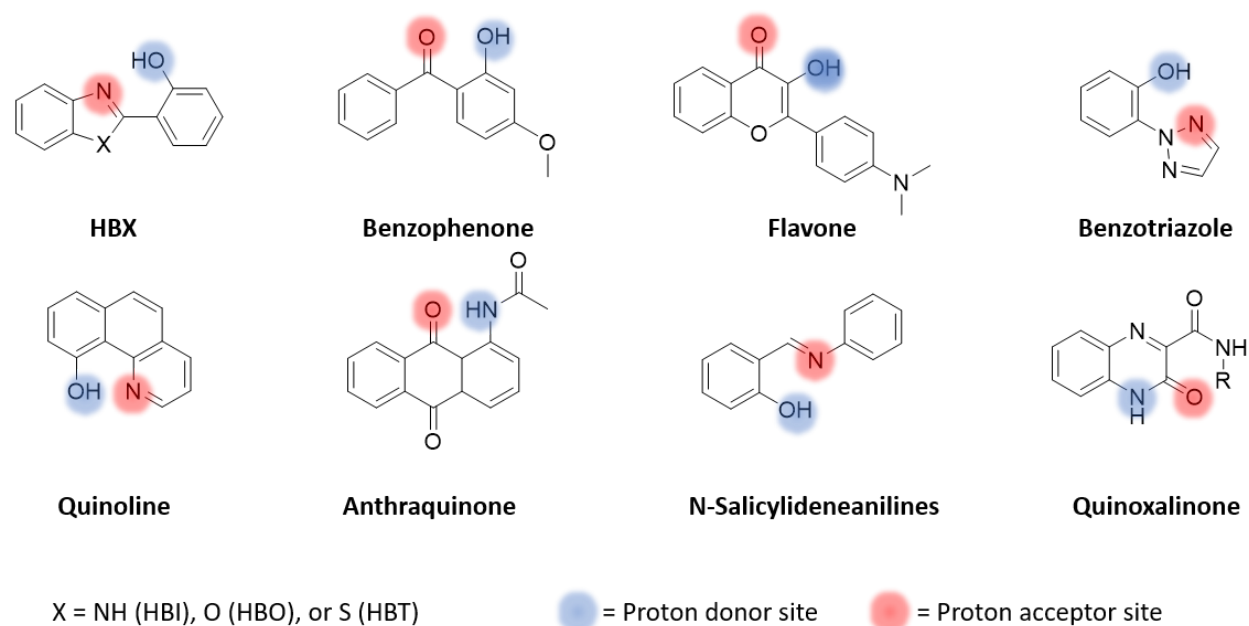
Figure 1.4 Several of the most commonly used ESIPT fluorophores with their proton donating and accepting sites highlighted.

The most common ESIPT fluorophores are analogues of 2-(2′-hydroxyphenyl)benzimidazole (HBI), 2-(2′-hydroxyphenyl)benzoxazole (HBO) and 2-(2′-hydroxyphenyl)benzothiazole (HBT). Additional ESIPT fluorophores that have been reported include quinoline, benzophenones, flavones, anthraquinones, benzotriazoles, *N*-salicylideneaniline, and quinoxalines.[12]

In 2016 the Jacquemin research group published a review of HBO derivatives in an effort to derive design guidelines for creating dual emitter ESIPT molecules. Through the course of this investigation they analyzed the position and push/pull nature of substituents as well as the role of the ring heteroatom. The presence of an electron withdrawing group (EWG) on the proton acceptor side of the molecule universally decreased the stability of the keto tautomer thus increasing enol emission. In contrast, EWGs on the proton donor side yield mixed results, stabilizing either the keto or enol excited states. Interestingly, adding donor groups systematically favors the excited state enol form, and hence limits ESIPT, irrespective of the substitution side. This result was expected for the phenol side, as increasing the electron density near the hydroxyl should increase the covalent character of the O-H bond thereby making it less acidic. The somewhat more counterintuitive EDG effect when substituting the benzoxazole moiety causes the magnitude of the enol stabilization to be even larger. EDGs on the proton

acceptor side decrease the acidity of the excited state phenol by localizing the excited state on the benzoxazole side. The change of density on the hydroxyl after absorption becomes too small to favor ESIPT.[50]

The same study found that EDG and EWG effects are not additive, with extremely diminishing effects on either keto or enol stabilization.[50]

As mentioned previously the strength of the bond between the proton donor and its proton is a deciding factor in the molecules capability to do ESIPT. The pK_a of aniline is ~30 while the pK_a of phenol is ~10. ESIPT rarely takes place in N–H hydrogen bonding such as from aniline systems unless the acidity of the N–H proton can be enhanced via chemical modification. Tseng et al demonstrated that through systematic variation of the amine, and the adjacent phenyl ring ESIPT can be made favorable. By replacing one of the N–H protons with an electron-withdrawing tosyl (Ts) group or acetyl (Ac) group. Notably from their study was that phenyl substitution alone was not sufficient to weaken the N-H bond into the realm of ESIPT.[34]

The excited state acidity of dyes can be intentionally modified through the addition of specific substituents. Electron withdrawing groups are typically expected to increase electron density redistribution away from aromatic alcohols, while electron donating groups should decrease this effect. Early work from the Tolbert group demonstrated this by the addition of -CN groups to 2-naphthol leading to a maximum acidity of $pK_a^* = -4.5$.[27] Other investigations into the excited state acidity of substituted flavanols revealed that the pK_a^* can be controlled through modifying the fluorophore with electron donating or withdrawing groups. When the flavanols were substituted with fluorine the excited state acidity decreased (more acidic) and when substituted with amine derivatives the pK_a^* increased slightly.[51]

1.3   Applications of ESPT

Despite how long ESPT has been known of it has found relatively few applications until the last decade or two. Early interest in ESPT systems was due to their uses as chemosensors providing a highly sensitive scaffolding to determine the presence of a target analyte. With the advent of OLED technology research groups are looking to ESIPT fluorophores to provide new and more efficient emitters.

1.3.1   Photoacid Generators

Aside from the novelty of these super photoacids they offer several advantages over conventional strong acids. One such application would be the temporary generation of acidity. The transient nature of excited state proton transfer is exactly suited to this application[52], with the increase in acidity lasting only as long as the molecules are irradiated and then promptly relaxing within picoseconds[28]. Photoacid generators (PAGs) are compounds which under irradiation undergo reactions or dissociations in which the final photoproducts formed include acidic species.[53] PAGs have become integral tools in biological probing[54], controlling enzyme activity[54], and in photodynamic therapy[55]. But the major role for which PAG's have become essential is for polymerization initiation and in the manipulation of polymer coatings and resins[56]. Conventional PAGs undergo irreversible photoreactions that can also generate undesired secondary products. One solution to this problem would be to employ ESPT dyes as transient photoacid generators[52].

Modulating the acidity of polymeric materials is a common strategy to alter their physical properties which can then open the door to drug delivery and other biomedical applications. These materials, commonly referred to as intelligent, adaptive, or switchable in the literature respond to some triggering event (i.e. pH change or irradiation) which results in physical changes in the material[57]. Different photoacids based on 1-naphthol into amphiphilic block copolymers (BCPs) through a direct RAFT polymerization and deprotection approach[58]. amphiphilic terpolymers containing photoacids based on 1-naphthol using reversible addition fragmentation chain transfer radical polymerization[59] To demonstrate the potential of these photo-responsive micelles for controlled release, a model hydrophobic guest molecule (Nile Red) was encapsulated, and triggered release based on a light-mediated excited state proton transfer (ESPT) from the photoacid to DMAEMA could be observed, due to a shift in the hydrophilic/hydrophobic balance of the overall diblock quarterpolymer. Upon irradiation with light, the photoacid pendant moieties experience a strong increase in acidity, resulting in the protonation of the neighboring DMAEMA units, and a shift in the overall hydrophilic/hydrophobic balance of the BCP. We demonstrate this photo-response through the encapsulation and subsequent light-mediated release of Nile Red, a model hydrophobic guest molecule, using fluorescence emission spectroscopy.

The highly nuanced field of biochemistry requires precise control of pH for reactions to proceed properly and they often require an acidic environment. However due to the sensitive nature of

biological systems pH may not be adjusted as simply as adding a buffer solution. Non-invasive control over proton transfer is therefore a highly desirable technology, which may be accomplished through excited state proton transfer. Irradiation can be controlled for precise wavelength, time, location, and intensity, which opens pathways to many different therapies and imaging techniques.

Enzymatic kinetics measurements could benefit greatly from precise control of their activation and deactivation times. Typically, this has been accomplished through thermal controls or irradiation. Thermal activation is unfortunately only applicable for reactions that occur at temperature extremes and photoresponsive proteins or receptors are difficult to synthesize and is not applicable to most enzymes. Therefore modulation of the chemical environment is a practical method for enzymatic control.[60, 61] A 2-naphthol based photoacid system was used to affect a pH change in acid phosphatase. The reaction of p-nitrophenyl phosphate with the enzyme was studied in the presence of the photoacid and irradiation and in the dark and it was shown that the photoacid successfully generated the requisite acidic environment for the enzyme to become active, while in the dark product was not observed. [60]

In 2015, Das et al. demonstrated upon 365 nm excitation, 7-bromo-2-naphthol was sufficiently acidic to protonate 1-phenyl-2-(trimethylsiloxy)cyclohexene and generate 2-phenylcyclohexanone via ESPT (Figure 27).[62] The reaction was made catalytic by the addition of phenol as the sacrificial proton source. Up to 96 % yield of the product was obtained with 1 mol% 7-bromo-2-naphthol catalyst.

Biological probes are essential tools in medicine for understanding the microenvironments in cells.[63] 2,6-naptholsulfonate is known to exhibit rapid ESPT in aqueous solution however when this chromophore is adsorbed to bovine serum albumin (BSA), little or no proton transfer is observed. As a result of this the presence of BSA was easily characterized by fluorescence spectroscopy.[63] While early investigations into the use of ESPT as biological probes remained limited due to the poor solubility and low QY of these molecules, work by the Jung group has demonstrated that highly fluorescent and lipophilic ESPT probes can be designed with high cellular uptake to show multiphoton fluorescence micrographs after treatment of Hep-G2 cells with pyranine based fluorophores.[26] Yet another biological probe has used the generation of an ESPT dye in situ to determine the enzymatic activity. The product of this dephosphorylation enzyme reaction, 6-chloro-8-fluoro-4-methylumbelliferone, possessed strong fluorescence at ~450 nm with low pKa (4.7). The large apparent stokes shift of ESPT was integral in its fluorescent imaging.[64]

1.3.2 Sensors

ESIPT fluorophores typically have large apparent Stokes shifts (~200 nm) when compared to traditional fluorophores (fluorescein, BODIPY, rhodamine, etc) as discussed in section 1.1.2. The large Stokes shift is a desired feature for sensors because the self-absorption, or the inner filter effect, can be avoided and the fluorescence analysis can be improved with this kind of fluorophore.[13] They are also highly sensitive to changes in structure and the local environment as mentioned in sections 1.2.2 and 1.2.3.

For chiral sensing, atropisomeric ESPT dyes have proven to be an effective means of detecting chiral amines, amino acids, carboxylic acids, and more using fluorescence measurements. The generally accepted mechanism of fluorescent ESPT sensing of an amine substrate (NR_3) by BINOL (BIN-OH). Following excitation ($h\nu_a$) BIN-OH can undergo radiative ($h\nu_{em}$) and non-radiative decay (k_{nr}). In the presence of an amine, the excited state of BINOL can hydrogen bond to the lone pair of nitrogen (K^*_{HB}) which facilitates non-radiative decay from the adduct species (k'_{nr}). Alternatively, if intermolecular ESPT is favorable (k^*_{PT}), BIN-O$^-$ is generated and can relax through non-radiative decay (k''_{nr}) or emit at a large apparent Stokes shifted wavelength ($h\nu'_{em}$).[65]

The extreme dual emission characteristic of 3HF derivatives have been used for biomolecular sensors which can probe polarity, electrostatic fields, and the structural variations in micelles and biomembrane models.

1.3.3 Emissive Materials

One of the most promising features of ESIPT dyes lies within their large apparent stokes shift. With a sufficiently large red shift self-absorption and inner filtering may be entirely avoided making them optimal emissive materials.

Good laser material should have high luminescence efficiency and a high chromophore density, but more importantly is that the excited-state absorption spectrum should not overlap with the stimulated emission spectrum.[66] in ESIPT molecules, stimulated emission (SE) could readily be observed even in rather higher concentration due to the guaranteed population inversion without self-absorption attributed to its intrinsic four level photocycle[14] The amplified spontaneous emission (ASE) phenomenon of ESIPT molecule was first reported 30 years ago

with 3-hydroxyflavone by Kasha and his colleagues[67] One very beneficial property of ESIPT molecules is that the ASE wavelength can be widely separated from the region of the optical pump source due to their large apparent Stokes' shift. Moreover, it is noteworthy that their Stokes' shift can be easily tunable by the chemical modification (section 1.2.4). [14,68] Efficient ASE of ESIPT molecule was also observed in dendrimer neat films incorporating ESIPT molecules.[69]

OLEDs based on organic fluorescent materials are of increasing interest because of their many advantages such as wide viewing angle, flexibility, color reproducibility, and fast-response time in comparison to alternative emissive technologies.[14]

White-Light Generation from a Single Molecule is of increasing interest as we move away from inefficient incandescent lights. Most white LEDs are still composed of multiple discrete color LEDs combined to generate white light. This results in relatively poor color reproducibility. A solution to this would be single molecule systems. ESIPT offers an attractive solution to this problem given that a single molecule can emit from both the enol and keto forms therefore spanning a large portion of the visible spectrum. Work from the Park[70], and Zhu[49] groups has recently made strides towards this goal.

The Park group synthesized a concentration-independent white-light-emitting molecular dyad based on two ESIPT keto-emitting units. The independent blue and orange light emitting moieties were covalently linked to cover much of the visible spectrum. The system was designed such that energy transfer is frustrated, and the combination thus shows broad white photoluminescence covering the entire visible range after single-wavelength excitation.[70]

CHAPTER 2

METHODS

2.1   Materials

2-Phenylcyclohexanone, 2-Methyl-1-Indanone, lithium diisopropylamide (LDA), Trimethylsilylchloride, Triethylsilylchloride, Trisopropylsilylchloride, Triphenylsilylchloride, (R)-VANOL(2a), (S)-VANOL, (R)-BINOL (1a), (R)-3,3'-Dibromobinol(1b), Bis[2-(4,6-difluorophenyl)pyridinato-C2 ,N](picolinato)iridium(III) and triphenylmethane were used as received from Sigma-Aldrich. All the substrates, 1-3 (R)-7,7'- Dibromo-BINOL(1c),4,5 and (R)-Dibromovanol(2b) 6 were prepared according to a published literature procedure.

N(α)-benzyloxycarbonyl-L-tryptophan (Z-Trp-OH) and N,N'-dicyclohexylcabodiimide (DCC) were purchased from Alfa Aesar and used without further purification. 4-(dimethylamino)pyridine (DMAP), N-(tert-butoxycarbonyl)-L-phenylalanine (Boc-Phe-OH), N-(tert-butoxycarbonyl)-L-2-phenylglycine (Boc-Phg-OH), N-benzyloxycarbonyl-L-proline (Z-Pro-OH), N- (tert-butoxycarbonyl)-L-proline (Boc-Pro-OH), N-(tert-Butoxycarbonyl)-L-alanine (Boc-Ala-OH), (1S)-(+)-Menthyl chloroformate, triethylamine, diisopropylethylamine, pyridine, and isopropylamine were all purchased from Sigma Aldrich and used without further purification. Racemic 1,1'-Bi-2-naphthol, (R)- 1,1'-Bi-2-naphthol, and (S)- 1,1'-Bi-2-naphthol were purchased from TCI and used without further purification. HPLC grade CH_2Cl_2 was purchased from Sigma-Aldrich and used without further purification. Dry solvents were obtained from a Pure Process Technology solvent purification system.

Barium perchlorate, calcium perchlorate tetrahydrate, calcium chloride, cadmium perchlorate hydrate, cobalt(II) perchlorate hexahydrate, copper(II) perchlorate hexahydrate, iron (II) perchlorate hydrate, mercury(II) perchlorate hydrate, magnesium perchlorate hexahydrate, manganese(II) perchlorate hydrate, nickel(II) perchlorate hexahydrate, , zinc perchlorate hexahydrate, cadmium acetate dihydrate, copper(II) acetate, sodium acetate trihydrate, 2-aminopyridine, 2,3-dicyanohydroquinone, 4-(dimethylamino)pyridine (DMAP), 1-Ethyl-3-(3-dimethylaminopropyl)carbodiimide hydrochloride (EDC HCl), di-*tert*-butyl dicarbonate (Boc$_2$O), and 4-bromobutanoic acid, *n*-butanol, acetonitrile, dichloromethane, toluene, and methanol were

all purchased from Sigma Aldrich and used without further purification. Sodium chloride was purchased from Ward's Scientific and used without further purification. Dimethyl sulfoxide, strontium perchlorate trihydrate, and zinc acetate dihydrate were purchased from Alpha Aesar and used without further purification. Ethylene glycol was purchased from EMD Millipore and used without further purification.

2.2   Synthesis

2.2.1   Synthesis of BINOL with Chiral Auxiliary Groups
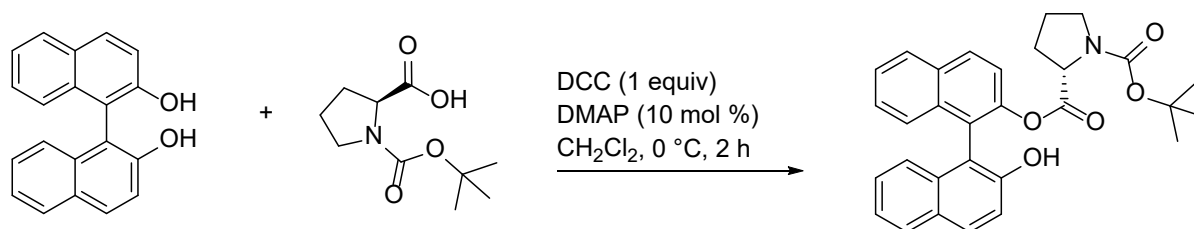
Figure 2.1 Synthetic scheme for Boc-Pro-BINOL

Boc-Pro-BINOL (1): (R/S)BINOL (1 g, 3.49 mmol, 1 equiv), dicyclohexylcarbodiimide (0.86 mg, 4.19 mmol, 1.2 equiv), N,N-dimethylaminopyridine (0.05 mg, 0.42 mmol, 0.12 equiv), and N-(tert-Butoxycarbonyl)-L-proline (0.9 g, 4.19 mmol, 1.2 equiv) were added to a 250mL three neck round bottom flask equipped with a magnetic stir bar. The flask was purged and backfilled with N_2 three times and submerged in an ice bath. 100 mL of cold CH_2Cl_2 (~0° C) was added via syringe to the reaction flask. Seconds to minutes after the solvent was added dicyclohexyl urea can be seen precipitating from solution. The solution was stirred at 0° C until TLC indicated that most or all of the BINOL had reacted (~2 hours). The reaction mixture was then rotary evaporated to remove 2/3^{rds} of the solvent volume, causing more dicyclohexyl urea to precipitate from solution. The resulting slurry was vacuum filtered and washed with three 5mL portions of cold CH_2Cl_2. The filtrate was then rotary evaporated to dryness. A silica gel column was prepared by wet packing 60 grams of 400-600 mesh silica with hexanes in a 40 mm column. The crude product was wet loaded with minimal CH_2Cl_2 onto the column and eluted with 25%

EtOAc/hexanes until the monosubstituted product was obtained. The fractions were combined and evaporated to dryness to obtain **1** (1.61 g, 95% yield) as an off-white amorphous solid. ^{1}H NMR (400 MHz, Chloroform-*d*) δ 8.1 – 7.8 (m, 4H), 7.6 – 7.2 (m, 7H), 7.1 – 7.0 (m, 1H), 5.3 – 5.2 (m, 1H), 4.3 – 4.1 (m, 1H), 3.4 – 2.9 (m, 2H), 1.5 – 1.4 (m, 10H), 1.4 – 0.9 (m, 2H), 0.9 – 0.3 (m, 2H). ^{13}C NMR (101 MHz, Chloroform-*d*) δ 172.2, 153.6, 151.8, 147.8, 147.8, 133.5, 131.1, 130.6, 130.5, 129.1, 128.5, 128.1, 128.0, 128.0, 127.7, 127.3, 127.1, 127.0, 126.7, 126.5, 126.4, 126.2, 125.9, 125.7, 125.7, 124.9, 124.7, 124.5, 123.9, 123.8, 121.4, 121.4, 118.5, 118.4, 118.2, 100.1, 80.3, 80.1, 80.0, 76.9, 59.0, 58.9, 58.5, 46.3, 46.1, 30.1, 29.8, 29.3, 28.7, 28.6, 28.5, 23.8, 23.4, 23.1, 22.5. HRMS (ESI+) *m/z* calcd. For $C_{30}H_{29}NNaO_5$ ([M+Na]$^+$) 506.19434, found 506.19446.
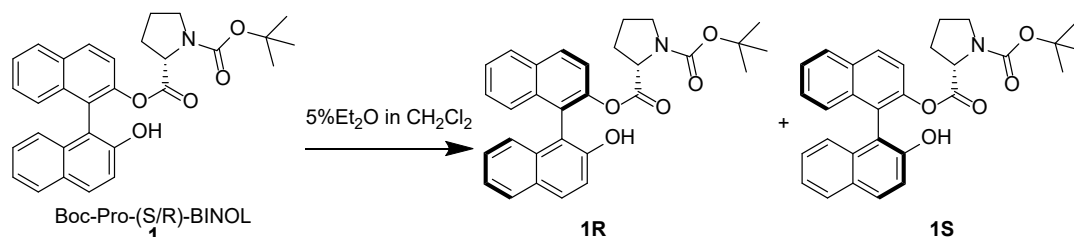
Figure 2.2 Synthetic scheme for separation of R and S diastereomers of Boc-Pro-BINOL

Separation of R and S diastereomers of Boc-Pro-BINOL (**1R** and **1S**): For irradiation experiments a large quantity of **1R** and **1S** were necessary to repeat measurements. Instead of synthesizing these from enantiopure starting materials, 1g of (R/S) Boc-Pro-BINOL was synthesized according to the above procedure and then subjected to silica column chromatography to separate the diastereomers following a modified literature procedure.[1] A 5% Et$_2$O in CH$_2$Cl$_2$ solution was used as the solvent. Due to the difficulty of the separation, several of the fractions were found to contain traces of both **1R** and **1S**, and therefore great care was taken to only combine fractions which contained only one diastereomer. Chiral SFC analysis of **1R** and **1S** confirmed their enantiopurity. The fractions which contained some quantity of both diastereomers were combined to constitute the racemic sample. Chiral SFC indicated a slight excess of **1R** which was adjusted by adding small amounts of **1S** until the SFC trace showed a 50/50 ratio of diastereomers.
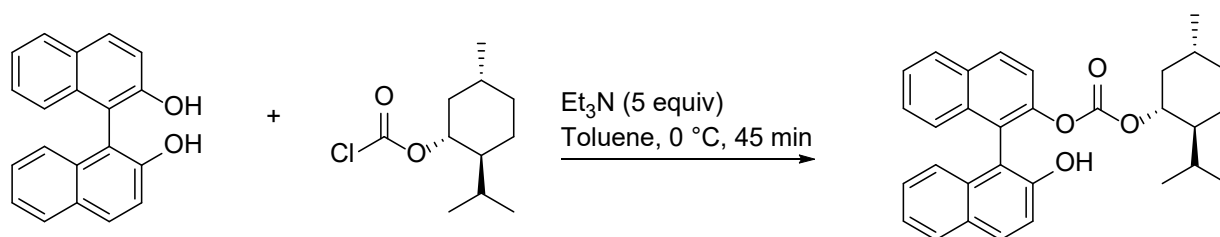
Figure 2.3 Synthetic scheme for Menthyl-BINOL

Synthesis of Menthyl-BINOL (2): (R/S)BINOL (250 mg, 0.873 mmol, 1 equiv) and (S) menthyl chloroformate (210 mg, 0.960 mmol, 1.1 equiv) were added to a 250 mL 3 neck round bottom flask equipped with a magnetic stir bar. The flask was purged and backfilled with N_2 three times. 60 mL of toluene was added to the flask and stirred until the BINOL was completely dissolved. Et_3N (0.609 mL, 4.366 mmol, 5 equiv) was added slowly via syringe with stirring. The reaction mixture was stirred at room temperature until TLC indicated completion of the reaction, ~45 minutes. The reaction was quenched with 10 mL of 4 M HCl, extracted with water 3 times, dried over anhydrous sodium sulfate, and evaporated to dryness. A silica gel column was prepared by wet packing 12 grams of 400-600 mesh silica with hexanes in a 15 mm column. The crude product was wet loaded with minimal CH_2Cl_2 onto the column and eluted with 10% EtOAc/hexanes until the monosubstituted product was obtained. The fractions were combined and evaporated to dryness to obtain **2** (0.301 g, 74% yield) as an off-white amorphous solid. ^{1}H NMR (400 MHz, Chloroform-*d*) δ 8.1 – 8.1 (m, 1H), 8.0 – 8.0 (m, 1H), 8.0 – 7.8 (m, 2H), 7.6 – 7.5 (m, 2H), 7.4 – 7.3 (m, 4H), 7.3 – 7.2 (m, 1H), 7.1 (ddt, *J* = 7.7, 4.5, 1.1 Hz, 1H), 5.3 (d, *J* = 5.3 Hz, 1H), 4.4 (qd, *J* = 11.0, 4.6 Hz, 1H), 1.8 – 1.5 (m, 4H), 1.4 – 1.2 (m, 2H), 1.0 – 0.7 (m, 7H), 0.7 – 0.5 (m, 5H). ^{13}C NMR (101 MHz, Chloroform-*d*) δ 153.9, 152.0, 151.9, 148.1, 133.6, 133.5, 132.5, 132.4, 131.0, 131.0, 130.6, 130.6, 129.3, 128.4, 128.1, 128.1, 127.6, 127.6, 126.9, 126.9, 126.5, 126.5, 126.0, 126.0, 124.7, 124.7, 123.7, 123.7, 123.6, 123.4, 121.6, 118.5, 118.4, 113.9, 79.8, 46.8, 46.6, 40.4, 39.9, 34.1, 34.0, 31.4, 31.3, 26.7, 26.1, 23.6, 23.4, 22.0, 22.0, 20.6, 20.5, 16.6, 16.2. HRMS (ESI+) *m/z* calcd. For $C_{31}H_{32}NaO_4$ ([M+Na]$^+$) 491.21983, found 491.22072.

Figure 2.4 Synthetic scheme for Z-Pro-BINOL

Synthesis of Z-Pro-BINOL (3): (R/S)BINOL (100 mg, 0.349 mmol, 1 equiv), dicyclohexylcarbodiimide (0.086 mg, 0.419 mmol, 1.2 equiv), N,N-dimethylaminopyridine (0.005 mg, 0.042 mmol, 0.12 equiv), and N-[(Benzyloxy)carbonyl]-L-proline (104 mg, 0.419 mmol, 1.2 equiv) were added to a 50mL three neck round bottom flask equipped with a magnetic stir bar. The flask was purged and backfilled with N_2 three times and submerged in an ice bath. 10 mL of cold CH_2Cl_2 (~0° C) was added via syringe to the reaction flask. After the solvent was added dicyclohexyl urea can be seen precipitating from solution. The solution was stirred at 0° C until TLC indicated that most or all of the BINOL had reacted (~2 hours). The reaction mixture was then rotary evaporated to remove 2/3^{rds} of the solvent volume, causing more dicyclohexyl urea to precipitate from solution. The resulting slurry was vacuum filtered and washed with three 5 mL portions of cold CH_2Cl_2. The filtrate was then rotary evaporated to dryness. A silica gel column was prepared by wet packing 12 grams of 400-600 mesh silica with hexanes in a 15 mm column. The crude product was wet loaded with minimal CH_2Cl_2 onto the column and eluted with 33% EtOAc/hexanes until the monosubstituted product was obtained. The fractions were combined and evaporated to dryness to obtain **3** (0.141 g, 78% yield) as an off-white amorphous solid. ^1H NMR (400 MHz, Chloroform-*d*) δ 8.1 – 7.8 (m, 4H), 7.6 – 7.5 (m, 1H), 7.5 – 7.3 (m, 9H), 7.3 – 7.1 (m, 2H), 7.1 – 7.0 (m, 1H), 5.3 – 5.1 (m, 2H), 5.1 – 5.0 (m, 1H), 4.3 – 4.2 (m, 1H), 3.7 – 3.0 (m, 2H), 2.2 – 1.6 (m, 2H), 1.4 – 1.0 (m, 2H). ^{13}C NMR (101 MHz, Chloroform-*d*) δ 171.9, 171.7, 154.9, 154.1, 154.0, 151.9, 151.7, 147.8, 147.5, 136.6, 136.5, 133.5, 133.4, 133.3, 132.3, 131.0, 130.8, 130.7, 130.6, 130.4, 130.4, 130.2, 128.9, 128.6, 128.6, 128.5, 128.4, 128.4, 128.3, 128.3, 128.3, 128.2, 128.1, 128.0, 127.9, 127.9, 127.8, 127.8, 127.5, 127.5, 127.3, 127.0, 126.9, 126.7, 126.4, 126.2, 125.7, 125.6, 125.6, 124.8, 124.6, 124.5, 124.4, 123.7, 123.7, 123.7, 123.5, 122.9, 122.9, 122.8, 122.1, 121.9, 121.5, 118.3, 118.3, 118.1, 114.1, 113.8, 67.2, 67.1,

67.0, 60.4, 59.2, 58.8, 58.7, 58.4, 46.8, 46.6, 46.3, 46.1, 30.1, 29.9, 29.1, 28.9, 23.7, 23.3, 23.0, 22.3, 14.2, -16.9. HRMS (ESI+) *m/z* calcd. For $C_{33}H_{27}NNaO_5$ ([M+Na]$^+$) 540.17869, found 540.17921.
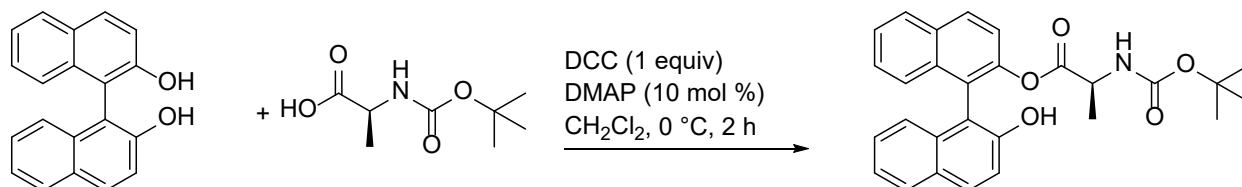
Figure 2.5 Synthetic scheme for Boc-Ala-BINOL

Synthesis of Boc-Ala-BINOL (4): (R/S)BINOL (100 mg, 0.349 mmol, 1 equiv), dicyclohexylcarbodiimide (0.108 mg, 0.524 mmol, 1.5 equiv), N,N-dimethylaminopyridine (0.006 mg, 0.052 mmol, 0.15 equiv), and N-(tert-Butoxycarbonyl)-L-alanine (0.099 mg, 0.524 mmol, 1.5 equiv) were added to a 50mL three neck round bottom flask equipped with a magnetic stir bar. (Note: the R_f values of Boc-Ala-BINOL and BINOL are very similar. To compensate, large excess of Boc-Ala-OH was used to ensure that all the BINOL was reacted making the separation much easier). The flask was purged and backfilled with N_2 three times and submerged in an ice bath. 10 mL of cold CH_2Cl_2 (~0° C) was added via syringe to the reaction flask. Seconds to minutes after the solvent was added dicyclohexyl urea can be seen precipitating from solution. The solution was stirred at 0° C until TLC indicated that all the BINOL had reacted (~2 hours). The reaction mixture was then rotary evaporated to remove 2/3^{rds} of the solvent volume, causing more dicyclohexyl urea to precipitate from solution. The resulting slurry was vacuum filtered and washed with three 5mL portions of cold CH_2Cl_2. The filtrate was then rotary evaporated to dryness. A silica gel column was prepared by wet packing 16 grams of 400-600 mesh silica with hexanes in a 15 mm column. The crude product was wet loaded with minimal CH_2Cl_2 onto the column and eluted with 25% EtOAc/hexanes until the monosubstituted product was obtained. The fractions were combined and evaporated to dryness to obtain **4** (0.065 g, 41% yield) as an off-white amorphous solid. ^1H NMR (400 MHz, Chloroform-*d*) δ 8.1 (t, *J* = 9.2 Hz, 1H), 8.0 – 7.9 (m, 1H), 7.9 – 7.8 (m, 2H), 7.5 (ddt, *J* = 10.0, 6.0, 1.9 Hz, 1H), 7.5 – 7.2 (m, 7H), 7.0 (dq, *J* = 8.4, 0.9 Hz, 1H), 5.4 (s, 1H), 4.2 (t, *J* = 7.5 Hz, 1H), 1.4 (s, 9H), 0.6 (d, *J* = 7.2 Hz, 3H). ^{13}C NMR (101 MHz, Chloroform-*d*) δ 172.1, 151.7, 147.7, 147.5, 133.4, 133.4, 132.4, 131.1, 130.6, 130.5, 130.4, 129.0, 128.4, 128.4, 128.0, 127.6, 126.9, 126.5, 126.3, 125.8, 125.6,

124.7, 124.3, 123.7, 123.5, 122.9, 121.6, 118.2, 113.8, 79.9, 77.2, 28.3, 28.3, 17.1, 17.0. HRMS (ESI+) *m/z* calcd. For $C_{28}H_{27}NNaO_5$ ([M+Na]$^+$) 480.17869, found 480.17681.
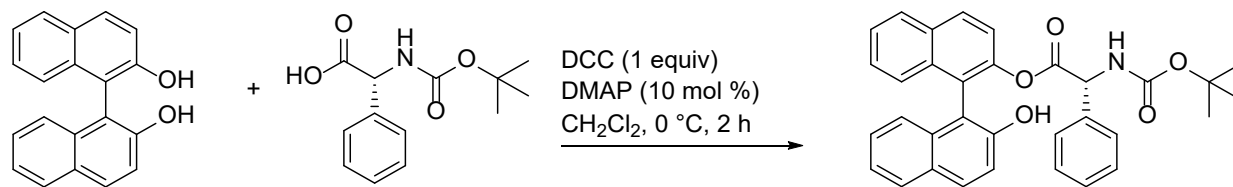
Figure 2.6 Synthetic scheme for Boc-Phg-BINOL

Synthesis of Boc-Phg-BINOL (5): (R/S)BINOL (100 mg, 0.349 mmol, 1 equiv), dicyclohexylcarbodiimide (0.108 mg, 0.524 mmol, 1.5 equiv), N,N-dimethylaminopyridine (0.006 mg, 0.052 mmol, 0.15 equiv), and N-(tert-Butoxycarbonyl)-D-phenylglycine (0.110 mg, 0.524 mmol, 1.5 equiv) were added to a 50 mL three neck round bottom flask equipped with a magnetic stir bar. (Note: the R_f values of Boc-Phg-BINOL and BINOL are very similar. To compensate, large excess of Boc-Phg-OH was used to ensure that all the BINOL was reacted making the separation much easier). The flask was purged and backfilled with N_2 three times and submerged in an ice bath. 10 mL of cold CH_2Cl_2 (~0° C) was added via syringe to the reaction flask. Seconds to minutes after the solvent was added dicyclohexyl urea can be seen precipitating from solution. The solution was stirred at 0° C until TLC indicated that all the BINOL had reacted (~2 hours). The reaction mixture was then rotary evaporated to remove 2/3^{rds} of the solvent volume, causing more dicyclohexyl urea to precipitate from solution. The resulting slurry was vacuum filtered and washed with three 5mL portions of cold CH_2Cl_2. The filtrate was then rotary evaporated to dryness. A silica gel column was prepared by wet packing 16 grams of 400-600 mesh silica with hexanes in a 15 mm column. The crude product was wet loaded with minimal CH_2Cl_2 onto the column and eluted with 25% EtOAc/hexanes until the monosubstituted product was obtained. The fractions were combined and evaporated to dryness to obtain **5** (0.094 g, 52% yield) as an off-white amorphous solid. ^{1}H NMR (400 MHz, Chloroform-*d*) δ 8.05 (dd, *J* = 13.5, 9.0 Hz, 1H), 7.96 (d, *J* = 8.0 Hz, 1H), 7.82 (dd, *J* = 15.9, 8.5 Hz, 1H), 7.74 (t, *J* = 8.3 Hz, 1H), 7.54 – 7.43 (m, 2H), 7.42 – 6.96 (m, 9H), 6.93 – 6.79 (m, 3H), 6.70 (d, *J* = 7.9 Hz, 1H), 5.17 (q, *J* = 7.1 Hz, 1H), 1.43 (d, *J* = 11.9 Hz, 9H); ^{13}C NMR (101 MHz, Chloroform-*d*) δ 170.79, 155.06, 154.88, 151.82, 151.61, 147.69, 135.05, 134.83, 133.60, 133.49, 132.40, 131.08,

24

130.73, 130.65, 130.51, 129.12, 129.03, 128.93, 128.56, 128.46, 128.37, 128.17, 128.07, 127.62, 127.44, 126.99, 126.64, 126.55, 126.38, 126.00, 125.73, 124.74, 124.22, 123.55, 123.47, 123.39, 121.53, 121.46, 118.37, 118.12, 113.68, 80.56, 80.38, 77.37, 76.90, 58.24, 57.73, 28.40, 28.38; HRMS (ESI+) m/z calcd. For $C_{33}H_{29}NNaO_5$ ([M+Na]$^+$) 542.19434, found 542.19383.
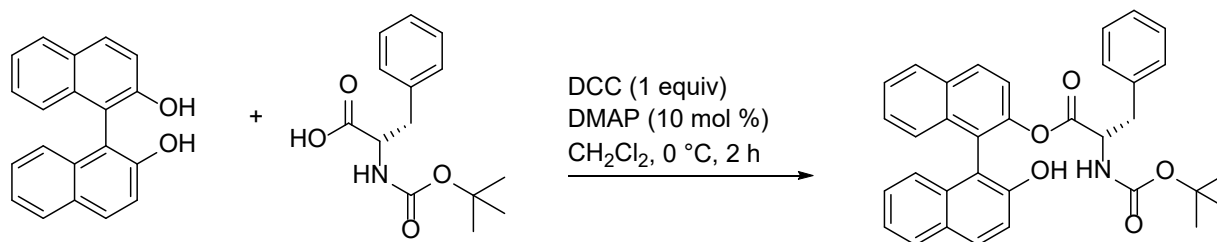
Figure 2.7 Synthetic scheme for Boc-Phe-BINOL

Synthesis of Boc-Phe-BINOL (6): (R/S)BINOL (100 mg, 0.349 mmol, 1 equiv), dicyclohexylcarbodiimide (0.108 mg, 0.524 mmol, 1.5 equiv), N,N-dimethylaminopyridine (0.006 mg, 0.052 mmol, 0.15 equiv), and N-(tert-Butoxycarbonyl)-L-phenylalanine (0.139 mg, 0.524 mmol, 1.5 equiv) were added to a 50mL three neck round bottom flask equipped with a magnetic stir bar. (Note: the R_f values of Boc-Phe-BINOL and BINOL are very similar. To compensate, large excess of Boc-Phe-OH was used to ensure that all the BINOL was reacted making the separation much easier). The flask was purged and backfilled with N_2 three times and submerged in an ice bath. 10 mL of cold CH_2Cl_2 (~0° C) was added via syringe to the reaction flask. Seconds to minutes after the solvent was added dicyclohexyl urea can be seen precipitating from solution. The solution was stirred at 0° C until TLC indicated that all the BINOL had reacted (~2 hours). The reaction mixture was then rotary evaporated to remove 2/3^{rds} of the solvent volume, causing more dicyclohexyl urea to precipitate from solution. The resulting slurry was vacuum filtered and washed with three 5mL portions of cold CH_2Cl_2. The filtrate was then rotary evaporated to dryness. A silica gel column was prepared by wet packing 16 grams of 400-600 mesh silica with hexanes in a 15 mm column. The crude product was wet loaded with minimal CH_2Cl_2 onto the column and eluted with 25% EtOAc/hexanes until the monosubstituted product was obtained. The fractions were combined and evaporated to dryness to obtain **6** (0.117 g, 63% yield) as an off-white amorphous solid. ^{1}H NMR (400 MHz, Chloroform-*d*) δ 8.1 (dd, *J* =

11.4, 8.9 Hz, 1H), 8.0 (dd, *J* = 8.1, 4.1 Hz, 1H), 7.9 – 7.8 (m, 2H), 7.5 (ddd, *J* = 8.2, 5.8, 2.3 Hz, 1H), 7.5 – 7.2 (m, 6H), 7.2 – 7.1 (m, 3H), 7.1 – 7.1 (m, 1H), 6.9 – 6.8 (m, 1H), 6.8 – 6.7 (m, 1H), 4.6 (d, *J* = 8.4 Hz, 1H), 4.4 (td, *J* = 8.8, 4.3 Hz, 1H), 2.2 – 1.8 (m, 2H), 1.3 (d, *J* = 11.9 Hz, 9H). ^{13}C NMR (101 MHz, Chloroform-*d*) δ 171.7, 155.1, 151.8, 147.8, 147.6, 135.9, 133.5, 133.3, 132.4, 131.1, 130.6, 129.0, 128.9, 128.5, 128.4, 128.1, 127.6, 127.4, 127.0, 126.9, 126.8, 126.5, 125.7, 124.5, 123.8, 122.9, 121.6, 118.2, 113.8, 80.2, 80.0, 77.3, 54.1, 36.9, 28.2. HRMS (ESI+) *m/z* calcd. For $C_{34}H_{31}NNaO_5$ ([M+Na]$^+$) 556.20999, found 556.21032.
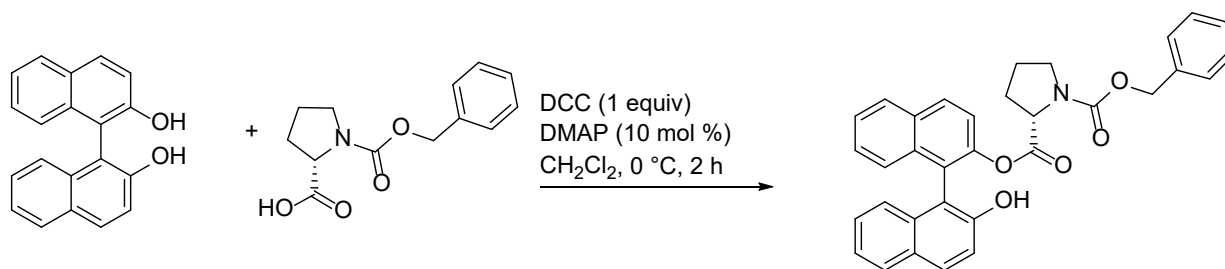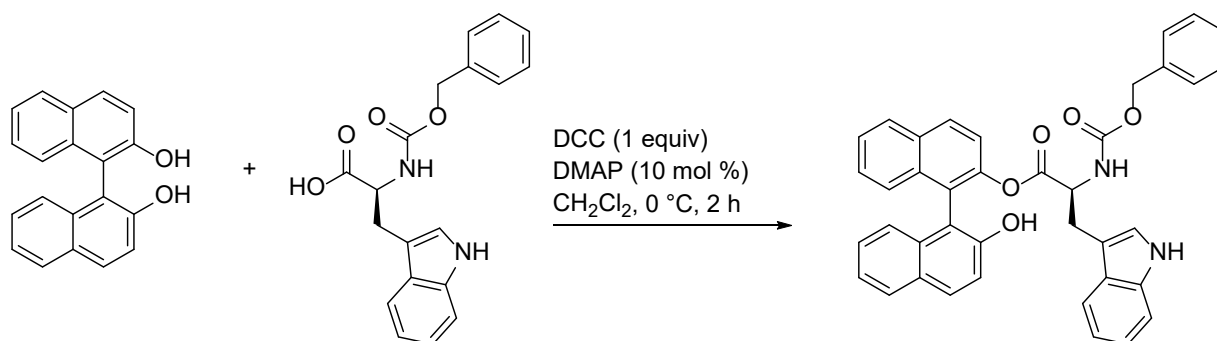

Figure 2.8 Synthetic scheme for Z-Trp-BINOL

Synthesis of Z-Trp-BINOL (7): (R/S)BINOL (100 mg, 0.349 mmol, 1 equiv), dicyclohexylcarbodiimide (0.086 mg, 0.419 mmol, 1.2 equiv), N,N-dimethylaminopyridine (0.005 mg, 0.042 mmol, 0.12 equiv), and N-[(Benzyloxy)carbonyl]-L-tryptophan (118 mg, 0.419 mmol, 1.2 equiv) were added to a 50mL three neck round bottom flask equipped with a magnetic stir bar. The flask was purged and backfilled with N_2 three times and submerged in an ice bath. 10 mL of cold CH_2Cl_2 (~0° C) was added via syringe to the reaction flask. Seconds to minutes after the solvent was added dicyclohexyl urea can be seen precipitating from solution. The solution was stirred at 0° C until TLC indicated that most or all of the BINOL had reacted (~2 hours). The reaction mixture was then rotary evaporated to remove 2/3^{rds} of the solvent volume, causing more dicyclohexyl urea to precipitate from solution. The resulting slurry was vacuum filtered and washed with three 5 mL portions of cold CH_2Cl_2. The filtrate was then rotary evaporated to dryness. A silica gel column was prepared by wet packing 12 grams of 400-600 mesh silica with hexanes in a 15 mm column. The crude product was wet loaded with minimal CH_2Cl_2 onto the column and eluted with 33% EtOAc/hexanes until the monosubstituted product

was obtained. The fractions were combined and evaporated to dryness to obtain **7** (0.138 g, 65% yield) as an off-white amorphous solid. ^{1}H NMR (400 MHz, Chloroform-d) δ 7.9 – 7.8 (m, 3H), 7.8 – 7.7 (m, 2H), 7.4 (dt, J = 8.2, 4.0 Hz, 1H), 7.3 – 7.1 (m, 13H), 7.1 (ddd, J = 8.2, 7.0, 1.3 Hz, 1H), 7.0 – 6.9 (m, 2H), 6.3 (d, J = 2.5 Hz, 1H), 5.6 (s, 1H), 4.9 (s, 2H), 4.8 (d, J = 7.8 Hz, 1H), 4.4 (td, J = 7.7, 4.8 Hz, 1H), 2.6 (dd, J = 15.2, 4.9 Hz, 1H), 2.3 (dd, J = 15.2, 7.7 Hz, 1H), 1.8 (dd, J = 12.5, 4.0 Hz, 1H), 1.6 (dddd, J = 13.3, 5.8, 3.9, 1.9 Hz, 1H). ^{13}C NMR (101 MHz, Chloroform-d) δ 171.0, 155.9, 151.9, 147.6, 136.1, 136.0, 133.6, 133.5, 132.3, 130.6, 130.5, 129.0, 128.5, 128.4, 128.2, 128.1, 128.1, 127.4, 127.3, 126.9, 126.3, 125.9, 124.8, 123.6, 123.0, 122.7, 122.2, 121.7, 119.6, 118.5, 118.3, 113.8, 111.2, 109.3, 67.0, 54.5, 49.2, 33.9, 26.6, 24.9. HRMS (ESI+) *m/z* calcd. For $C_{30}H_{29}NNaO_5$ ($[M+Na]^+$) 629.20524, found 629.20570.
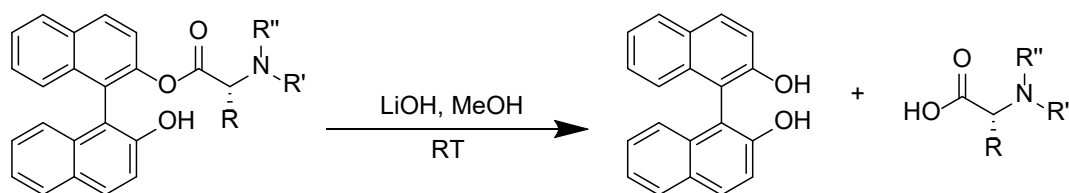
Figure 2.9 Synthetic scheme for the deprotection of amino acid substituted BINOL

~5mg of Boc-Pro-(S)-BINOL was dissolved in 1 mL of MeOH, then 0.1 mL of a 1 M solution of LiOH in MeOH was added and the solution was stirred at RT for 30 mins to 2 hours until TLC indicated completion of the reaction, as evidenced by the disappearance of the coupled BINOL and the reappearance of BINOL. The reaction was quenched by adding an equimolar amount of trifluoroacetic acid in MeOH. The reaction was stirred an additional 5 minutes and then evaporated to dryness. The resulting amorphous solid was dissolved in CH_2Cl_2 and run through a silica plug with CH_2Cl_2 until all the BINOL was eluted to yield (S)-BINOL in 90% yield with 100% ee.
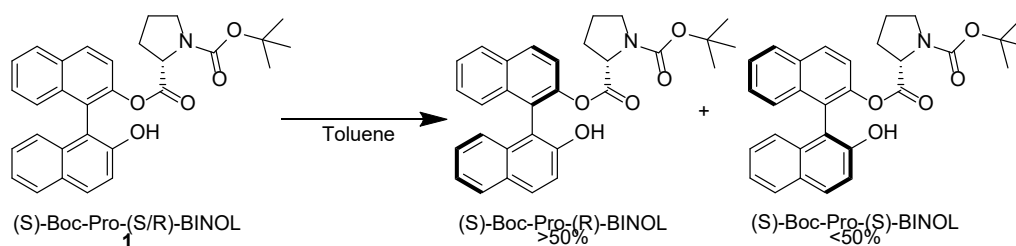
Figure 2.10 Synthetic scheme for the photo enantioenrichment of Boc-Pro-BINOL

5 mg of racemic Boc-Pro-(S/R)-BINOL added to test-tube with a magnetic stir bar. 1 mL of dry toluene and 0.1 mL of dry triethylamine were added to the test tube and the reaction vessel was capped with a rubber septum. The solution was vigorously stirred with a magnetic stir plate and irradiated with a 365 nm LED at 8 mW/cm^2 for 60 minutes. 0.1 mL aliquots were removed at 10, 20, 40, and 60 minutes. Each aliquot was evaporated to dryness, dissolved in 1 mL of toluene, then evaporated to dryness a second time to remove residual triethylamine. Silica gel columns were prepared by wet packing 400-600 mesh silica gel in 25% ethyl acetate in hexanes. Samples were dissolved in 1mL of 25% ethyl acetate in hexanes and flashed through the column. After separation, fractions containing Boc-Pro-BINOL were dried under reduced pressure. Purified samples were dissolved in 1mL of HPLC grade dichloromethane and analyzed by supercritical fluid chromatography.

2.2.2 Synthesis of BPI 1-4
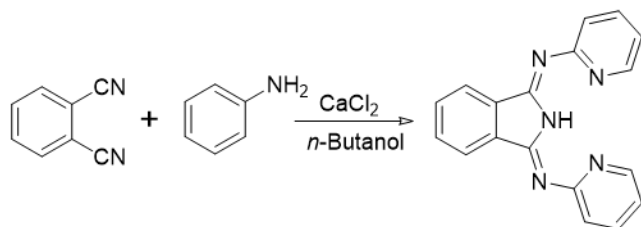
Figure 2.11 Synthetic scheme for BPI-1

28
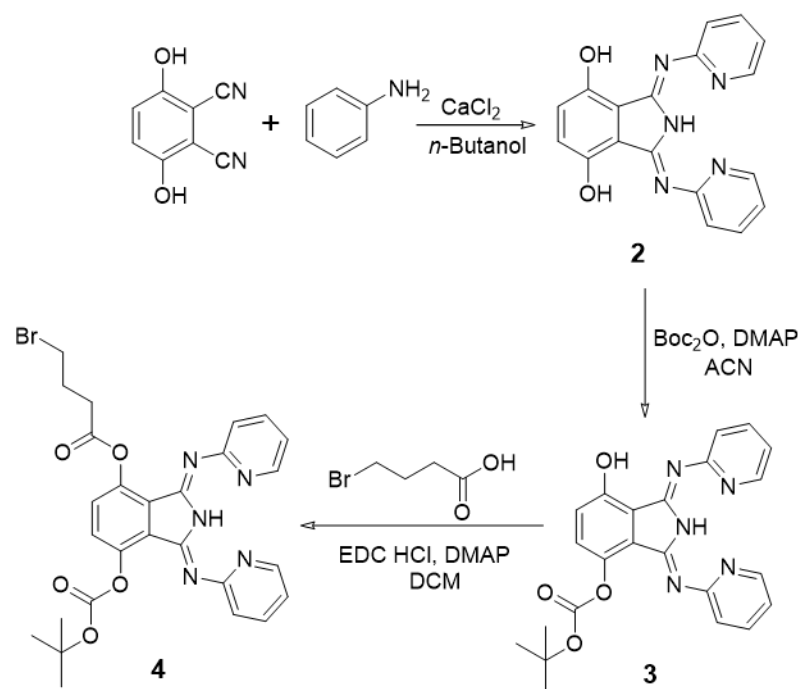
Figure 2.12 Synthetic scheme for BPI-2, BPI-3, and BPI-4

Synthesis of 2: 2,3-dicyanohydroquinone(500 mg, 3.12 mmol, 1 equiv), 2-aminopyridine(646 mg, 6.86 mmol, 2.2 equiv), CaCl$_2$(69 mg, 0.62 mmol 0.2 equiv), and *n*-butanol (20mL) were added to a 50 mL 3 neck round-bottom flask equipped with a magnetic stir-bar and reflux condenser. The flask was purged and backfilled with N$_2$ three times and then stirred at reflux for 20 days. The reaction was stopped despite the presence of unreacted starting material. After cooling to room temperature, the crude solution was poured into 500mL of water, and then filtered. The precipitate and then washed several times with water until no blue fluorescence from unreacted starting material was observed in the filtrate. The precipitate was then transferred to a 100mL round-bottom flask with 50mL of DCM and heated to reflux for 30 minutes and filtered. This was repeated 3 times. The DCM was removed by rotary evaporation. Recrystallization of the crude material in DCM/MeOH yielded long needle-like reddish-brown crystals of **2** which were filtered and dried in vacuo. Original recrystallization solution was concentrated then the recrystallization was repeated to yield a second crop of crystals. **2** (0.205 g, 19.8% yield).

Synthesis of 3: **2** (500 mg, 1.5 mmol), di-*tert*-butyl dicarbonate (489 mg, 2.24 mmol) and dimethylaminopyridine (DMAP) (182mg, 1.5 mmol) were added to a 250mL three neck round bottom flask equipped with a magnetic stir bar and dissolved in acetonitrile (100mL). The flask was purged and backfilled with N_2 three times and stirred at room temperature. The reaction progress was monitored by TLC. After 2 days the solvent was evaporated in vacuo and the crude mixture was purified by column chromatography on silica gel using a 10% ethylacetate in hexanes mobile phase. The fractions were combined and evaporated to dryness to obtain **3** (0.417 g, 65% yield) as a yellow amorphous solid.

Synthesis of 4: **3** (100 mg, 0.23 mmol), 4-bromobutanoic acid (50 mL, 0.48mmol), EDC HCl (114 mg, 0.59 mmol), DMAP (15.8 mg, 0.13 mmol) added to a 100mL three neck round bottom flask equipped with a magnetic stir bar and dissolved in dichloromethane (50mL). The flask was purged and backfilled with N_2 three times and stirred at room temperature. Reaction progress was monitored by disappearance of orange emission, which is indicative of the alcohol's protection. Once orange emission completely disappeared (~3 days), the reaction was quenched with 25 mL H_2O. The reaction crude was extracted 3x with DCM then concentrated in vaccuo. The crude material was recrystallized from DCM layered with hexanes. The crystals were filtered, rinsed with hexanes, then dried in vaccuo to yield **4** (0.102 g, 78% yield) as a pale yellow crystalline solid.

2.3   Experimental Techniques

2.3.1   Chiral Chromatography

Supercritical fluid chromatography (SFC) was performed using a JASCO SFC-4000 analytical SFC system with ~1mg/mL of sample in HPLC grade solvent.

2.3.2   Solution State Absorption

Solution state absorption spectra were recorded using an Agilent 8453 UV-visible photo diode array spectrophotometer. Extinction coefficients were determined from the absorption

spectra of solutions with a known concentration of analyte in a 1×1 cm special optical glass cuvette from Equation 2.1.

$$A = -\log(T) = \varepsilon b c \qquad (2.1)$$

2.3.3 Circular Dichroism Spectroscopy

Circular Dichroism spectra were obtained using an AVIV 202 CD spectrometer with a 2 mm $\times$ 1 cm quartz cuvette.

2.3.4 Nuclear Magnetic Resonance Spectroscopy

^{1}H and ^{13}C nuclear magnetic resonance spectra were recorded on a Bruker 400 MHz spectrometer. Chemical shifts for protons are reported in parts per million (ppm) relative to residual solvent peak ($CHCl_3$ = 7.26 (s) ppm,). Chemical shifts for ^{13}C are reported in parts per million (ppm) relative to residual chloroform peak (77.16 ppm).

2.3.5 Steady State Emission Spectroscopy

Steady state emission data was collected using an Edinburgh FLS980 fluorescence spectrometer at room temperature. A housed 450 W Xe lamp/single grating (1800 λ/mm, 250 nm blaze) Czerny–Turner monochromator was used as an output to excite the samples. Emission from the sample was passed through a single grating (1800 λ/mm, 500 nm blaze) Czerny–Turner monochromator and then detected by a Peltier-cooled Hamamatsu R928 photomultiplier tube. Solution state emission samples were contained in a 1×1 cm special optical glass cuvette. Solid state emission samples were sandwiched between two 2 x 2 cm glass slides and placed at an ~45-degree angle relative to the incident excitation source.

2.3.6 Emission Lifetime Measurements

Solution emission lifetimes were monitored by using the FLS980's time-correlated single-photon counting capability (1024 channels; 200 ns window) with data collection for 10,000 counts. Excitation was provided by an Edinburgh EPL-360 picosecond pulsed diode laser (360 ± 10 nm, 892 ps FWHM) operated at 10 MHz. Emission from the sample was passed through a single grating (1800 l/mm, 500 nm blaze) Czerny-Turner monochromator (0.75 nm bandwidth) and finally detected by a peltier-cooled Hamamatsu R928 photomultiplier tube. Kinetics were fit with a single exponential function by using Edinburgh software package. Solution state emission samples were contained in a 1×1 cm special optical glass cuvette. Solid state emission samples were sandwiched between two 2 x 2 cm glass slides and placed at an ~45-degree angle relative to the incident excitation source.

2.3.7 Absolute Emission Quantum Yields

Absolute Emission quantum yields were acquired using a Quantaurus Absolute PL Quantum Yield Spectrometer (Hamamatsu). Liquid samples were prepared with an A < 0.1 in a 1 cm cuvette) and then transfer to a 12.5 cm long, 0.8 cm diameter quartz tube with a round bottom and a rubber septa cap for data acquisition. Solid samples were prepared by adding a small amount to the tube then rolling the sample to coat the walls of the tube. A similar tube was used as a reference with the same volume for solutions, or air for solids. Samples and reference were excited with 360 nm light and the excitation and emission intensities recorded at 1 nm step intervals from 340 to 900 nm. Quantum yields were then calculated using the De Mello method. Emission quantum yields were reproducible to within ±1% across several different measurements and at least three independently prepared samples.

2.3.8 Single Crystal X-ray Diffraction

Single crystal X-ray diffraction was performed using a Rigaku XtaLAB diffractometer, using CuKα radiation at 100 K. structure solution and least square refinements were performed in SHELXL. Due to the resolution of the data, the carbons in the central rings were not located

accurately. Crystal Models were constructed in Materials Studio Modeling Suit (v 8.0, BIOVIA Software Inc. San Diego CA 2014) utilizing the experimental crystal data as a starting point. Geometry optimizations were performed in the Forcite module utilizing the universal force field (UFF).H and ^{13}C nuclear magnetic resonance spectra were recorded on a Bruker 400 MHz spectrometer. Chemical shifts for protons are reported in parts per million (ppm) relative to residual solvent peak ($CHCl_3$ = 7.26 (s) ppm,). Chemical shifts for ^{13}C are reported in parts per million (ppm) relative to residual chloroform peak (77.16 ppm).

2.3.9 Powder X-Ray Diffraction

Powder X-ray diffraction measurements were performed using a Rigaku Miniflex 600 diffractometer, with θ - 2θ Bragg-Brentano geometry, and a 600 W (40 kV, 15 mA) Cu X-ray tube source using Kα (λ = 1.5418 Å) radiation. Samples were measures from 3 to 80 2θ-degrees with a step size of 0.02º and a scan rate of 1.5 s per step. Samples were prepared by dropping the powder sample in a Si zero background plate and pressing the powder with a razor blade spatula till smooth. Measurements were performed under spinning. Rietveld refinement was processed in GSAS II.

2.3.10 N$_2$ Gas Adsorption Isotherm Analysis

N_2 gas adsorption isotherm analysis was performed using a Micromertics ASAP 2020 porosimetry analyzer. The measurements were performed at 77 K. Mass spectra were recorded on a JEOL (Toyko, Japan) AccuTOF-LP 4G™, model JMS-T100LP mass spectrometer (JMS-4000LC) coupled with an IonSense (Peabody, MA) DARTSVP® ionization source. Helium gas was used as the DART ionization gas at a flow rate of approximately 3.6 L/min. The gas temperature was maintained at 500 °C. The needle electrode potential and exit grid voltage were held at 2 kV and 250 V, respectively, for the positive ionization mode. Fourier-transform infrared spectra were recorded using a Perkin Elmer Spectrum ONE Universal FT-IR ATR. A total of 32 transients were collected for each sample with a resolution of 0.05 cm^{-1} between 4000-650 cm^{-1}.

CHAPTER 3

ENANTIOSELECTIVE PROTONATION OF SILYL ENOL ETHER USING EXCITED STATE PROTON TRANSFER DYES

3.1   Introduction to Enantioselective Proton Transfer

Enantiopure excited state proton transfer (ESPT) dyes were used for the asymmetric protonation of silyl enol ether. Under 365 nm irradiation, with 3,3′-dibromo-VANOL as the ESPT dye, up to 49% enantioselectivity with a 68% yield of product was observed at room temperature. The reaction is effective with a range of silyl enol ethers and can also be achieved with visible light upon the addition of triplet sensitizer. The relatively low ee of the protonated product is due to the racemization/decomposition of the ESPT dye in the excited state as indicated by circular dichroism, HPLC, and UV−vis spectroscopy.
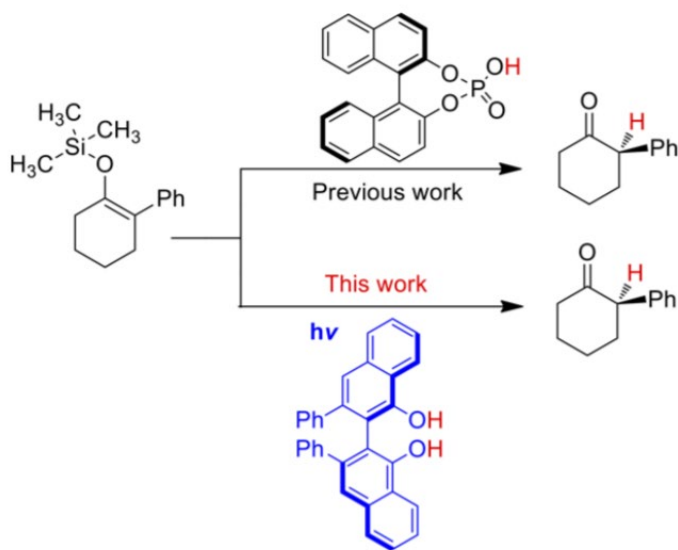
Figure 3.1 Enantioselective protonation of 1-phenyl-2-(trimethylsiloxy)cyclohexene to generate (R)-2-phenylcyclohexanone

Enantioselective synthesis is the cornerstone of modern synthetic chemistry and a crucial step in the production of fine chemicals such as food additives, fragrances, natural products, and

pharmaceuticals.[72] Historically these reactions are thermally driven, but over the past decade there has been an increased interest in enantioselective photocatalysis because the reactions can proceed at room temperature and they use light as a nontoxic reagent.[73] Most of these asymmetric, photocatalytic reactions rely on either (1) triplet energy transfer to generate a reactive organic substrate[74] or (2) photoredox reagents such as ruthenium(II) tris(2,2′-bipyridine),[75-77] acridinium,[78] iridium complexes,[79] and eosin[80] which, upon excitation, can initiate a wide range of chemical transformations by facile, one-electron oxidation or reduction events.

3.2   Experimental
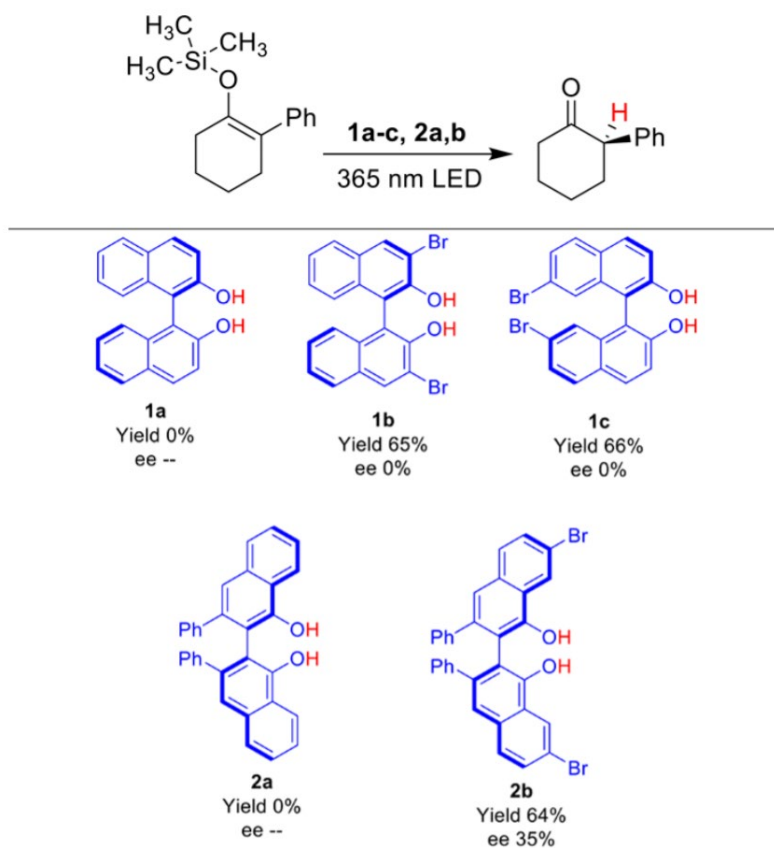
Figure 3.2 Excited state proton transfer dyes, reaction yield, and enantiomeric excess of (R)-2-Phenylcyclohexanone[a] reaction conditions: 1 mM of 1-phenyl-2-(trimethylsiloxy)cyclohexene and 1 mM of (R)-ESPT dye in 0.5 mL of toluene with 365 nm irradiation (8 mW/cm^2); yields were calculated by ^{1}H NMR using triphenylmethane as the internal reference; ee's were determined by HPLC (OD chiral column, flow rate 1 mL/min, hexane/isopropanol = 99:1).

Recently our research group introduced excited state proton transfer (ESPT), in the presence of a sacrificial proton source, as an alternative photocatalytic strategy which relies on the electron density shift associated with light absorption to increase the acidity of the catalyst significantly.[62] Greater than 95% efficient photocatalytic protonation of a silyl enol ether was achieved with 1 mol % 7-bromo-2-naphthol as an ESPT catalyst and phenol as the sacrificial proton source.[62] Although there is a stereocenter, the achiral reaction conditions generate a racemic mixture of (R)- and (S)-2-phenylcyclohexanone as the product.

Enantioselective protonation of prochiral enol ether is a simple and attractive route for the generation of optically active carbonyl compounds.[81] This protonation reaction has been performed using chiral phosphoric acids (top of the Figure 3.1),[82] chiral BINOL Sn complexes,[83] and organocatalysts.[84] In this report we demonstrate that chiral naphthol compounds can facilitate enantioselective ESPT to a prochiral silyl enol ether substrate at room temperature (bottom of Figure 3.1). Enantioselective ESPT has been used for the chiral recognition of enantiopure amino acids,[85, 86] amino alcohols,[87, 88] amines,[89] or alcohols,[90] but to the best of our knowledge, this is the first example of applying ESPT to a prochiral substrate for the generation of chiral product.

BINOL and VANOL compounds (Scheme 1) were selected for this work because (1) they contain naphthol chromophoric units which are known to exhibit ESPT[2, 91, 92] and (2) they are relatively common molecules for use in enantioselective reactions because of their axial chirality.[93-96]

Photochemical reactions were performed with a stoichiometric mixture of 1-phenyl-2-(trimethylsiloxy)cyclohexene and enantiopure ESPT dye (1a−c and 2a−b) in toluene under 365 nm irradiation (8 mW/cm^2) for 2 h. The reaction yields and ee of 2-phenylcyclohexanone were determined by NMR and HPLC, respectively.

3.3   Results and Discussion

There are several notable observations from the yield and ee shown in Figure 3.2. The first is that the unsubstituted BINOL (1a) and VANOL (2a) compounds yielded no product. In contrast, bromine substituted compounds 1b, 1c, and 2b, gave product in >60% yield. This result is in agreement with our previous report where the generation of a triplet excited state was necessary for diffusion limited contact and ESPT to occur.[62] The addition of bromine heavy

atoms (1b, 1c, and 2b) effectively facilitates intersystem crossing into the long-lived triplet excited state which can undergo chemical reactions.[97, 98]

Of the ESPT dyes in Scheme 1 only 2b exhibited any enantioselectivity (35% ee) for the protonation of 1-phenyl-2- (trimethylsiloxy)cyclohexene. Despite the high yield, no ee was observed for 1b and 1c. As previously reported by Tolbert,[99] Wan,[100] and others,[101] BINOL planarizes in the excited state and can subsequently racemize. Presumably either (1) the lack of asymmetric induction from the planarized excited state or (2) racemization prior to proton transfer is responsible for the lack of enantioselectivity during the ESPT reaction with 1b and 1c. Our initial attempts to hinder planarization/racemization by substituting BINOL with more sterically hindered bromine atoms in the 7,7′ position did not increase the ee of reactions with 1c. However, with (R)-3,3′-dibromoVANOL (2b) a 64% yield (61% isolated yield) with 35% enantioselectivity of (R)-2- phenylcyclohexanone was obtained. The significant increase in steric hindrance provided by the phenyl substituents likely impedes rotation/planarization of VANOL in the excited state.

Table 3.1 Reaction conditions for the protonation of 1- Phenyl-2-(trimethylsiloxy)cyclohexene by 2b [a]All of the reactions were carried out with 1mM of the substrates and 1mM of **2b** with 365 nm irradiation (8 mW/cm^2) for 2 hours; [b]Yield of the product was calculated by ^{1}H NMR using triphenylmethane as the internal reference; [c] Determined by HPLC (OD chiral column, Flow rate 1 mL/min, Hex:IPA = 99:1).

entry	solvent	hν (nm)	temp ($^\circ$C)	yield (%)[b]	ee (%)[c]
1	toluene	-	60	0	nd
2	toluene	-	rt	0	nd
3	toluene	365	rt	64	35
4	toluene	365	0	72	35
5	toluene	365	-5	70	36
6	toluene	365	60	76	32
7	MeCN	365	rt	64	0
8	CHCl$_3$	365	rt	80	0

Various conditions for the protonation of 1-phenyl-2- (trimethylsiloxy)cyclohexene by 2b were examined, and the results are summarized in Table 3.1. In the absence of light, 2b is not sufficiently acidic to protonate the substrate and generate any observable 2-phenylcyclohexanone even at elevated temperatures (entries 1−2 in Table 3.1). Under irradiation, increasing (60 °C) or

decreasing (−5 °C) the reaction temperature had minimal effect on the reaction yield or the enantioselectivity (entries 4−6). The nature of the solvent had minimal influence on the reaction yield with only a small decrease in CHCl$_3$ (80%) relative to toluene (64%). However, in both MeCN and CHCl$_3$ no enantioselectivity is observed. Although we do not have a definitive explanation for the loss in enantioselectivity, it may be due to the increase polarity of MeCN and CHCl$_3$ effectively solvating the acidic proton and decreasing substrate−dye contact during the proton transfer event.
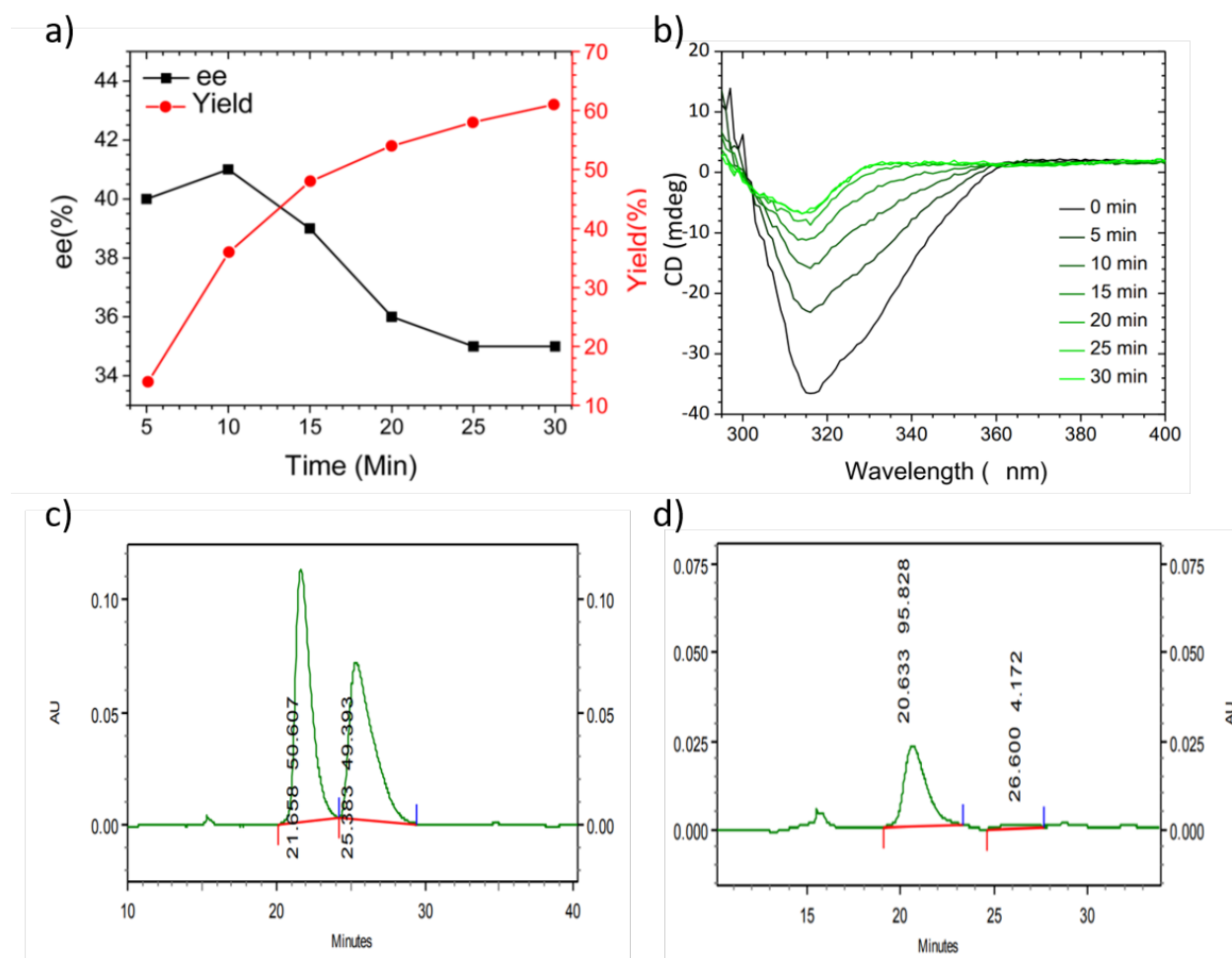
Figure 3.3 a) Reaction yield and ee of 2-phenylcyclohexanone with respect to time for a reaction mixture containing 1 mM of 1-phenyl-2- (trimethylsiloxy)cyclohexene and 1 mM of (R)-2b in 0.5 mL of toluene under 365 nm irradiation (8 mW/cm^2). b) Circular dichroism (CD) spectra of a 1 × 10^{-3} M 2b and 1 × 10^{-3} M 1-phenyl-2- (trimethylsiloxy) cyclohexene in toluene at different time intervals of irradiation with 365 nm light. c) . HPLC of a racemic mixture of (R)- and (S)-VANOL, and d) after 10 minutes of irradiation of a 1 × 10^{-3} M 2b and 1 × 10^{-3} M 1-phenyl-2- (trimethylsiloxy) cyclohexene in toluene.(Chiralcel OD, Hex: Isopropanol=99:1, Flowrate=0.8 mL/min)

To gain insights into the progress of the reaction we have monitored both ee and yield with respect to time, and the results can be seen in Figure 3.2. As expected, the reaction yield continues to increase over the course of the reaction. In contrast, for the first 10 min of the reaction the ee is >40% and then decreases to ~35% over the subsequent 20 min.

The decrease in ee as the reaction progresses can be attributed to a decrease in enantiopurity and/or decomposition of 2b over the course of the experiment. Changes in the circular dichroism spectra with respect to time indicate that more than 50% of the initial CD intensity is lost within the first 10 min (Figure 3.3b) and continues to decrease for at least the first 30 min. HPLC measurements after 10 min of irradiation show the generation of ~5% (S)-VANOL (Figure 3.3d). Conversely, changes in the UV−vis spectra over time show the disappearance of VANOL absorption features over the course of the reaction. These results suggest that, while slower than with BINOL, both isomerization and decomposition of VANOL contribute to the decreased ee over time.

Enantioselective ESPT was effective with a range of silyl enol ethers as summarized in Table 3.2. In accord with our previous report, the R1 substituent had minimal influence on the reaction. However, we observe a >30% decrease in ee as the steric bulk is increased from methyl to ethyl and isopropyl groups. The highest ee we report here, 49%, was achieved with a

Table 3.2 Reaction yield and ee for various silyl enol ethers.[a]

entry	R_1	yield (%)[b]	ee (%)[c]
1	-CH$_3$	64	35
2	-C$_2$H$_5$	64	20
3	-CH(CH$_3$)$_2$	78	25
4	-C$_6$H$_5$	68	49
5	(trimethylsiloxy)indene	80	13
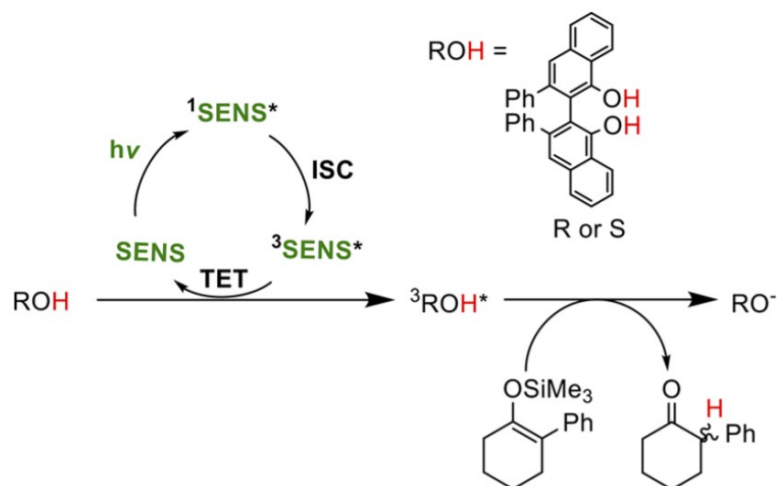
Figure 3.4 Sensitized enantioselective proton transfer under visible light (445 nm). SENS = Bis(4,6-difluorophenylpyridine) (picolinate)- iridium(III).

triphenylsilyl group. Interestingly, with 2-methyl-3-(trimethylsiloxy)indene we observe the highest reaction yield (80%; 74% isolated yield) but the lowest ee (13%).

In accord with our previous work, enantioselective ESPT can also be achieved under visible light by using the appropriate triplet sensitizer molecule and the unsubstituted ESPT dye by triplet energy transfer (TET) (Figure 3.4). Irradiating a mixture of substrate (1 mM), VANOL (2a, 1 mM), and bis(4,6- difluorophenyl-pyridine)(picolinate)iridium(III) (SENS, 0.05 mM) in 0.5 mL of toluene with 445 nm light gave (R)-2- phenylcyclohexanone in 68% yield and 25% ee. The same reaction with (S)-VANOL yielded (S)-2-phenylcyclohexanone in similar yield and ee. It is worth emphasizing that the sensitized reactions are achieved using the nonbrominated ESPT dye since the triplet state is generated on the sensitizer and then transferred to the dye. Initial attempts to realize enantioselective ESPT catalysis have been unsuccessful. In our previous report ESPT catalysis was demonstrated with phenol as the sacrificial proton source to regenerate 7-bromo-2-naphthol (1 mol % relative to substrate) after the proton transfer event.[62, 81] Similar catalytic protonation of substrate by 2b in the presence of phenol was observed, but the reaction was not enantioselective. Our working hypothesis is that hydrogen bonding between 2b and phenol in the ground state is responsible for the loss of ee. That is, upon excitation, ESPT from 2b to phenol can generate $PhOH_2^+$ which is still sufficiently acidic to protonate substrate, but all chiral induction is lost.[82] Attempts to limit hydrogen bonding by using thiol proton sources (ethanethiol, thiophenol, etc) or the sterically hindered 2,6-di-tert-butyl-methylphenol

yielded no product and no enantioselective product, respectively. In the former case, insoluble brown precipitation was quickly generated, likely due to the formation of sulfide adduct by photoinitiated radical reaction of thiols.[102] Presumably with an achiral sacrificial proton donor that lacks hydrogen bonding and has the appropriate pK_a to regenerate the ESPT dye but not protonate substrate, enantioselective ESPT catalysis could be realized.

In summary we have introduced a new strategy to enantioselectively protonate prochiral substrates using excited state proton transfer from a chiral dye. The reaction is effective with a range of silyl enol ethers and can also be achieved with visible light upon the addition of triplet sensitizer. The low ee of the protonated product is due to the racemization of the ESPT dye in the excited state as indicated by circular dichroism. The development of new enantiopure ESPT dyes that cannot photoisomerize will likely improve the ee and increase the utility of enantioselective ESPT in organic synthesis.

CHAPTER 4

ENANTIOENRICHMENT OF RACEMIC BINOL BY WAY OF EXCITED STATE PROTON TRANSFER

4.1   Introduction to Enantioenrichment of Racemic BINOL

Here we report a method for enantioenriching BINOL using a chiral auxiliary and an excited state proton transfer (ESPT) event. Regardless of the starting enantiomeric excess (ee),
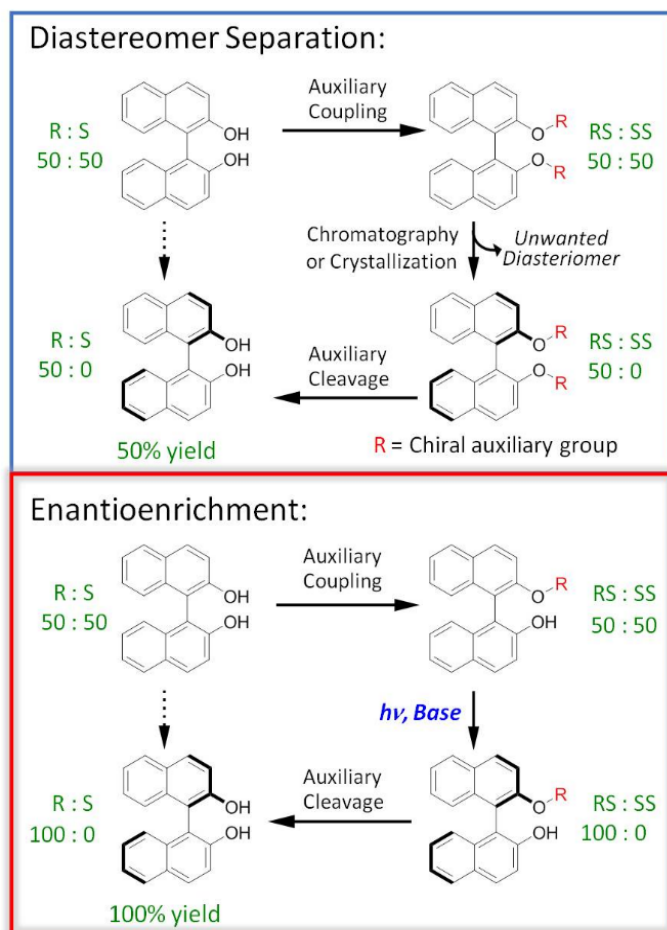
Figure 4.1 Strategies for generating enantiopure BINOL with the maximum theoretical yields in green.

after irradiation the solution reaches a photostationary state whose ee is dependent solely on the identity of the chiral auxiliary group. The enantioenriched BINOL is easily recovered by cleaving the auxiliary group in mild conditions.

Enantioselective reactions are the cornerstone of modern synthetic organic chemistry[104, 105] and are crucial to obtaining enantiopure molecules for applications ranging from fragrances to pharmaceuticals.[72] Asymmetric catalysis, the most popular method of enantiogenesis, commonly employs catalytic coordination complexes composed of a transition metal surrounded by chiral ligands. Of the classes of chiral ligands, BINOL ([1,1'-binaphthalene]-2,2'-diol) and its derivatives, are arguably the most popular chelates and have been critical for the development of a wide range of asymmetric catalytic reactions.[93, 106] The utility and effectiveness of these reactions is directly dependent on obtaining enantiopure BINOL.

Enantiopure BINOL is typically generated by resolving racemic mixtures of enantiomers (chiral resolution) or by asymmetric synthesis.[75] Chiral chromatography of BINOL[107] as well as standard chromatography[108] or crystallization[109] of diastereomeric mixtures of functionalized BINOL (Figure 4.1a) are an effective means of purification but these techniques typically require large quantities of solvent and at least 50% of the starting material (i.e. the unwanted enantiomer) is unused. Asymmetric synthesis requires one or more additional synthetic steps and either an enzyme[110] or a chiral organometallic catalyst which itself must be prepared with high enantiopurity.[111, 112] Here we introduce a new, light driven method for the generation of enantiopure BINOL from a mixture of diastereomers by way of excited state proton transfer (ESPT).

ESPT is a process where photoexcitation of a dye increases the acidity of the molecule by upwards of 13 pK_a units and consequently, it can transfer a proton to a base.[3] Recently, our group demonstrated that ESPT dyes can be used to catalytically[62] and enantioselectively[71] protonate silyl enol ethers after either direct or sensitized excitation. The latter reaction relied on enantiopure naphthol derivatives, VANOL[113] and BINOL,[97, 99] which have axial chirality. Interestingly, both ESPT dyes yielded ~65% of the protonated product but the enantiomeric excess (ee) was 49% and 0% for VANOL and BINOL respectively.

In retrospect the 0% ee for BINOL is not surprising given that BINOL is known to planarize and subsequently isomerize in the excited state. Tolbert, Wan, and others have demonstrated that ESPT from BINOL to a base is a necessary step in the isomerization process.[99, 100] While these planarization and isomerization events are not ideal for enantioselective ESPT reactions, here we demonstrate that it offers a new method of dynamically enantioenriching BINOL by using bulky chiral directing groups to influence the equilibrium of the photostationary state (bottom of Figure 1). Boc-Pro-BINOL (Table 1), was selected as the prototypical molecule for this study because it can be readily generated by mixing (R/S)-BINOL and (S)-Boc-Pro-OH with dicyclohexylcarboimide and N,N-dimethylaminopyridine in CH_2Cl_2 at

Table 4.1 [a] 10 mM Boc-Pro-(R/S)-BINOL in toluene under 365 nm irradiation (8 mW/cm^2) at room temperature for 60 minutes with stirring unless otherwise noted. [b] 10mM solution of Boc-Pro-OH and (R/S)-BINOL. [c] Resulted in Boc-Pro- cleavage. [d] ee reported for the (R)-BINOL as determined using SFC (Daicel CHIRALPAK® IA column, 35% CH_2Cl_2 in CO_2, 1.5 mL/min flow rate). [e] ee is for unprotected BINOL.

(S)-Boc-Pro-(R/S)-BINOL **1** → Toluene → (S)-Boc-Pro-(R)-BINOL ≥50% + (S)-Boc-Pro-(S)-BINOL ≤50%
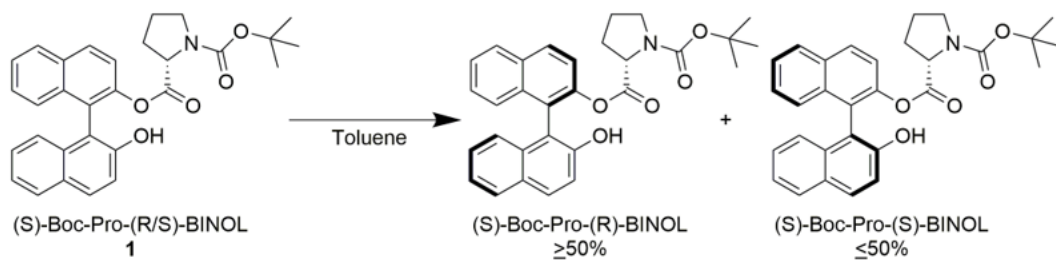
entry	hν (nm)	Et₃N	temp (°C)	yield (%)	ee (%)[d]
1	365	0.1mL	rt	86	31
2	-	0.1mL	rt	82	-5
3	365	-	rt	100	2
4	-	0.1mL	100	-[c]	0[e]
5[b]	365	0.1mL	rt	21	5[e]

0° C.[114] The selective addition of only one Boc-Pro group is convenient because at least one OH group of BINOL must be present for ESPT to occur.[99]

For the photoreaction, a mixture of Boc-Pro-(R/S)-BINOL (1:1 ratio of (R)- and (S)-BINOL) and triethylamine (Et₃N) in toluene were irradiated with 365 nm light (8 mW/cm^2) at

room temperature for 60 minutes. Upon completion, the product was recovered in an 86% isolated yield with a 31% ee of (R)-BINOL as indicated by chiral supercritical fluid chromatography.
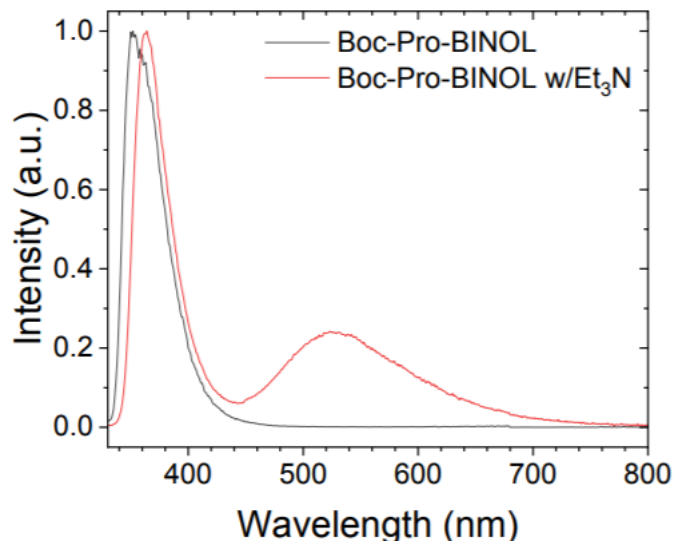
Figure 4.2 Emission spectra for Boc-Pro-BINOL in toluene with and without Et3N (λex = 320 nm).

The control experiments, summarized in Table 4.1, indicate that a notable ee is only achieved when both light and base are present during the reaction. Even at elevated temperatures (100° C) no ee, and presumably no isomerization, was observed supporting that this is a light driven process. This result was expected due to the high rotational barrier of BINOL in the ground state ($\Delta G^{\ddagger}$ rac 38 kcal/mol in diphenylether).[115] An ~30% ee was observed for the reaction at 0°C which is within the experimental error (±3%) the same as at room temperature. This observation is not surprising given that for a ΔG of 0.2 kcal/mol (vida infra), a 25° C change in temperature is insufficient to shift the equilibrium constant (i.e. the ee) to beyond the measurement error. Attempts to perform the reaction at lower temperatures (<0° C) were hindered by light scattering due to water condensation and dramatically lengthened reaction times. It is worth noting that for a mixture of Boc-Pro-OH and BINOL (Table 4.1, entry 5) a negligible change in ee was observed suggesting that proximity of the chiral auxiliary and the BINOL molecule are necessary for enantioenrichment.

Table 4.2 [a]10 mM Boc-Pro-(S/R)-BINOL under 365 nm irradiation (8 mW/cm^2) at room temperature for 60 minutes with stirring. [b]ee was determined using SFC (Daicel CHIRALPAK® IA column, 35% CH$_2$Cl$_2$ in CO$_2$, 1.5 mL/min flow rate). [c]Boc-Pro-BINOL was insoluble at the standard solvent volume, therefore 3mL of hexanes and 0.3mL of triethylamine was used to fully dissolve the compound.

Solvent	ee **1R** (%) @ 20 mins[b]	ee **1R** (%) @ 60 mins[b]
Toluene	15	31
Mesitylene	8	17
Hexanes[c]	10	24
MeCN	7	13
THF	15	17
MeOH	4	2
CH$_2$Cl$_2$	18	18

Boc-Pro-BINOL in toluene exhibits a single emission peak at 350 nm but upon addition of Et$_3$N, a second low energy emission feature is observed at ~445 nm (Figure 4.2). Dual features are consistent with emission from the high energy protonated (–OH) and low energy deprotonated (–O⁻) forms of the dye. This dual emission, the lack of reaction in the absence of base, as well as previous literature all indicate that an ESPT event is critical in initiating the isomerization reaction.

Of the solvents tested (THF, MeOH, hexanes, mesitylene, MeCN, toluene, and CH$_2$Cl$_2$) toluene resulted in the highest ee (Table 4.2). The solvent will influence the excited state

Table 4.3 Enantioenrichment of Boc-Pro-BINOL with various bases. [a]10 mM Boc-Pro-(S)-BINOL under 365 nm irradiation (8 mW/cm^2) at room temperature for 60 minutes with stirring. [b]ee was determined using SFC (Daicel CHIRALPAK® IA column, 35% CH$_2$Cl$_2$ in CO$_2$, 1.5 mL/min flow rate).

Base[a]	Volume added (mL)	ee (%) at 60 mins[b]
Triethylamine	0.100	17 of R
Diisopropylamine	0.125	26 of S
Pyridine	0.058	84 of S
Isopropylamine	0.061	76 of S
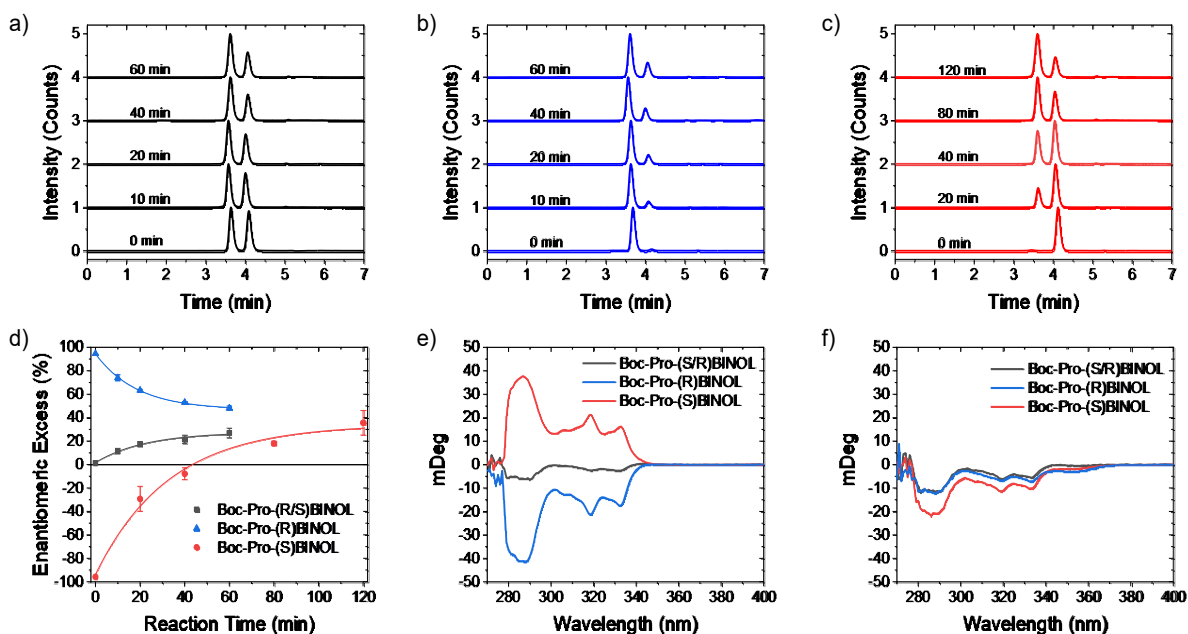
Figure 4.3 The photoreaction 10mM Boc-Pro-BINOL solution, with 0.1mL NEt$_3$ in toluene under 365 nm irradiation (8 mW/cm^2) at room temperature with respect to time. (a-c) Normalized SFC traces (Chiralpak IA column, 35% CH$_2$Cl$_2$ in CO$_2$, 1.5 mL/min flow rate) for the photodynamic resolution of 10mM Boc-Pro-(R/S)-BINOL (a), Boc-Pro-(R)-BINOL (b), and Boc-Pro-(S)-BINOL (c). d) Enantiomeric excess with respect to time for 10mM Boc-Pro-(R/S)-BINOL (black squares), Boc-Pro-(R)-BINOL (blue circle), and Boc-Pro-(S)-BINOL (red triangle). Each data point is the average of 3 independent trials with the error bar representing the standard deviation. (e-f) Circular dichroism spectra collected from 10mM Boc-Pro-(R/S)-BINOL (black), Boc-Pro-(R)-BINOL (blue), and Boc-Pro-(S)-BINOL (red) before (e) and after (f) photodynamic resolution.

lifetime, pK$_a$*, the ΔG between the excited isomers, and other factors, but the primary driver dictating ee with respect to solvent is currently unclear to us. The triethylamine also influences the rate of the reaction and side product generation (vida infra) with a 10:1 Et$_3$N to substrate ratio reaching the photostationary state in the least amount of time (Table 4.3).

Upon completion of the reaction, unsubstituted BINOL can readily be obtained by cleaving the amino acid group following literature procedure.[114] Briefly, LiOH in MeOH was added to the dried crude mixture, followed by reaction quenching with TFA, solvent evaporation, and finally passing the residue through a silica plug eluting with CH$_2$Cl$_2$. ^{1}H NMR and SFC confirmed the purity of the BINOL and the retention of ee during the deprotection process.

To confirm that the reaction had reached a photostationary state, we monitored the ee of three different samples, Boc-Pro-(R/S)-BINOL, enantiopure Boc-Pro-(R)-BINOL, and

enantiopure Boc-Pro-(S)-BINOL, over the course of the reaction using SFC. As can be seen in Figure 2a-c, regardless of the starting point, all three samples converge on an ee of 25-35%. Circular dichroism spectra recorded before and after irradiation are in agreement with the results obtained by SFC. These observations strongly indicate that the ee is determined by the equilibrium between the excited states of Boc-Pro-(S)-BINOL and Boc-Pro-(R)-BINOL and not simply preferential decomposition or reaction of one of the isomers.
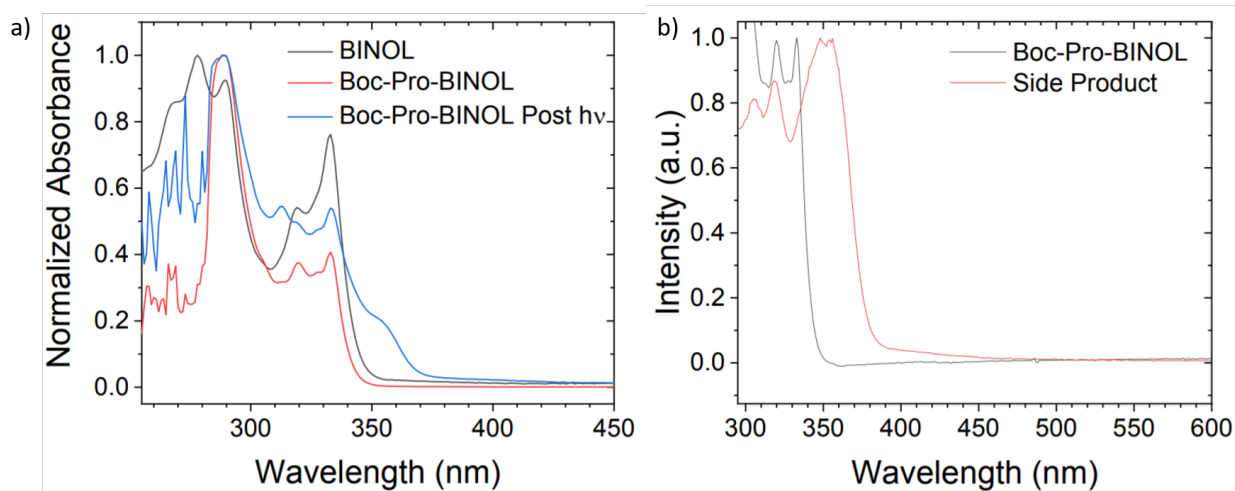
Figure 4.4 [a] UV-Vis absorption spectrum of BINOL, Boc-Pro-BINOL, and Boc-Pro-BINOL after 60 minutes of irradiation with 365nm at 8mW/cm^2. Spectra were normalized to set the λ_{max} = 1. The peak that appears at 360 nm after irradiation corresponds to the photodecomposition product responsible for the internal filtering effect. [b] UV-Vis absorption spectra of Boc-Pro-BINOL and isolated side product (Rf = 0.5 in 20% EtOAc/80% Hexanes) after 4 hours of photolysis.

For both Boc-Pro-(R/S)-BINOL and Boc-Pro-(R)-BINOL the photostationary state is achieved in <60 minutes. In contrast the Boc-Pro-(S)-BINOL diastereomer required longer irradiation times presumably because it is the furthest from the photostationary state. It is important to note that during initial measurements of the R diastereomer, the ee plateaued at ~10% and was accompanied by a change in the solution from colourless to yellow. UV-Vis spectra of the solution showed the presence of a new absorption feature at 360 nm (Figure 4.4) that is not associated with Boc-Pro-(R/S)-BINOL. A similar species was observed by Tolbert and co-workers and was attributed to a photodecomposition product of the ESPT reaction.[99, 100] The concentration of this impurity is low but its high extinction coefficient at 365 nm results in an optical filtering effect that significantly hinders the desired photoreaction.

To ensure that the Boc-Pro-(R)-BINOL has reached equilibrium the yellow impurity was removed by passing the solution through a silica plug, rinsing with CH_2Cl_2, evaporating the solvent, adding toluene and Et_3N, and then resuming irradiation under the original reaction conditions. Presumably the same impurity is formed during the Boc-Pro-(R/S)-BINOL and Boc-Pro-(S)-BINOL reactions but they reach equilibrium before the filtering effect significantly hinders the reaction. A structure for this impurity has been suggested.[99, 100] Definitively establishing the nature of the decomposition product, its reaction rate and mechanism will likely be crucial to the viability of this separations strategy but is beyond the scope of the current work.

4.3   Substrate Scope

To determine the influence of the chiral auxiliary on the resulting ee, we generated a series of BINOL derivatives as depicted in Figure 4.5. The menthyl carbonate (2)[116] substituted BINOL was prepared following variations of previously published procedures. The remaining compounds with amino acid groups (3-7) were prepared following a similar procedure to Boc-Pro-BINOL[114] with experimental details provided in Chapter 2. Despite the syntheses of these compounds being performed using racemic BINOL, we found some degree of selectivity resulting in a small ee even before irradiation (ee (%) 0 min in Table 4.4). Given that the photoreaction is dictated by the excited state equilibrium, we do not expect that the variation in starting points influences the resulting ee.
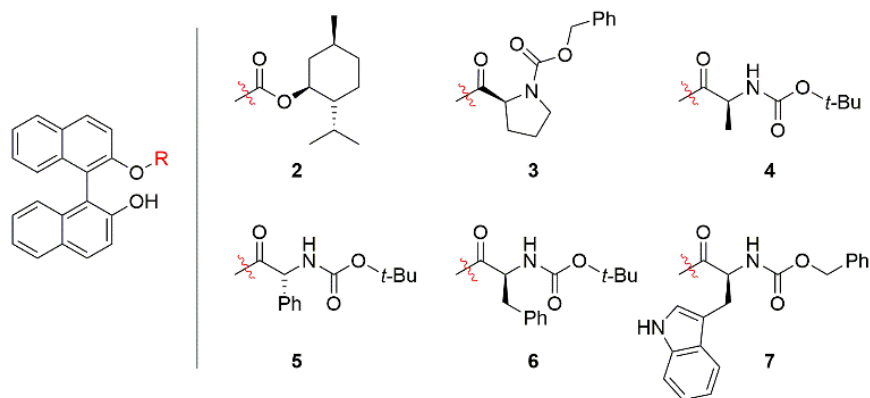
Figure 4.5 BINOL derivatives with chiral auxiliary groups

49

After 60 minutes of irradiation, this series of molecules exhibits a dramatic range of ee's from 63% to 4% for 5 and 2, respectively. For the amino acids, there is a general trend of

Table 4.4 Enantiomeric excess of BINOL with various chiral auxiliary groups before and after irradiation. [a]10 mM 1-7 with 0.1mL Et3N in toluene under 365 nm irradiation (8 mW/cm^2) at room temperature for 60 minutes with stirring. [b] ee was determined using SFC (Daicel CHIRALPAK® IA column, 35% CH_2Cl_2 in CO_2, 1.5 mL/min flow rate) [c] ee was determined using SFC (Daicel CHIRALPAK® IF column, 35% CH_2Cl_2 in CO_2, 1.5 mL/min flow rate).

entry	Group	ee (%) 0 min	ee (%) 60 min	Isolated Yield (%)
1	Boc-Pro	1[b]	31[b]	86
2	Menthyl	-5[b]	4[b]	56
3	Z-Pro	12[b]	25[b]	52
4	Boc-Ala	7[b]	20[b]	52
5	Boc-Phg	10[b]	63[b]	50
6	Boc-Phe	5[c]	47[c]	74
7	Z-Trp	3[c]	57[c]	82

increasing ee with increased steric bulk at the chiral center in the order of Ala (4) < Pro (1 and 3) < Phe (6) < Trp (7) < Phg (5). Perhaps not surprisingly, the terminal protecting group (Boc versus Z) has minimal influence on the ee as the proline derivatives 1 and 3 resulted in similar ee's of 31% and 25%, respectively. The menthyl carbonate derivative (2) gave the lowest ee of 4% likely due to the increased distance between BINOL and the chiral center of menthyl, limiting the chiral inductive influence.

Collectively, the above results are consistent with a Gibbs free energy diagram depicted in Figure 4.6. For BINOL with or without a chiral auxiliary group, the activation barrier for isomerization in the ground state is sufficiently high that it does not occur until over 100° C. However, upon excitation and in the presence of a base, ESPT facilitates isomerization between (R)- and (S)-BINOL. In the absence of a chiral auxiliary group (left of Figure 4.6) the isomerization is equally favorable in both directions and thus no enantioenrichment is observed. In contrast, the addition of a chiral auxiliary group makes the energy of the diastereomers unequal (right of Figure 4.6). The ΔG between the diastereomers dictates the concentration ratio at equilibrium (i.e. the photostationary state). The identity of the chiral auxiliary influences the magnitude of ΔG and the resulting ee.

It is important to note that the energies would be intrinsically higher for the excited state of the molecules but have been normalized in this diagram. Additionally, because the reaction occurs in the excited state, but not the ground state, it is reasonable to assume the activation barrier in the excited state is lower, but we have no direct information about intermediates or transition states and thus have depicted the reaction as a single step process.

As a preliminary attempt to model ee values, we used time-dependent density functional theory (B3LYP, 6-31g**) to calculate first excited state energy differences between (R) and (S) enantiomers for deprotonated Boc-Pro-BINOL. The energy difference was calculated as 0.2 kcal/mol which corresponds to a 17% ee. While the enantiomeric excess value was calculated using ΔE in vacuum, as opposed to ΔG in toluene, the results are qualitatively consistent with measured ee values, suggesting DFT may be a useful tool in predicting and designing alternative auxiliary groups. Efforts are underway to expand the theory to model both ground and excited states of protonated and deprotonated forms of BINOL derivatives, taking solvent into account.
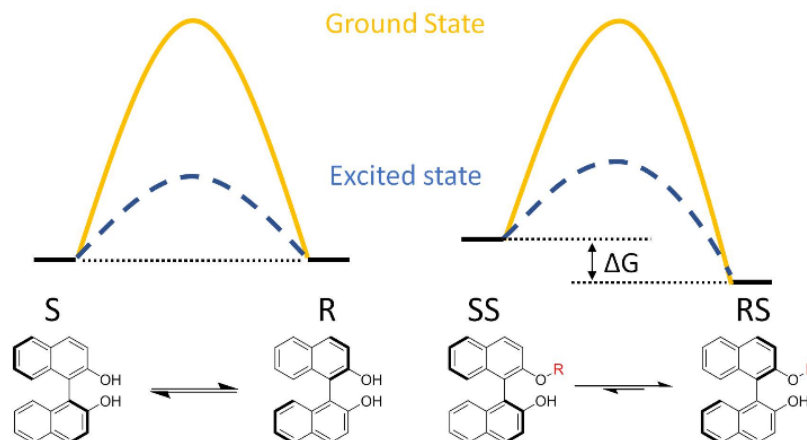
Figure 4.6 Normalized Gibbs free energy diagram for ground (orange) and excited state (blue) isomerization for BINOL without (left) and with a chiral auxiliary group (right).

In summary, we have demonstrated that photoexcitation followed by excited state proton transfer and isomerization is an effective means of enantioenriching BINOL. Regardless of the ee of the starting solution, the resulting ee is dictated by the ratio between the diastereomers upon reaching a photostationary state with values as high as 63% ee. The nature of the chiral auxiliary and the distance from the BINOL core influences the equilibrium condition with a general increase in ee with increased steric bulk. Presumably, increasing the steric bulk and attaching the chiral center directly to the alcohol group will increase the ee to near unity values.

This work opens the door to an entirely new strategy for enantioenriching BINOL and related atropisomeric compounds. While the resolution of the parent BINOL is largely a solved problem, expanding this methodology to more complex and asymmetric BINOL derivatives may provide a means of obtaining enantiopure compounds that are difficult to prepare by standard means. This technique may also help avoid the use of costly purification procedures and eliminate the waste associated with isolating only the desired product at <50% yield.

CHAPTER 5

SOLID STATE MULTICOLOR EMISSION IN SUBSTITUTIONAL SOLID SOLUTIONS OF METAL-ORGANIC FRAMEWORKS

5.1   Introduction to Multivariate Metal-Organic Frameworks

Preparing crystalline materials that produce tunable organic based multicolor emission is a challenge due to the inherent inability to control the packing of organic molecules in the solid state. Utilizing multivariate, high symmetry metal−organic frameworks, MOFs, as matrices for organic-based substitutional solid solutions allows for the incorporation of multiple fluorophores with different emission profiles into a single material. By combining nonfluorescent links with dilute mixtures of red, green, and blue fluorescent links, we prepared zirconia-type MOFs and found that the bulk materials exhibit features of solution-like fluorescence. Our study found that MOFs with a fluorophore link concentration of around 1 mol % exhibit fluorescence with decreased inner filtering, demonstrated by changes in spectral profiles, increased quantum yields,
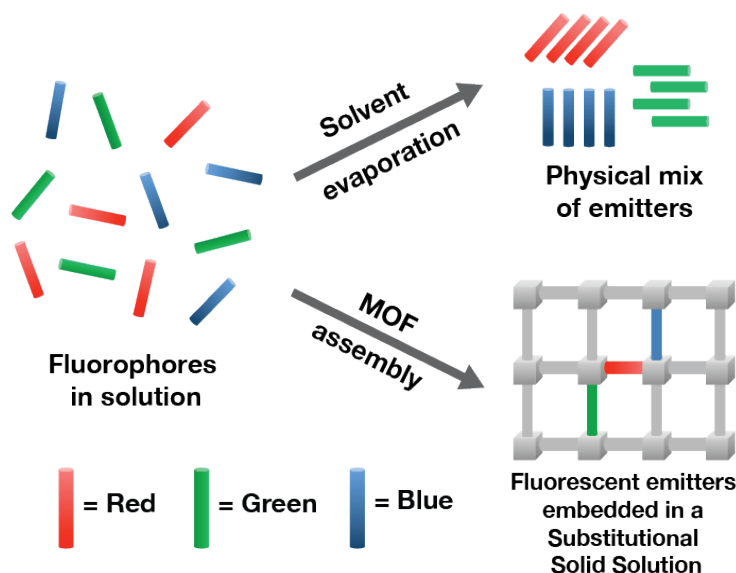
Figure 5.1 Graphic depicting generalized assembly of fluorophores under traditional solvent evaporation techniques (top right), and under metal organic framework crystallization techniques (bottom right).

and lifetime dynamics expected for excited-state proton-transfer emitters. Our findings enabled us to prepare organic-based substitutional solid solutions with tunable chromaticity regulated only by the initial amounts of fluorophores. These materials emit multicolor and white light with high quantum yields (~2−14%), high color-rendering indices (>93), long shelf life, and superb hydrolytic stability at ambient conditions.
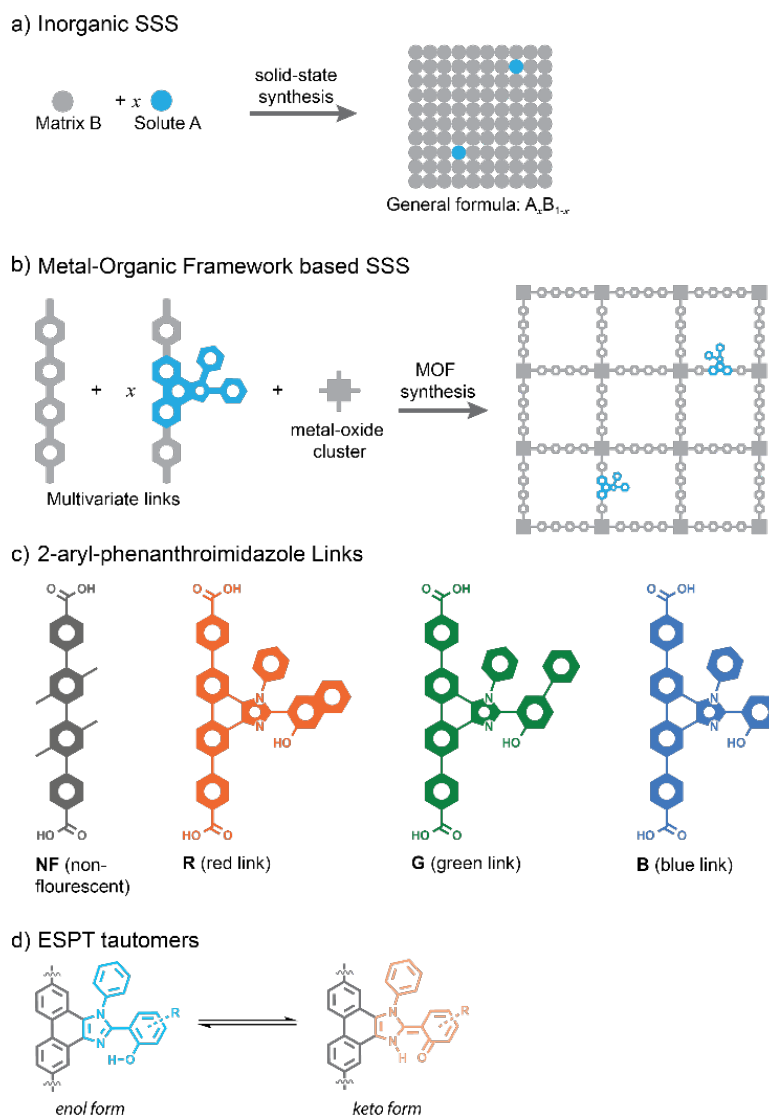
Figure 5.2 a) Scheme of organic-based substitutional solid solution formation in MOFs. b) Organic links used in this study. c) Excited state proton transfer tautomers.

Multicolor emission in solutions is a phenomenon that occurs in a system of multiple emitters, where the bulk fluorescence of a solution is the result of the combined emission of each

emitter.[118, 119] In liquid solutions of dilute organic fluorophores, this phenomenon is easily controlled because solutions with exact concentrations can be prepared. In the crystalline solid state (i.e., excluding polymer blends and glasses), organic based multicolor emission is more challenging to produce because when the solvent is removed mixtures of organic fluorophores aggregate,[120, 121] phase separate, and quench, producing heterogeneous solid mixtures with unpredictable fluorescence. A strategy to produce organic-based crystals with tunable bulk multicolor emission is by adapting the solid-state chemistry concept of substitutional solid solutions (SSS). SSS are crystals that form when a solute atom (Figure 5.2a) is incorporated into a uniform crystalline matrix, substituting some of the matrix atoms, so the solute is effectively dissolved within the average unit cell.[122] Application of this concept in inorganic materials has allowed for fine-tuned control of physical properties of materials for applications such as lasers[123] and blue LEDs.[124] In the case of organic materials, however, the concept of preparing SSS does not generally apply for several reasons. First, unlike atoms, organic molecules are nonspherical, so matrix-dopant matching is a nontrivial task.[125, 126] Second, organic compounds tend to form low symmetry and unpredictable crystal packings,[127] which makes their bulk crystallographic characterization a challenge. Third, as mentioned above, mixtures of organic
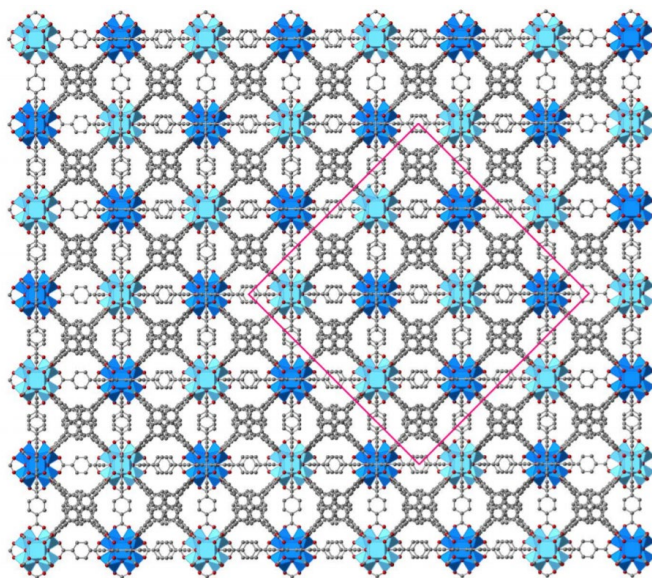
Figure 5.3 Crystal model of NF MOF viewed along the 001 direction. Unit cell is indicated, black spheres are carbon, red spheres are oxygen, blue polyhedra represent zirconium, and the light and dark blue polyhedra represent zirconium clusters in each of the two interwoven frameworks, respectively. Methyl carbon and hydrogen are not shown for clarity.

compounds phase separate during crystallization, so homogeneous incorporation of solutes is not ensured. Despite these challenges, preparation of organic-based SSS with tunable fluorescence would allow for preparing crystalline materials that take advantage of the inherent tunability of molecular emitters.

Multivariate metal−organic frameworks (MTV MOFs) are a subclass of MOFs where organic links of varied functionalization are incorporated into a single phase MOF.[128] These types of MOFs are an attractive platform for making multicolor emitting crystals because the crystalline arrangement of the organic links is dictated by the structure of the MOF. When considering high-symmetry MOFs, the organic links will also arrange in a high-symmetry environment despite their differences in chemical functionality (Figure 5.2b).[129] Here, we demonstrate that utilizing high-symmetry multivariate MOFs as matrices for organic-based SSS enables the preparation of crystalline multicolor emitting materials. By forcing the organic links to arrange in high-symmetry environments, a higher level of synthetic control can be achieved because these MTV MOFs circumvent the problems associated with organic-based SSS (see above). In addition, using high-symmetry MOFs (e.g., cubic) facilitates crystallographic characterization via crystal simulations and powder diffractometry. We demonstrate that incorporation of links that contain red, green, and blue (RGB) fluorescent moieties (Figure 5.2b) into a nonfluorescent, high symmetry MOF results in the formation of fluorescent, organic-based SSS. The observed organic SSS behavior allows tunable multicolor emission in bulk crystals with emissive properties dictated exclusively by the input concentration of RGB fluorophore links, producing materials that fluoresce with many different colors, including white light, with easy-to-tune color parameters (e.g., chromaticity and white-light temperature), and very high color-rendering indices. The prepared materials retain their crystallinity at room temperature for months under normal laboratory conditions and even after direct exposure to water. We found that dilution of fluorescent links at around 1.0 mol % displayed typical solution behavior, including decreased inner filtering, high quantum yields, tunable chromaticities, excitation−emission independence, concentration-dependent energy transfer, as well as emission phenomena expected from the fluorophores, such as excited state proton transfer (ESPT).

5.2 Experimental for Single Component Systems

The MOF matrix utilized here consists of the zirconia-type PPPP−PIZOF MOF (Figure 5.3), an interwoven face-centered cubic network (space group Fd$\bar{3}$m)[130] built with tetramethyl quarterphenyldicarboxylate (Figure 5.2c) that is nonfluorescent in the visible region. This MOF type is water stable and allows for the incorporation of links of varied nature.[129] Based on ESPT dyes designed by Park et al., the multivariate links are composed of quarterphenyl chains bearing 1,2- diarylphenanthro[9,10-d]imidazole fluorophores.[131, 132] This moiety was utilized as a template for its stability to MOF synthetic conditions, high quantum yield, and ease of color
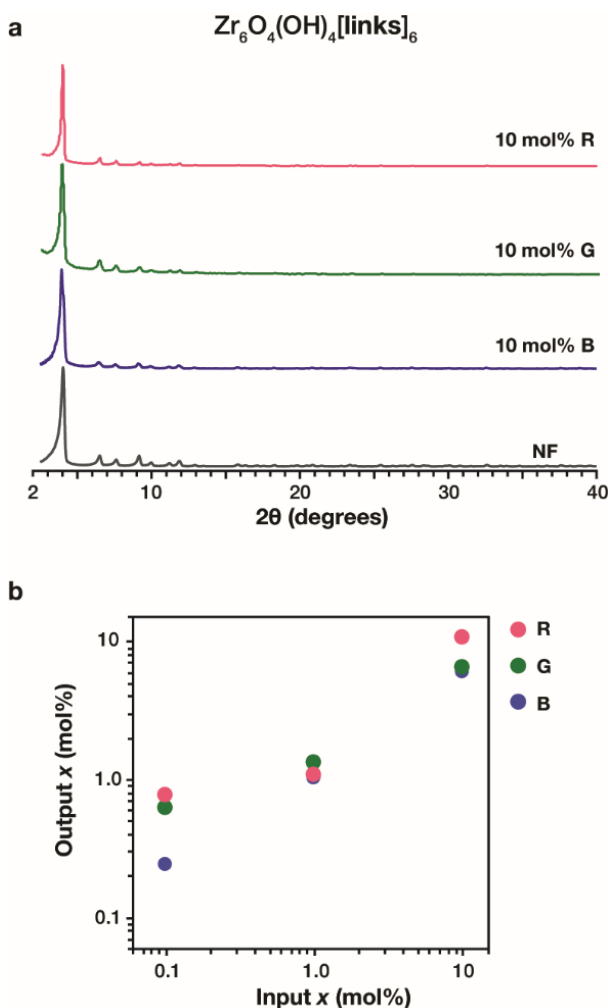
Figure 5.4 (a) Powder X-ray diffraction (PXRD) patterns of **NF** and **RGB**-containing MOFs, indicating their isoreticular nature. (b) Substitutional input-output plot for 3 sets of single fluorophore MOFs with *x* in mol%.
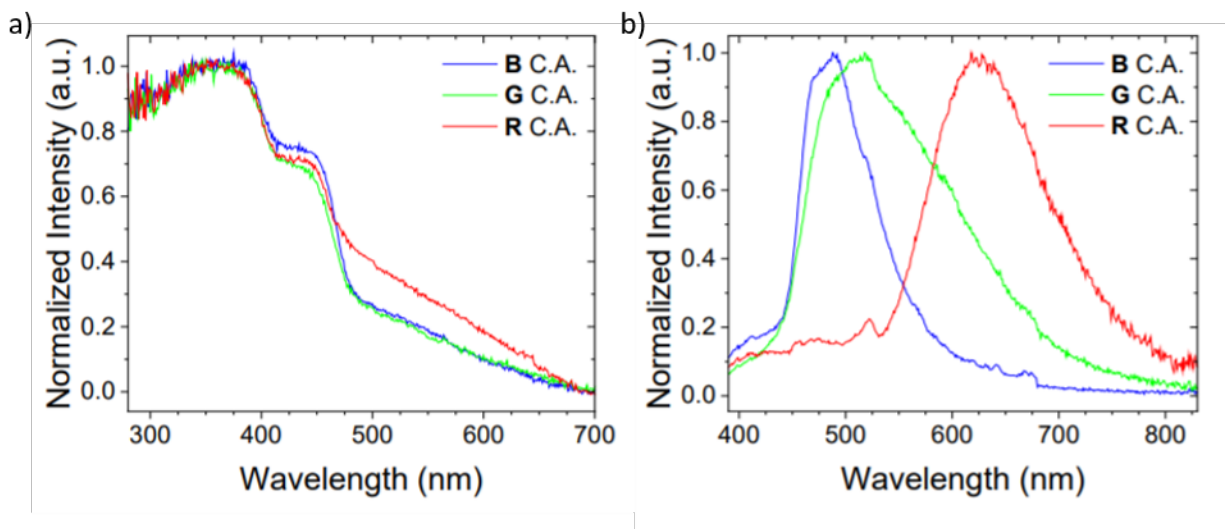
Figure 5.5 a) Absolute absorbance spectrum and b) emission spectra for neat solids of blue, red, and green acids (25 °C).

variability through synthesis. When the aryl at the 2 position is an o-phenol derivative, the dye can exist as an enol or keto tautomer (Figure 5.2d) by transferring the phenolic proton to the unsubstituted nitrogen of the imidazole ring.[133] In the ground state, these dyes exist in the enol tautomer. After excitation, a proton transfer can occur, producing the excited state keto form that induces a large apparent Stokes shift that varies according to the molecular structure of the phenol. As such, an unsubstituted phenol has a small shift, emitting in the blue, adding a phenyl group shifts emission to green, and changing to a naphthol group further shifts emission to red (Figure 5.5). After relaxing via emission, the dye readily reverts to the enol form. This large apparent Stokes shift is advantageous for mixed fluorophore systems because it allows for single wavelength excitation of the high energy enol form and emission from the low energy keto form with minimal spectral overlap.[14, 133] Furthermore, covalent attachment of diaryl phenanthroimidazole to the quaterphenyl links ensures that fluorophores will not diffuse or leach out of the solid.[134, 135] The SSS were prepared using the multivariate links shown in Figure 5.2b, herein referred to as NF (nonfluorescent), R (red), G (green), and B (blue).

Crystalline single fluorophore MOFs of NF with R, G, or B produced solids samples with formulas $Zr_6O_4(OH)_4[R_xNF_{1-x}]_6$, $Zr_6O_4(OH)_4[G_xNF_{1-x}]_6$, and $Zr_6O_4(OH)_4[B_xNF_{1-x}]_6$ with substitutional input x values between 0.10 and 10 mol %. For simplicity, samples with a single fluorophore will be referred to as x%-fluorophore, i.e., 10%-B, 10%-G, and 10%-R for MOFs

58

Table 5.1 Photophysical properties of ester links in toluene (25 °C) (a) Emission data acquired using dilute solutions (~1 × 10^{-5} M). (b) $k_r = \Phi/\tau$. (c) $k_{nr} = (1-\Phi)/\tau$.

Compound	Absorbance λ (nm)	Emission at rt[a]			k_r (× 10^{7}s^{-1})[b]	k_{nr} (× 10^{8}s^{-1})[c]
		λ_{max} (nm)	τ (ns)	Φ_{PL}		
Blue	330	420	7.8	0.35	4.5	0.83
Green	305	505	5.6	0.22	4.0	1.4
Red	335	605	7.9	0.04	0.5	1.2

with a 10% fluorophore input. All samples were prepared utilizing solvothermal MOF crystallization conditions[130] and exhibited the same powder X-ray diffraction (PXRD) pattern of the pure NF MOF (Figure 5.4). Predictable and adjustable linker incorporation was demonstrated from the synthetic input/structural output plot shown in Figure 5.4 with output composition values determined by solution ^{1}H NMR of digested MOF samples. Attempts to prepare MOFs with higher fluorophore content (>10 mol %) were unsuccessful, producing amorphous, nonporous solids with inconsistent fluorophore content. This observation indicates that the MOF matrix has a limited tolerance for sterically crowded links. Furthermore, it also suggests that it is unlikely that a mix-phase MOF composite is formed (e.g., clustered RGB MOF crystals mixed with pure NF MOF crystals). Regarding the homogeneity of the fluorescent links in the SSS, previous work on high-symmetry MTV MOFs has shown that the distribution of the MTV links
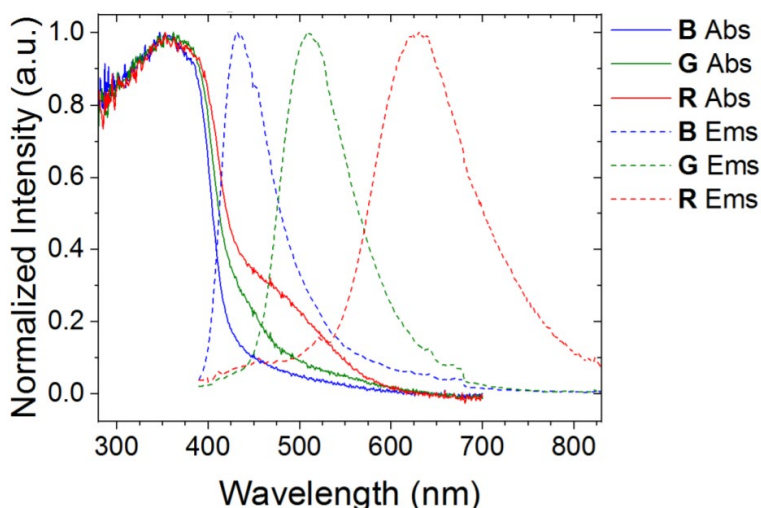
Figure 5.6 UV-Vis absorption (solid lines) and emission (dashed lines, λ_{ex} = 360 nm) spectra of 10%-B, 10%-G, and 10%-R (25 °C).

is highly dependent on the dilution range of the dopant link. In our case, high fluorophore dilution likely results in MOF with homogeneous distribution,[129] with the 10 mol % MOFs potentially forming alternating apportionments.[136] Further studies using multidimensional solid-state NMR on isotopically enriched MOFs will provide this information. Nonetheless, consistent and reproducible fluorescence was observed in the bulk, indicating little effect from the links distribution.
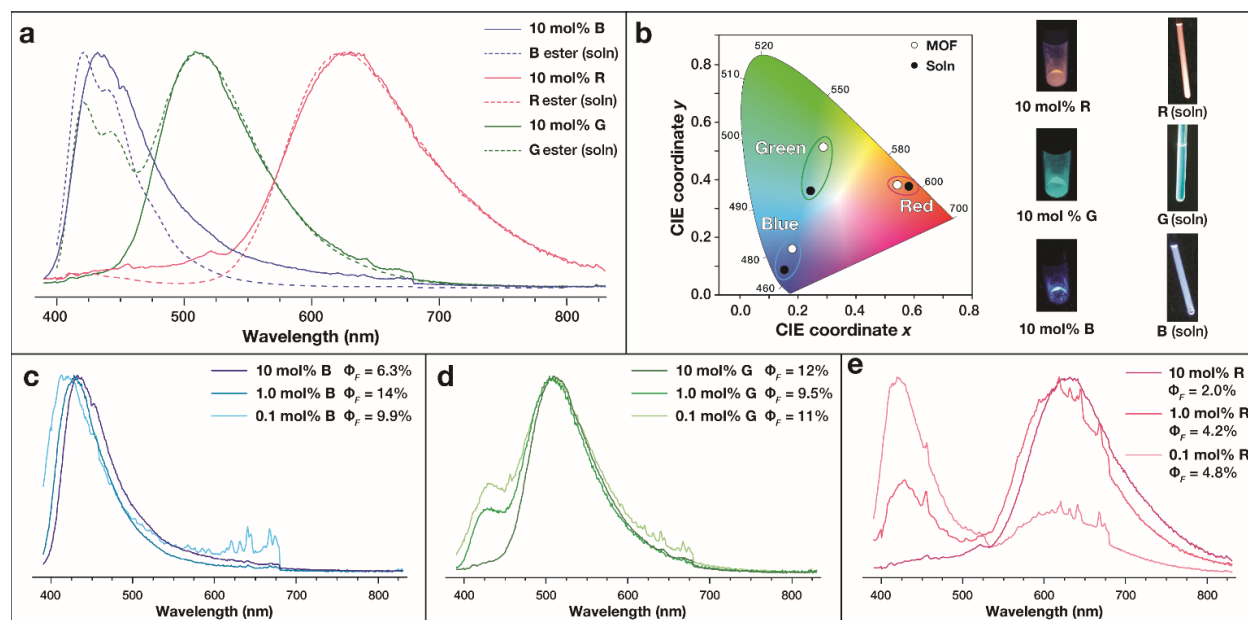
Figure 5.7 (a) Overlay of toluene-solvated fluorophore esters (dashed lines) and $x = 10$ mol% input single fluorophore MOFs (solid lines). (b) CIE chromaticity coordinates of prepared $x = 10$ mol% MOFs (open circles) and solvated links (closed circles), and optical image of MOF powders and solvated links under UV light. (c-e) Emission profiles of **B**, **G**, and **R** MOFs, respectively at varied dilution ($0.1 \leq x \leq 10$ mol%) indicating their quantum yields ($\lambda_{ex} = 365$ nm).

Despite having similar absorption profiles (Figure 5.5), upon excitation at 365 nm, MOFs made with 10%-R, 10%-G, and 10%-B exhibit solid-state emission maxima at 430, 510, and 630 nm (Figure 5.6), respectively, with relatively high color purity (Figure 5.7b). The emission profiles of these MOFs are drastically different than the neat solid linkers (Figure 5.5b). In contrast, the low energy keto emission in the MOFs closely resembles that of the ester forms of the RGB links solvated in toluene (Figure 5.7a, dashed lines), suggesting that the pore microenvironment of the MOF more closely resembles the toluene-solvated, rather than neat solids of the linker.

60

The fluorophore mimics liquid-phase solution behavior in that the RGB links show concentration dependent changes in the emission profiles for all three fluorophore MOFs (Figure 5.7c−e). These changes are most notable in R and G containing MOFs, where there is a gradual increase in the high energy enol emission with decreasing concentration and a shift in the CIE (Commission Internationale de l'Eclairage) chromaticity coordinates from the red and green regions toward the blue portion of the diagram (Figure 5.8). For B and R, the spectral changes are accompanied by an emission lifetime and quantum yield increase from x = 10 to 1.0 mol % (Figure 5.7c,e, Table 5.2). These observations are consistent with an energy-transfer event[137] where spectral overlap between enol emission and enol absorption inhibits the higher energy light from exiting the solid. A similar effect can be observed in concentrated solutions but is presumably greatly enhanced by the high local concentration of the fluorophores in the MOF.[138] Monitoring the excited-state dynamics in the MOF using subnanosecond transient absorption measurements will be necessary to definitively establish an energy transfer mechanism. Regardless, the similarity in lifetime and quantum yield between 1.0%-B and 0.1%-B as well as
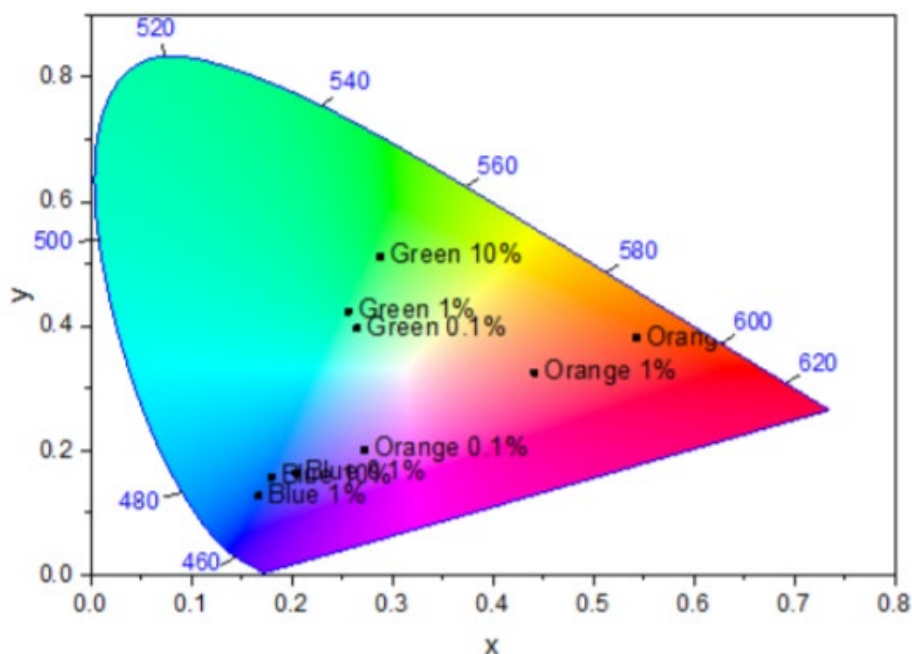
Figure 5.8 CIE dependence with varied input x for single fluorophore MOFs (λ_{ex} from 340-400 nm @ 10 nm step).

1.0%-R and 0.1%-R (Figure 5.7c,e) suggests that the inner filtering effect is minimal at concentrations of x = 1.0 mol %. These concentrations of fluorophore result in MOFs with

61

quantum yields which are up to an order of magnitude greater than previously prepared broadband emitting MOFs[139-141] and are similar to the soluble ester forms of the linkers in a toluene solution (Table 5.1).

Figure 5.9 Two component SSS MOFs: (Top) Optical images of samples under λ_{ex} = 365 nm indicating their fluorophore composition, (middle) emission profiles with λ_{ex} = 365 nm, and (bottom) CIE chromaticity coordinates of mixtures of **R** and **B** (left), and mixtures of **G** and **B** (right).

This dilution can be interpreted in terms of molar concentration of the links in the MOF since [links]max = 1.34 M (single crystal analysis of NF MOF evidence 48 links per unit cell with a cell volume of 58,400 Å^3 , equivalent to 1.34 mollinks dm^{-3}). As such, 10%-B, 1.0%-B, and 0.1%-B have molar concentrations of [B] = 134, 13.4, and 1.34 mM, respectively. These molarity values for 1.0%-B and 0.1%-B fall close to a dilution range with reduced inner filtering,
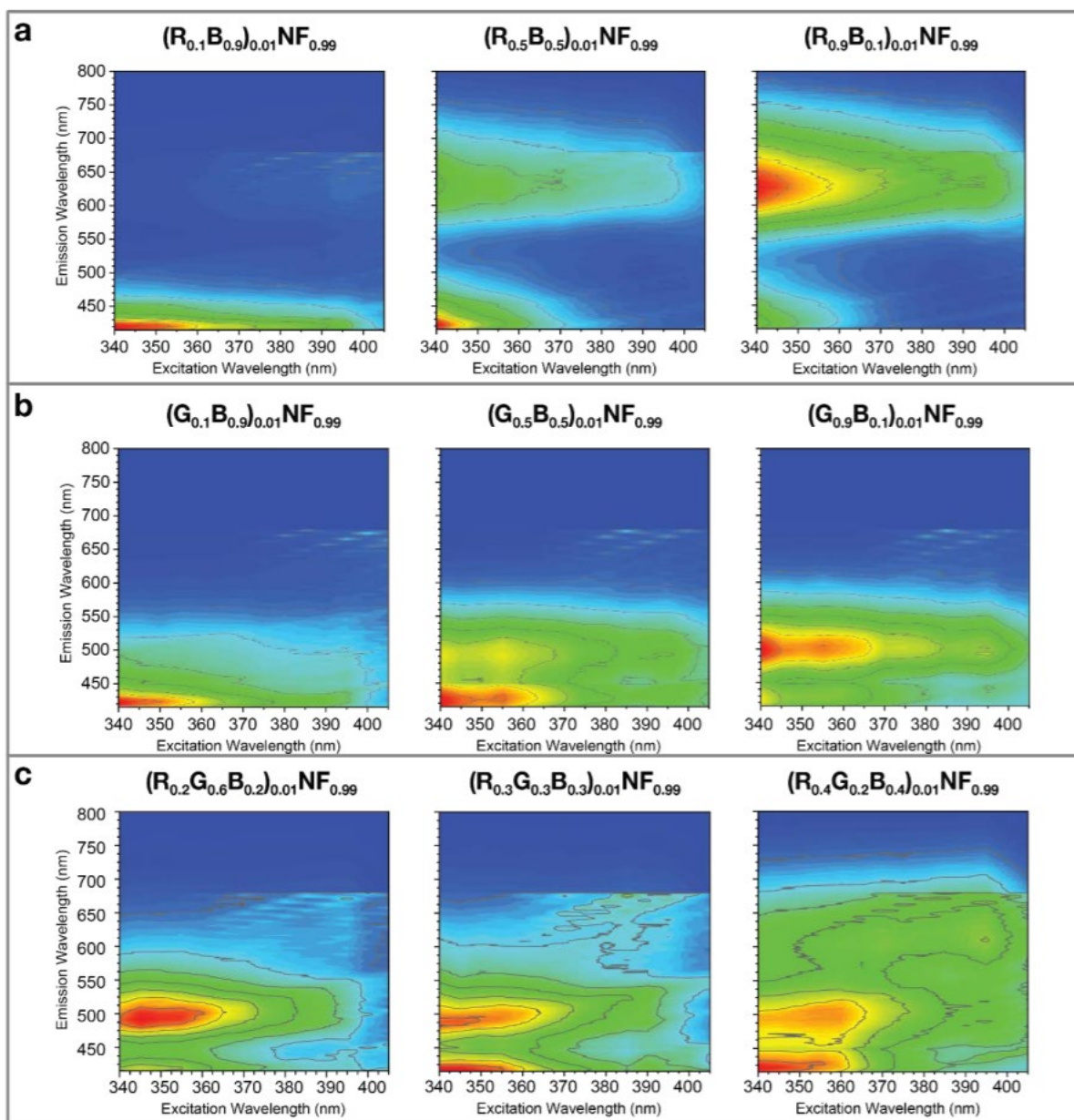
Figure 5.10 Excitation-emission maps of (a) R and B, (b) G and B, and (c) RGB MOFs demonstrating excitation independence.

and the 10%-B resembles a concentrated solution where the emission is dominated by this inner filtering.

5.3   Experimental for Multi Component Systems

Incorporation of two and three fluorophores resulted in MOFs that exhibit the combined emission of each fluorophore. For $Zr_6O_4(OH)_4(R_xB_{1-x})_yNF_{1-y}$ and $Zr_6O_4(OH)_4(G_xB_{1-x})_yNF_{1-y}$ with y = 0.01, under 365 nm excitation, we observed a sum of the individual components and a linear transition from R to B or G to B as x varies from 0.9 to 0.5 to 0.1 (Figure 5.9). The excitation−emission maps (Figure 5.10) as well as CIE coordinate diagrams with respect to λ_{ex} indicate that emission from the mixed fluorophore systems are excitation wavelength independent. The additive nature of the emission profiles and the wavelength independent CIE chromaticity coordinates are consistent with minimal energy transfer in the y = 0.01 MOFs.
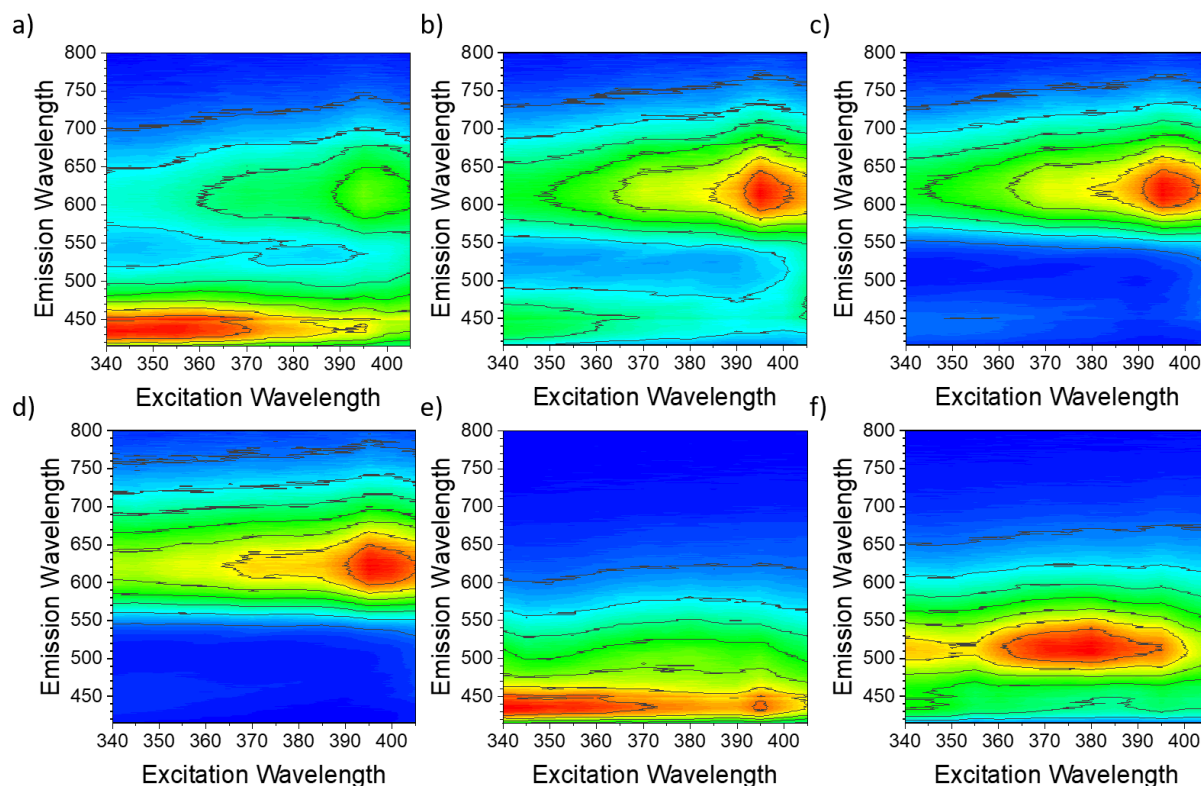
Figure 5.11 High doping (10%) excitation-emission maps of 9:1, 7.5:2.5, 5:5, and 2.5:7.5 B to R (a-d) and 9:1, and 5:5 B to G (e-f)

Consequently, selective color generation along these axes could be achieved by tuning the fluorophore ratio.

The three-fluorophore system with a composition of $Zr_6O_4(OH)_4(R_xG_{1-2x}B_x)_yNF_{1-y}$ exhibited emission profiles that depend on the total fluorophore concentration y. As expected for y = 0.10, the emission is strongly dependent on the excitation wavelength (Figure 5.11) and generally dominated by yellow emission (R + G) with minimal high energy contribution (B) due to strong inner filter effects. For the $Zr_6O_4(OH)_4[(R_{0.33}G_{0.33}B_{0.33})_{0.10}NF_{0.90}]_6$ MOF (Table 5.2), excited-state lifetimes for B ($\tau_{460\,nm}$ = 1.5 ns), G ($\tau_{560\,nm}$ = 1.8 ns), and R ($\tau_{660\,nm}$ = 1.9 ns) were similar to that of 10%-R ($\tau_{660\,nm}$ = 1.5 ns) but notably shorter than for 10%-G ($\tau_{560\,nm}$ = 3.1 ns) and 10%-B ($\tau_{460\,nm}$ = 5.7 ns). The similarity in lifetimes of the three peaks is symptomatic of an energy-transfer equilibrium condition where the collective emission decay kinetics are dictated

Table 5.2 Lifetime and quantum yield comparison data of SSS MOFs.

Compound[a]	Φ_{PL}	Emission at rt					
		λ_{max} (nm)	τ (ns)	λ_{max} (nm)	τ (ns)	λ_{max} (nm)	τ (ns)
$B_{0.10}NF_{0.90}$	0.063	460	5.66	–	–	–	–
$G_{0.10}NF_{0.90}$	0.123	–	–	560	3.08	–	–
$R_{0.10}NF_{0.90}$	0.017	–	–	–	–	660	1.53
$B_{0.09}R_{0.01}NF_{0.90}$	0.047	–	–	–	–	–	–
$B_{0.075}R_{0.025}NF_{0.90}$	0.021	–	–	–	–	–	–
$B_{0.05}R_{0.05}NF_{0.90}$	0.035	–	–	–	–	–	–
$B_{0.025}R_{0.075}NF_{0.90}$	0.043	–	–	–	–	–	–
$B_{0.01}NF_{0.99}$	0.143	460	9.11	–	–	–	–
$G_{0.01}NF_{0.99}$	0.095	–	–	560	3.41	–	–
$R_{0.01}NF_{0.99}$	0.042	–	–	–	–	660	2.06
$B_{0.001}NF_{0.999}$	0.099	460	7.78	–	–	–	–
$G_{0.001}NF_{0.999}$	0.106	–	–	560	3.68	–	–
$R_{0.001}NF_{0.999}$	0.048	–	–	–	–	660	1.94
$B_{0.005}G_{0.005}NF_{0.99}$	–	460	4.54	560	4.43	–	–
$B_{0.001}G_{0.009}NF_{0.99}$	–	460	3.43	560	2.58	–	–
$B_{0.005}R_{0.005}NF_{0.99}$	–	460	4.74	–	–	660	1.28
$B_{0.002}G_{0.006}R_{0.002}NF_{0.99}$	5.0	460	3.33	560	2.07	660	1.48
$B_{0.003}G_{0.003}R_{0.003}NF_{0.99}$	5.2	460	3.96	560	2.63	660	1.58
$B_{0.004}G_{0.002}R_{0.004}NF_{0.99}$	4.3	460	5.71	560	3.30	660	1.71
$B_{0.04}G_{0.02}R_{0.04}NF_{0.90}$	–	460	2.50	560	2.85	660	2.29

[a] = for clarity, only the linker composition is listed

by the emitter with the fastest radiative decay rate (i.e., R).[142] That is, B energy transfer to R and G, G enol energy transfer to R and B, and R enol energy transfer to G and B, with all these processes occurring in parallel. In contrast, an overall fluorescent link dilution to 1.0 mol %, $Zr_6O_4(OH)_4(R_{0.33}G_{0.33}B_{0.33})_{0.01}NF_{0.99}$, resulted in lifetimes of 3.9, 2.6, and 1.6 ns for B, G, and R, respectively, more closely resembling the single component systems with no energy transfer.

The excitation−emission maps (Figure 5.10) show a decrease in excitation wavelength dependence, as seen in other dilute samples. At these lower concentrations, an increase in the enol emission is observed, most strongly for R, which results in deviations from the linear trend in the CIE chromaticity coordinates (points L and M, Figure 5.12). Once the concentration of R is sufficiently increased ($Zr_6O_4(OH)_4(R_{0.4}G_{0.2}B_{0.4})_{0.01}NF_{0.99}$) the low energy keto emission becomes predominant (Figure 5.12, point N). This sample exhibits the combined broadband K. This emission from RGB, with CIE chromaticity coordinates close to the center of the white light region (0.31, 0.33), a quantum yield of 4.3%, and a correlating blackbody temperature of 6480 temperature is nearly identical to that of natural daylight (6500 K)[143] and can be adjusted based
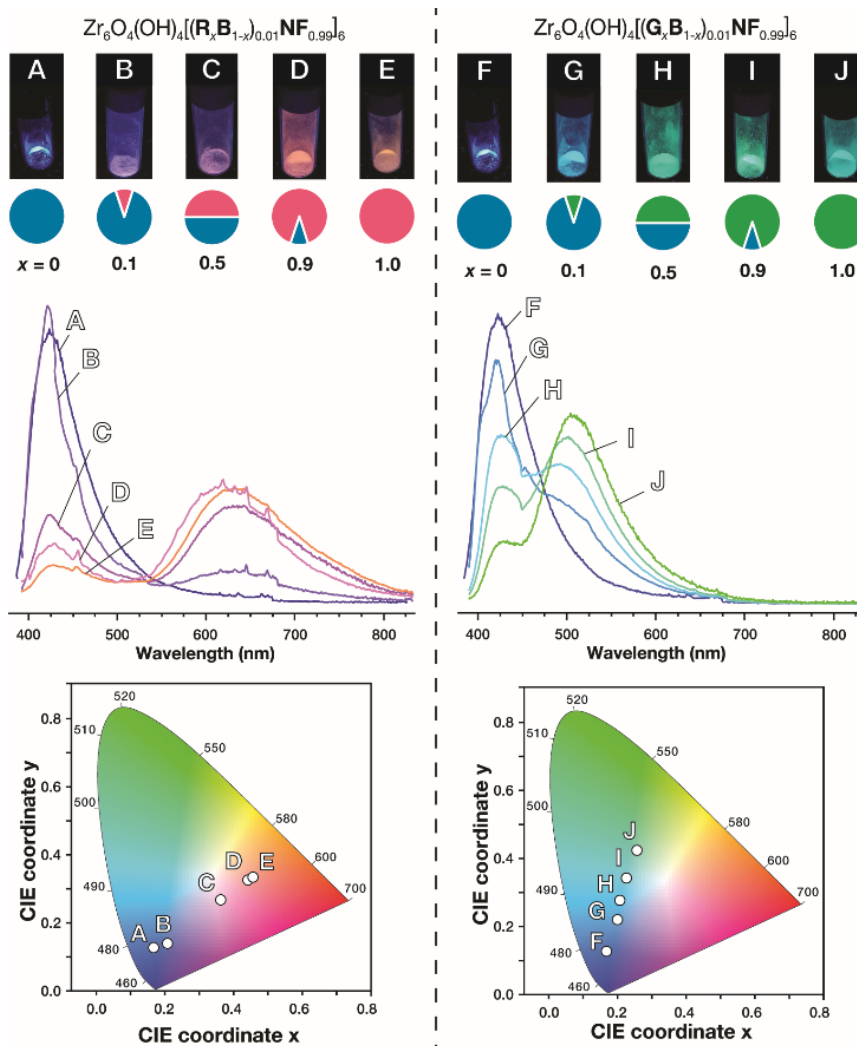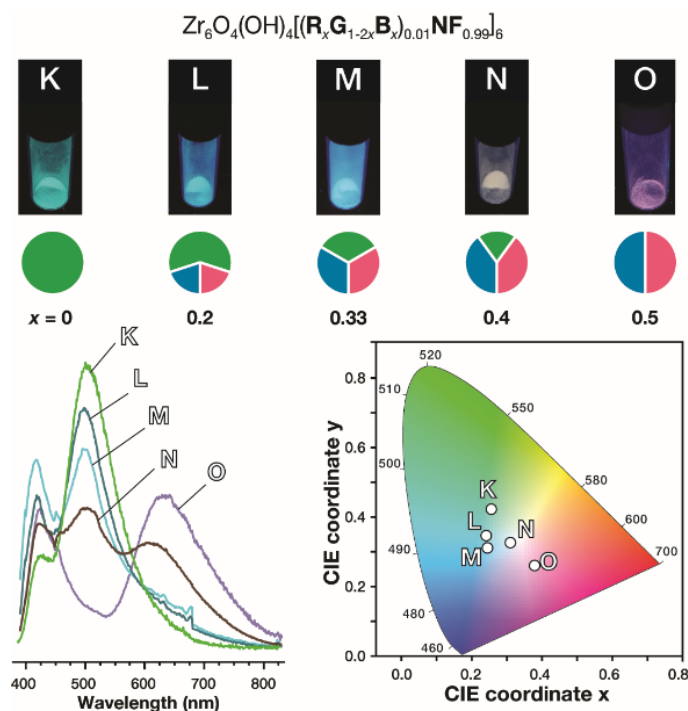

Figure 5.12 Three component SSS MOFs: (Top) Optical images of samples under λ_{ex} = 365 nm indicating their fluorophore composition, (bottom left) emission profiles with λ_{ex} = 365 nm, and (bottom right) CIE chromaticity coordinates of each sample.
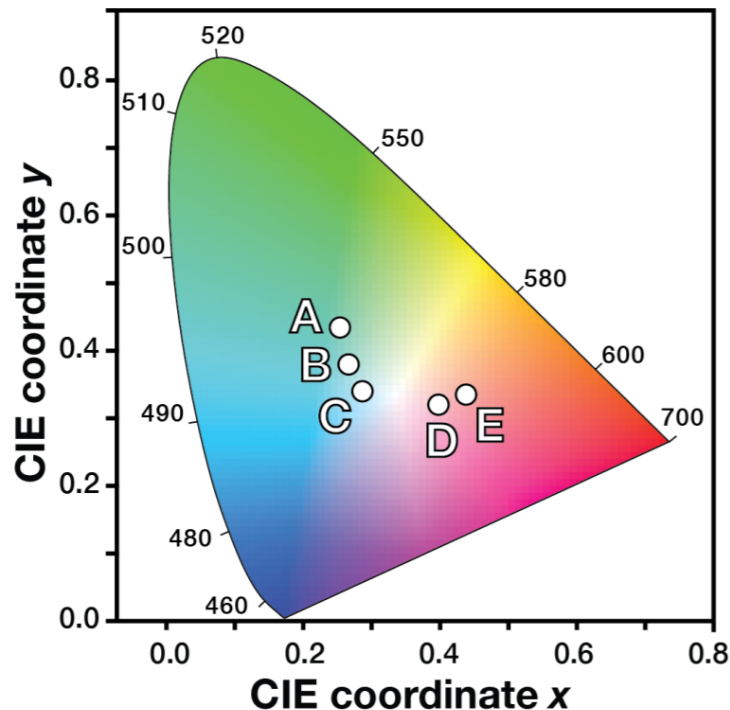
Figure 5.13 CIE coordinates of a) 1%-G MOF b) $Zr_6O_4(OH)_4[(R_{0.1}G_{0.9})_{0.01}NF_{0.99}]_6$ MOF, c) $Zr_6O_4(OH)_4[(R_{0.5}G_{0.5})_{0.01}NF_{0.99}]_6$ MOF, d) $Zr_6O_4(OH)_4[(R_{0.9}G_{0.1})_{0.01}NF_{0.99}]_6$ MOF and e) 1%-R MOF Ex = 365 nm (25 °C)

on the fluorophore concentration or the ratio of the fluorescent links. By increasing the overall concentration of the fluorophores to 10% a warmer white light can be achieved in $Zr_6O_4(OH)_4[(R_{0.4}G_{0.2}B_{0.4})_{0.10}NF_{0.90}]_6$ which has CIE chromaticity coordinates of (0.43, 0.39) and a corresponding temperature of 3060 K. Additionally, utilizing a two component system, taking advantage of the low concentration enol emission from R, cool white light can be achieved in $Zr_6O_4(OH)_4[(R_{0.5}G_{0.5})_{0.01}NF_{0.99}]_6$ with CIE chromaticity coordinates of (0.29, 0.33) and a corresponding temperature of 7820 K (Figure 5.13). To our knowledge, this is the first example of crystalline bulk materials whose fluorescent properties were adjusted following the dilution strategies used in liquid-phase fluorescence.

As a compliment to the CIE coordinates, the color-rendering index (CRI) is a critical parameter in describing how faithfully a light source represents the true color of an object with a score of 100 being a source identical to standardized daylight.[144] The CRI values for the above white light MOFs were calculated. and the results are reported in Table 5.3. Remarkably, sample N with formula $Zr_6O_4(OH)_4(R_{0.4}G_{0.2}B_{0.4})_{0.01}NF_{0.99}$ demonstrated a CRI of 93, and the two-

component R/G system with formula $Zr_6O_4(OH)_4(R_{0.5}G_{0.5})_{0.01}NF_{0.99}$ had a CRI of 95. For context, typical fluorescent bulbs are around 50 and white LEDs often score >80.[145] These results indicate that the mixed emitter MOFs are capable of both tunable emission chromaticity, as well as accurate color rendition.

All the MOFs synthesized are porous, stable to water, humidity, and up to 400 °C, and completely composed of earth-abundant elements. For example, 10%-B and $Zr_6O_4(OH)_4[(R_{0.33}G_{0.33}B_{0.33})_{0.01}NF_{0.99}]_6$ have Brunauer− Emmett−Teller (BET) surface areas of SBET = 1620 and 1600 m^2 g^{-1} respectively. The water stability in 10%-B was demonstrated by following changes in the diffraction pattern and BET surface area before and after exposure to water. Furthermore, the long-shelf life of the materials was demonstrated by the lack of changes in their PXRD even after 10 months of storage under laboratory conditions.

Table 5.3 Color rendering index (CRI) values of white light producing of SSS MOFs. For clarity, only the linker composition is listed.

Compound	CIE CRI
$B_{0.005}R_{0.005}NF_{0.99}$	69
$B_{0.001}R_{0.009}NF_{0.99}$	80
$G_{0.009}R_{0.001}NF_{0.99}$	72
$G_{0.005}R_{0.005}NF_{0.99}$	95
$G_{0.001}R_{0.009}NF_{0.99}$	82
$B_{0.001}G_{0.009}NF_{0.99}$	59
$B_{0.002}G_{0.006}R_{0.002}NF_{0.99}$	69
$B_{0.003}G_{0.003}R_{0.003}NF_{0.99}$	82
$B_{0.004}G_{0.002}R_{0.004}NF_{0.99}$	93

Other methods utilizing metal−organic materials for preparation of solid-state emission often bring significant drawbacks. For instance, Cu_4I_4 is a cluster used to create emissive materials, which has become a growing field in recent years. These materials offer similar quantum yields for pure colors, ca. 9%,[146, 147] but crystallize in low symmetry, unpredictable space groups. The Cu_4I_4 cluster is less ridged compared to the zirconium cluster, which results in cluster deformation when different ligands are bound creating low symmetry complex crystal

systems.[148, 149] Other emissive materials include MOFs where all the organic links in the framework are emissive fluorophores.[147] This results in unpredictable and inefficient fluorescence due to high inner filtering effects present in the material. Impregnating MOFs with fluorescent guest dyes can produce multicolor emission;[135] however, guest diffusion raises questions of homogeneity and long-term stability of the materials. Other MOF-based emissive materials utilize expensive rare-earth elements to achieve green and red fluorescence, with quantum yields ranging from 2 to 50%,[150-152] yet rare-earth elements are unsustainable, limiting their use as applied materials in the long term.[153] As such, the MOFs and methodology presented herein offer: an ease of characterization due to the high symmetry crystal system, tunable fluorophore concentration to achieve higher quantum yields with less inner filtering, and using earth abundant elements.

Applying the concept of SSS to organic-based materials was accomplished using high symmetry MOFs as matrices. This approach allows for circumvention of common challenges associated with emissive MOFs, including high inner filtering effects that cause complex emission, due to high fluorophore concentration, and high synthetic costs due to inclusion of lanthanides. This approach will further enable the ability to study other similar organic-based molecular phenomena in solids and can provide organic-based SSS materials for high precision applications such as in photonic devices and high definition displays.

CHAPTER 6

1,3-BIS(2-PYRIDYLIMINO)ISOINDOLINE DERIVATIVES AS VERSATILE FLUORESCENT ESIPT PROBES

6.1   Introduction to ESIPT Metal Sensor BPI

Colorimetric and fluorometric metal ion sensors are useful for a range of applications from biological labelling[154] to detecting heavy metal contamination in the environement.[155, 156] In the presence of the targeted analyte, these sensors typically exhibit a turn on/off emission and/or a discernible spectral shift in absorption/emission. Given these requirements, excited state proton transfer (ESIPT) dyes are a particularly appealing class of molecular sensors because they are highly sensitive to environmental changes (e.g. solvent, pH, etc) and exhibit large apparent Stokes shifts.[13, 157, 158] ESIPT compounds for sensing metal ions typically employ either 1) a 'fluorophore spacer receptor' architecture where the metal ion chelator and the chromo-fluorophoric unit are linked in proximity but largely independent moieties[159-161] or 2) the ESIPT functional groups can directly serve as the metal ion binding site where the proton is replaced by a metal ion.[12] Alternatively, one can envision an ESIPT dye where the metal ion chelator is intrinsic to the chromophore, but not the ESIPT site, which may provide a means of retaining ESIPT emission but with increased sensitivity and amplified spectral response to the analyte.

In 2011, Hanson et al. reported 1,3-bis(2-pyridylimino)-4,7-dihydroxyisoindole (**2** in Figure 1) as a new class of ESIPT dye.[162] Photoexcitation of this molecule leads to an electron density shift away from the phenolic protons (OH) and toward the imine (N) followed by excited state proton transfer from O to N, and finally emission from the proton transferred, keto state.[163] [164] Compound **2** exhibits a large apparent stokes shift ($>6{,}000\ \text{cm}^{-1}$) and ESIPT emission quantum yields of $>40\%$. The latter is particularly notable in that it is one of the highest ESIPT quantum yields reported to date.[13] Equally important, at least for the present study, is that compound **2** contains a 1,3-bis(2-pyridylimino)isoindole core which is a tridendate, monoanionic ligand known for binding a large range of metal ions like Fe^{2+}, Pt^{2+}, Co^{2+}, Ni^{2+}, Cu^{2+}, Zn^{2+}, Cd^{2+}, and more.[165-169] Therefore, unlike typical ESIPT metal ion sensors,[170, 171] the metal ion binding site in **2** is conjugated to the photoactive portion of the dye and may be directly involved in influencing the ESIPT event. Herein we report our study into the influence of metal(II) ions on

the photophysical properties of 1,3-bis(2-pyridylimino)-4,7-dihydroxyisoindole-based ESIPT dyes. Our experiments show that this ESIPT dye is responsive to several metal ions but it shows a dramatic response to Zn^{2+} ions resulting in a nearly two fold enhancement in emission quantum yield. Additionally, we demonstrate that with the use of phenolic protecting groups, this dye can also serve as turn on fluorescence probe for hydrazine.

6.2   Results and Discussion

The chromophores/fluorophores used in this study are shown in Figure 6.1. The parent, non-ESIPT dye **1** (a.k.a BPI), was synthesized using the alkaline-earth-catalyzed nucleophilic addition of pyridyl amine to 1,2-dicyanobenzene in butanol as originally reported by Siegl.[172] Compound **2** was synthesized using the same procedure but with minor modifications as described previously.[162] It is worth mentioning that the reaction time (20 days) and yield (24%)

1: R, R' = H
2: R, R' = OH
3: R = OH, R' = Boc
4: R = BrButyrate, R' = Boc
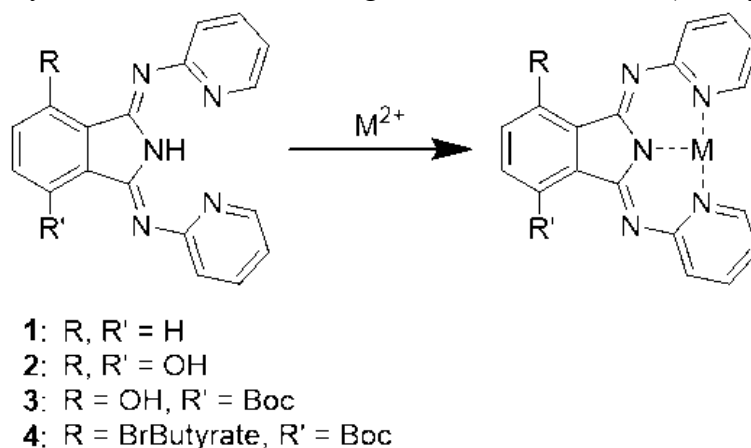
Figure 6.1 Structure of molecules **1-4** and the proposed coordination site of the M^{2+} ions.

for **2** were notably lower and longer than **1** (2 days and 68%) presumably due to deactivation of the cyano groups by the alcohol substituents.

Using ultrafast spectroscopy, Dawlaty and coworkers to demonstrate that one alcohol group of **2** is sufficient for ESIPT to occur.[173, 174] With this in mind, we prepared compounds **3** and **4** containing a single Boc (i.e. *tert*butoxycarbonyl) and both Boc and bromo butyrate phenolic protecting groups, respectively. These were selected as the alcohol protecting groups because 1) Boc increases the solubility of **2** and 2) bromo butyrate is known to undergo cleavage

in the presence of hydrazine enabling "turn on" sensing (*vida infra*).[175-177] Compound **3** was synthesized by reacting **2** with di-tert-butyl dicarbonate anhydride in acetonitrile to give **3** in 65% yield. Interestingly, even with a large excess of di-tert-butyl dicarbonate anhydride, Boc addition only occurred at one of the OH groups of making this a convenient strategy for asymmetric functionalization of **2**. Subsequent reaction of **3** with 4-bromobutyric acid in DCM in the presence of EDC and with DMAP catalyst gave compound **4** in 78% yield.

The photophysical properties of 1 and 2 in the absence and presence of metal(II) perchlorate salts was measured in a 90:10 mixture of DMSO/water (v/v). Due to the low solubility of 1 and 2 in aqueous conditions, DMSO was selected as the primary solvent for photophysical studies. However, with the intention of creating a practical methodology (i.e. sampling aqueous biological fluids), 10% volume of water or water containing the cations of interest were added to 1 or 2 in DMSO. It is important to note that there was negligible change in the photophysical properties of 2 in DMSO after the addition of water (Figure 6.2).
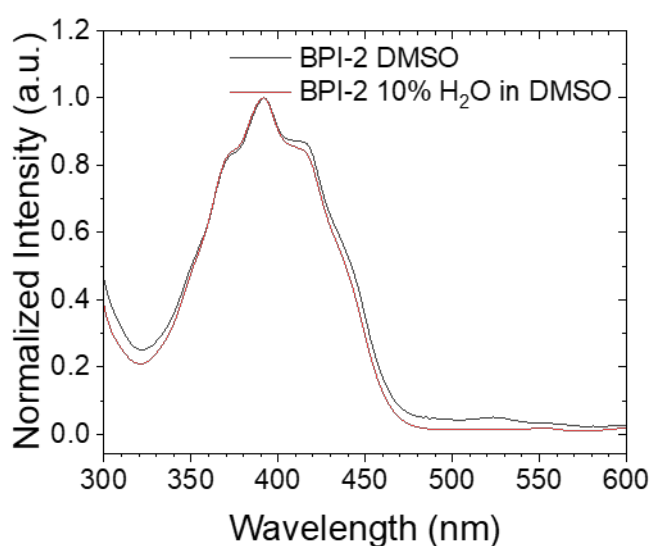
Figure 6.2 Absorption spectra of BPI-2 in DMSO and in a 10:1 (v:v) solution of DMSO and water demonstrating that there is negligible change in the colorimetric properties.

The parent molecule **1**, with no OH groups for proton transfer, exhibits highly structured absorption features at <420 nm and was non-emissive (Φ_{em} < 0.01%) at room temperature. In contrast, **2** has less well defined but still structured absorption (350-480 nm), bright orange

emission at 610 nm (Φ_{em} = 25%), and a large apparent Stokes shift (6,600 cm^{-1}) consistent with absorption in the enol state, ESIPT, and then emission from the keto state.

Select absorption and emission spectra of **1** and **2** following the addition of 100 equivalents of dication perchlorate salts are shown in Figure 6.3. The addition of Ba^{2+}, Ca^{2+}, Cd^{2+}, Fe^{2+}, Mg^{2+}, Mn^{2+}, and Sr^{2+} to **1** had minimal effect on the absorption spectra. The most observable change in this series was in the amplitude, but not position, of the high energy absorption peaks upon the addition of Fe^{2+} however this can be attributed to increased light
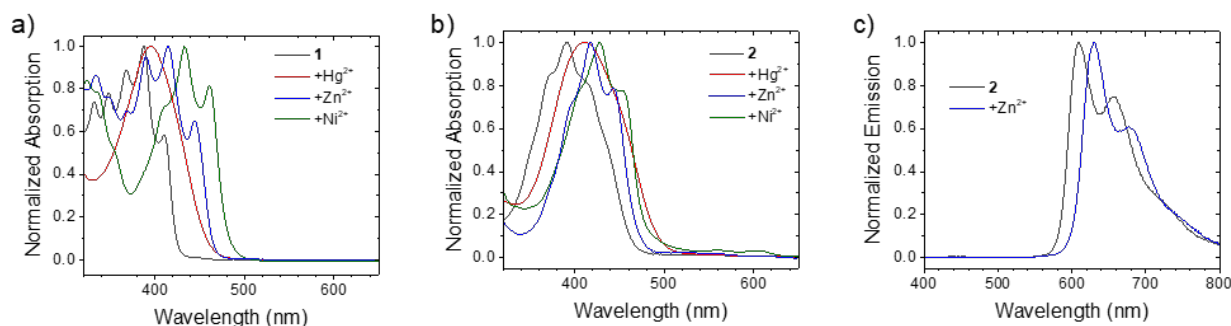
Figure 6.3 Normalized absorption spectra of **1** (a) and **2** (b) without and with 100 equivalents of Hg^{2+}, Zn^{2+}, and Ni^{2+}. (c) Emission spectra for **2** without and with 100 equivalents Zn^{2+} (λ_{ex} = 400 nm). All spectra were acquired in DMSO with 10% H$_2$O (v/v).

scattering from the relatively insoluble Fe(II) perchlorate salt. The lack of spectral shifts suggests that either the ions are coordinating but have no influence, or far more likely is that these metal ions do not coordinate to **1** under these conditions.

In contrast, notable bathochormic shifts in absorption (Figure 6.3a) can be observed upon the addition of Hg^{2+}, Zn^{2+}, Co^{2+}, and Cu^{2+} with the largest shift for the Ni^{2+} solution (0.33 eV). While most retain the vibrational structure, there is significant broadening in the presence of Hg^{2+} the origin of which is currently unclear to us. In the presence of Co^{2+}, a new, broad low energy shoulder from 500-600 nm which may be due to a new MLCT transition like those observed in the Pt(II)BPI complexes.[178] For these metal ions, we attribute the spectral shift to metal ion coordination to the 2,5-bis(2-pyridylimino)pyrrole portion of the molecule which effectively pulls electron density away from the π-system and lowers the energy of the π-π* transition. The absence of absorption features for pure **1** and complete shift in the spectra indicates that for these cations, there is irreversible and/or at least heavily coordination favoured

metal ion binding to the dye. It is important to note that despite metal ion coordination, no emission enhancement was observed from these complexes ($\Phi_{em} < 0.01\%$).

For the absorption spectra of complex **2** in the presence of dications, similar trends were observed as with **1**. That is, a nominal shift in absorption or emission with Ba^{2+}, Ca^{2+}, Cd^{2+}, Fe^{2+}, Mg^{2+}, Mn^{2+}, and Sr^{2+} but bathochormic shifts in absorption with Hg^{2+}, Zn^{2+}, Co^{2+}, Cu^{2+}, and Ni^{2+} (Figure 6.3b). The trend and the magnitude of the shift were similar to as with **1**, which lacks the OH group, suggests that metal ion coordination to **2** is at the 2,5-bis(2-pyridylimino)pyrrole portion of the molecule and not the ESIPT site (i.e. OH—N). Interestingly, for Hg^{2+} and Co^{2+} there is a new, structured, low energy absorption features from 500-620 nm. A similar spectral feature was observed in 5,6-dichloro-1,3-bis(2-pyridylimino)-4,7-dihydroxyisoindole and can be attributed to absorption from the keto form of molecule (i.e. O⁻ and NH form). This observation is important in that it indicates that metal ion coordination is an effective means of perturbing the enol-keto equilibrium even in the ground state of the 1,3-bis(2-pyridylimino)-4,7-dihydroxyisoindole dye. While relatively weak, at sufficiently high concentrations this feature results in a dramatic, visibly obvious, color change of **2** upon addition of Hg^{2+} and Co^{2+} (Figure 6.4) making it a promising candidate for colorimetric sensing.
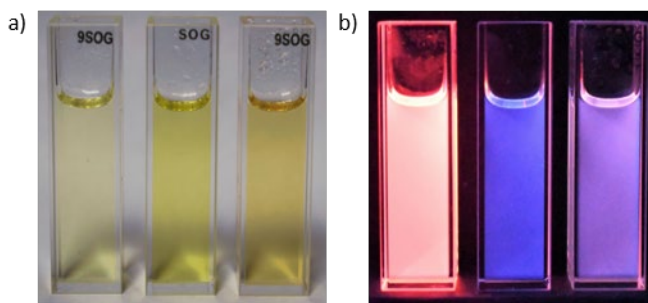
Figure 6.4 Photograph of solutions containing **2** (left), **2** with Hg^{2+} (middle), and **2** with Co^{2+}(right) perchlorate salts in DMSO with 10% H_2O (v/v) under ambient light (a) and UV irradiation (b).

The cation coordination also influences the emissive behaviour of **2** and the results are summarized in Figure 6.3 and Table 6.1. As with absorption, the non-coordinating cations had minimal influence on the energy ($\lambda_{em} \approx 610$ nm), lifetime ($\tau \approx 3.5$ ns) or quantum yield ($\Phi_{em} \approx 25\%$) of emission from **2** (Table 6.1). On the other hand, coordination with Co^{2+}, Cu^{2+}, Hg^{2+}, and

Ni^{2+} completely quenched emission from **2** ($\Phi_{em} < 0.01\%$). While we have not definitively established a mechanism, excited state quenching by these ions is not unusual and is often attributed to either excited state electron transfer or paramagnetic quenching.[179]

Remarkably, coordination of Zn^{2+} not only shifted the enol emission peak to 630 nm (Figure 6.2c) but also more than doubled the excited state lifetime (τ = 7.4 ns) and emission quantum yield (Φ_{em} = 58%) of **2**. The emission enhancement can be attributed to the nearly 3-fold decrease in the non-radiative decay rate of Zn-**2** ($k_{nr} = 1.0 \times 10^8$ s^{-1}) relative to **2** ($k_{nr} = 2.5 \times 10^8$ s^{-1}). While we don't have evidence to directly support the claim, one can envision metal ion coordination increasing the rigidity of the molecule and inhibiting vibrational relaxation modes. Regardless of the mechanism, as far as we know this is the highest emission quantum yield every reported for an ESIPT dye. Additionally, the spectral shift and increase emission intensity are sufficiently large to visually differentiate the sample with and without Zn^{II} ions.

Table 6.1 (a) 100eq M^{II} perchlorate salts relative to sensor. (b) Emission data acquired using dilute solutions (5×10^{-7} M) of sensor in 10%H_2O in DMSO.

[a] M^{II}	BPI-2 [b]				
	λ_{max} (nm)	τ (ns)	ϕ	k_r (x 10^8 s^{-1})	k_{nr} (x 10^8 s^{-1})
-	610	3.1	0.25	0.8	2.4
Ba^{II}	610	3.5	0.35	1.0	1.9
Ca^{II}	610	3.9	0.29	0.7	1.8
Cd^{II}	610	3.3	0.24	0.7	2.3
Co^{II}	-	-	<0.01%	-	-
Cu^{II}	-	-	<0.01%	-	-
Fe^{II}	610	3.4	0.41	1.2	1.7
Hg^{II}	-	-	<0.01%	-	-
Mg^{II}	610	4.0	0.27	0.7	1.8
Mn^{II}	610	3.6	0.14	0.4	2.3
Ni^{II}	-	-	<0.01%	-	-
Sr^{II}	610	3.7	0.27	0.7	2.0
Zn^{II}	630	4.1	0.58	1.4	1.0

Previous reports indicate that Zn^{2+} can coordinate to BPI in either tetrahedral[169] or octahedral[180] geometries. Given the remarkable enhancement in photophysical properties, we sought to gain structural insights into the Zn-**2** adduct observed here. Unfortunately, all attempts to grow crystals of the Zn-**2** were unsuccessful. Instead, we monitored changes in the ^1H NMR spectrum of **2** in DMSO-d6 upon the addition of Zn^{2+} ions and the results can be seen in Figure 6.5. In the absence of Zn^{2+}, compound **2** exhibits five well defined peaks from 7.0-9.0 ppm indicating a plane of symmetry bisecting the isoindole portion of the molecule. The peak assignments for this region, four from the pyridyl ring (H_{b-e}) and one from the isoindole (H_a), are shown in Figure 6.5.

Upon the addition of $Zn(ClO_4)_2$ there is a decrease in the peaks associated with **2** and a concurrent increase in an equal number but shifted peaks for Zn-**2**. While the indole proton (H_a) remained largely unaffected, there are notable upfield and down figure shifts for H_e and H_{b-d} (Figure 6.5) that are accompanied by the disappearance of the H_f, isoindoline proton. These changes are consistent with previous reports of Zn^{2+} coordination to the 2,5-bis(2-pyridylimino)pyrrole portion of the molecule[169, 180] and not the ESIPT site. The lack of symmetry breaking that was observed with the tetrahedral Zn-BPI complex reported by Anderson et al.[169] suggests **2** is binding Zn^{2+} via a tridentate and octahedral coordination environment.[180]
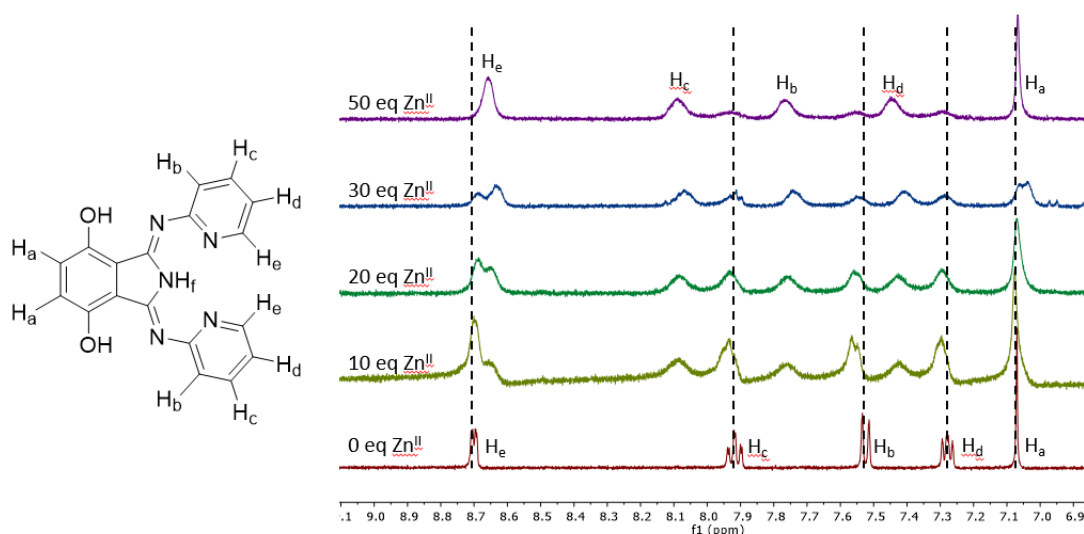
Figure 6.5 ^1H NMR spectra of **2** during a titration with 0 to 50 equivalents of $Zn(ClO_4)_2$.

To investigate the binding stoichiometry of **2** with Zn^{2+} we employed the method of continuous variations, otherwise known as a Job plot, as has been seen in various other metal ion sensor studies. For this study we employed $Zn(OAc)_2$ as opposed to $Zn(ClO_4)_2$ to ensure deprotonation of the isoindoline position, which is necessary for complexation to occur. We monitored the absorption spectral changes with respect to the molar ratio of Zn^{2+} and the results are shown in Figure 6.6. Spectra were normalized to a peak maximum of one to control for overlap between the keto absorption, absorption of unbound **2**, and absorption of Zn-**2**. From the absorption spectra intensities at 443 nm we constructed the Job plot shown in Figure 6.6. The peak maximum occurred at a molar ratio of 0.335 Zn^{2+} which is indicative of an AB_2 binding
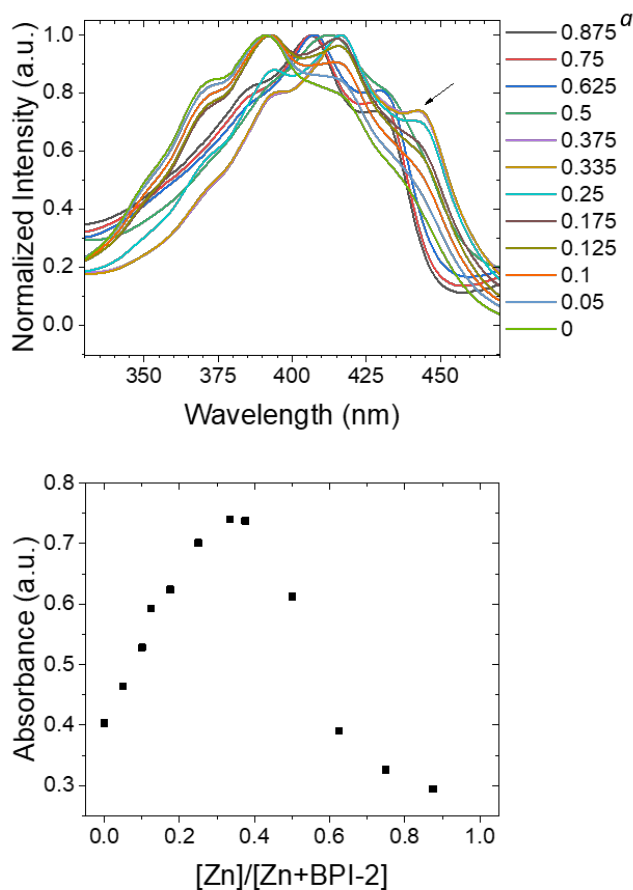
Figure 6.6 (Top) Normalized UVVis absorbance spectra for Job plot with varying molar ratios of $Zn(OAc)_2$ and BPI-2 in DMSO with a total concentration of 0.05 mM. [a] Ratios on the right are calculated by $X_A/(X_A + X_B)$ where X_A = $Zn(OAc)_2$ and X_B = BPI-2. (Bottom) Job plot constructed from the absorbance intensity at 443 nm.

motif.[32] The sigmoidal curvature to the right of the peak maximum is also symptomatic of the AB$_2$ motif.

Collectively these results indicate that Zn^{2+} is octahedrally coordinated to **2** at the 2,5-bis(2-pyridylimino)pyrrolate site of **2** with a stoichiometry of Zn(**2**)$_2$. Similar coordination chemistry was proposed by Gagne et al for Zn(4,4'-dimethylBPI)$_2$.[31] As eluded to above, one can envision this type of Zn^{2+} coordination increasing the rigidity of the molecule and decreasing non-radiative deactivation modes. However, a crystal structure of any Zn(BPI)$_2$ derivative has yet to be reported and thus while all of the data supports the above hypothesis, this structural assignment will remain tentative until a crystal structure can be obtained.

Because of the known solvatochromic characteristics of ESIPT molecules we measured the photophysical properties of **2** in MeOH and MeOD. Additionally, due to the sensitivity of these materials to pH we changed the counter ion from perchlorate to acetate and the results are summarized in Table 6.2.

Table 6.2 Photophysical data for **BPI-2** and its Zn^{II} complexes with different solvents and counter ions (a) Emission data acquired using dilute solutions (~5 × 10^{-7} M).(b) 100eq of each salt added relative to counter ion concentration (c) $k_r = \Phi/\tau$. (d) $k_{nr} = (1-\Phi)/\tau$.

Entry	Solvent	Salt[b]	Emission at rt[a]			k_r (× 10^{8}s^{-1})[c]	k_{nr} (× 10^{8}s^{-1})[d]
			λ_{max} (nm)	τ (ns)	Φ_{PL}		
1	DMSO	-	616	2.99	0.25	0.84	2.5
2	DMSO	NaOAc	616	6.26	0.12	0.19	1.4
3	DMSO	Zn(ClO$_4$)$_2$	631	4.01	0.6	1.5	1.0
4	DMSO	Zn(OAc)$_2$	631	7.97	0.68	0.85	0.40
5	MeOD	-	592	6.72	0.11	0.16	1.3
6	MeOD	NaOAc	595	6.81	0.23	0.34	1.1
7	MeOD	Zn(ClO$_4$)$_2$	615	8.23	0.1	0.12	1.1
8	MeOD	Zn(OAc)$_2$	617	10.4	0.34	0.33	0.64
9	MeOH	-	594	3.82	0.23	0.60	2.02
10	MeOH	NaOAc	596	3.90	0.09	0.23	2.34
11	MeOH	Zn(ClO$_4$)$_2$	606	4.34	0.28	0.65	1.66
12	MeOH	Zn(OAc)$_2$	615	8.79	0.48	0.55	0.59

Across all solvent systems we observe an increase in the radiative rate of decay (k_r) and a decrease in the non-radiative rate of decay (k_{nr}) in the presence of Zn^{II} relative to neat **BPI-2** in each respective solvent. We attribute this to the Zn^{II} coordination enhancing structural rigidity of the **BPI-2** ligands which is expected to facilitate radiative decay pathways. Comparing counter ions across all solvents shows that the relatively basic acetate produces uniformly lower k_{nr} presumably as a result of the further increased rigidity from the anionic form of **BPI-2**. Perhaps the most interesting unintended consequence of these experiments was the observation that entry 3 produced a yellow solution while entry 11 resulted in a bright pink colour despite only changing the solvent. The solution in methanol demonstrated an increased keto absorption feature for **BPI-2** which indicates that the pK_a of the phenolic proton is decreased by both the MeOH and by coordination to Zn^{II}.

Analyte induced cleavage of a protecting group on the proton donor site of an ESIPT dyes is an appealing strategy to realize turn-on fluorescence detection of species like H_2S, O_2^-, $ONOO^-$, and hydrazine[177]. The latter, is of particular interest because hydrazine is an acutely toxic and carcinogenic compound that is commonly used in many industrial, agricultural and pharmaceutical processes. As previously demonstrated by Goswami et al., a bromobutyrate alcohol protecting group is readily cleaved in the presence of hydrazine resulting in turn-on fluorescence.[177] To further expand the detection capabilities of **2**, we generated the compounds **3** and **4** containing a single Boc and both Boc and bromobutyrate phenolic protecting groups, respectively.

The similarity in photophysical properties between **2** and **3** is not surprising in that it has previously been demonstrated that one alcohol group of **2** is sufficient for ESIPT to occur.[173, 174] However, the addition of both Boc and bromobutyrate phenolic protecting groups to **2** results in compound **4** whose photophysical properties more closely resemble non-emissive **1** ($\Phi_{em} <$ 0.01%). This behaviour can be rationalized by the lack of OH donor for the ESIPT process to occur which prevents keto emission that is observed in **2** and **3**. At time 0 (i.e. prior to N_2H_4 addition) no emission was observed. However, immediately after the introduction of N_2H_4, bright orange emission was readily apparent, even to the naked eye. The emission intensity continued to increase until plateauing ~20 minutes after the initial addition. The emission spectra are consistent with the keto-type emission that is observed with **2** and **3**.
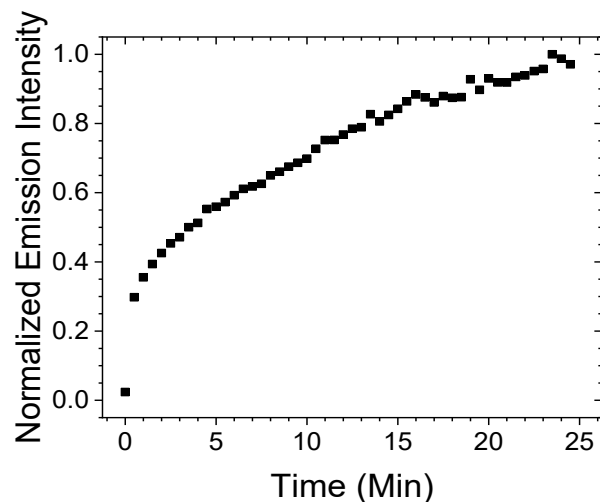
Figure 6.7 Hydrazinolysis of **4** in DMSO upon the addition of 2.2 equivalents of N_2H_4 monitored by fluorescence spectroscopy (λ_{ex} = 390 nm) every 30 seconds. Emission intensity recorded at 610 nm.

Following completion of the reaction, the solution was quenched with dilute HCl, concentrated in vaccuo, and analysed by ^{1}H NMR. Unexpectedly, hydrazine was capable of cleaving both the Boc and bromobutyrate protecting groups effectively converting **4** into **2**. Equally important is, as can be seen by the UV-Vis spectra and analogous to the NaOAc treatments in entry 2 of Table 6.2, the hydrazine solution was sufficiently basic to deprotonate **2** resulting in the keto form for both the ground and excited state of **2**. Thus, under these conditions, **4** does exhibit turn-on fluorescence in the presence of N_2H_4 but it is not by enabling an ESIPT mechanism but instead by excitation and emission from the deprotonated, keto form of **2**. Presumably, in a sufficiently acidic medium, the deprotected form of **4** would be protonated and exhibit ESIPT characteristics (i.e. no keto absorption but keto emission). None the less, the dramatic change in both absorption and emission spectra and intensities of **4** in DMSO makes this a promising molecule for the detection of hydrazine.

It is worth noting that from the UV-Vis, emission, and NMR measurements, the same metal ion interactions described above in section 6.2 and 6.3 for **1** and **2**, are also active in molecules **3** and **4**. While not explored here, this indicates that different combinations of metal ion, hydrazine, and molecule **4** will result in unique spectral signatures (i.e. turn on fluorescence, absorption/emission shifts, etc) which could open the door to complex, multicomponent detection schemes.

80

While investigating the role of the counter ion we decided to test whether using acetate would influence Cd^{2+} binding to **2**. Initial experiments with HNMR and UVVis indicated no binding to $Cd(ClO_4)_2$ but using $Cd(OAc)_2$ in DMSO red shifted and broadened the emission spectrum to 640 nm. This evidence suggests that the reason **1** was able to bind to Cd^{2+} while **2** was not is the decreased acidity of the isoindoline proton due to the electron donating nature of the alcohols on **2.** The binding affinity to Zn^{2+} must be high enough for deprotonation but Cd^{2+} required the proton to be removed prior to coordination.
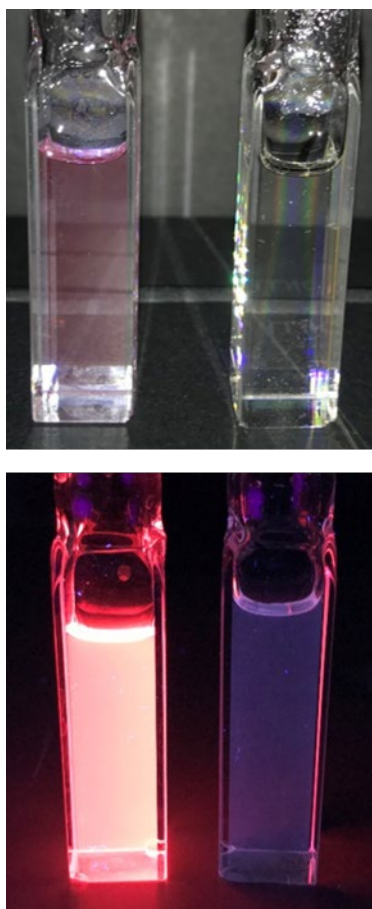
Figure 6.8 Photograph of solutions containing **4** without (left) and with (right) N_2H_4 in DMSO under ambient light (top) and UV irradiation (bottom).

The preferential binding of **2** with Zn^{2+} and Hg^{2+} compared to Cd^{2+}, combined with the emission quenching upon coordination to Hg^{2+} allowed us to develop the sensing scheme seen in Figure 6.9. 100 equivalents of each perchlorate salt was added to a 0.02mM solution of **2** in 10% H_2O in DMSO. The absorption shift upon coordination to Zn^{2+} and Hg^{2+} is apparent from the darkening of the yellow colored solutions. Observing the samples under illumination from a
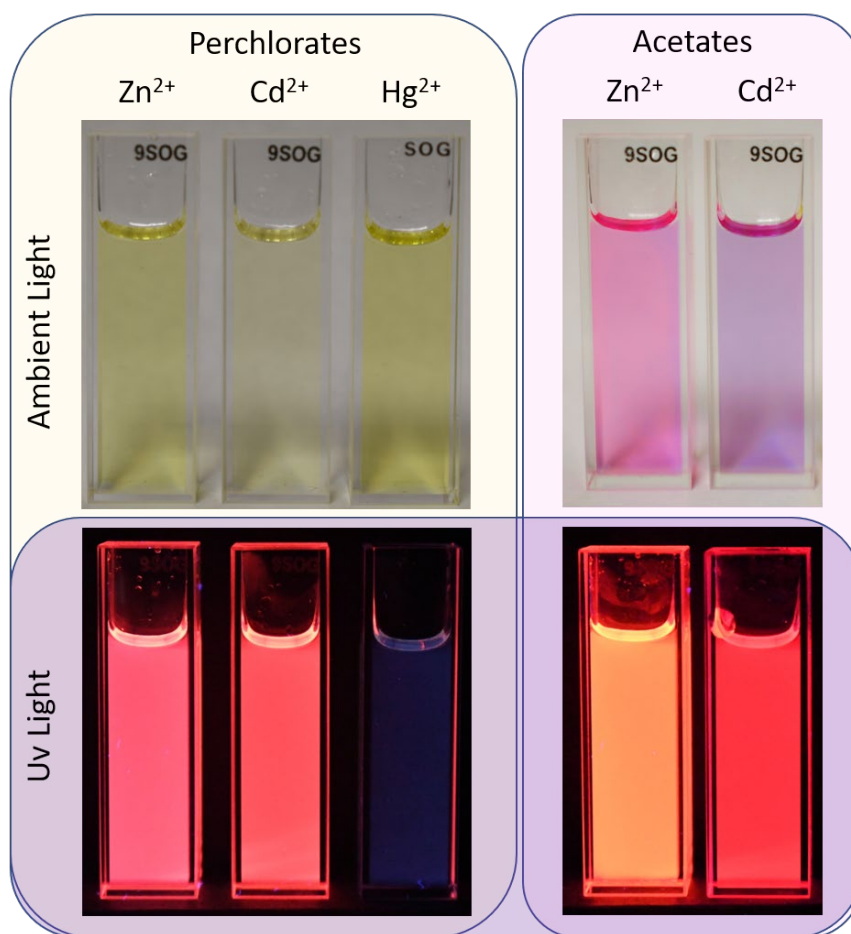
Figure 6.9 Sensing scheme depicting the unique photophysical properties of **2** with 100 eq of metal perchlorates under ambient light (top left) and UV light (bottom left). Following the addition of 100eq of NaOAc, Cd^{2+} coordinated to **2** producing the solutions pictured under ambient light (top right) and under Uv light (bottom right).

365nm UV lamp revealed the bright red shifted fluorescence of Zn-**2**, the typical orange keto emission from **2**, and finally the near complete quenching of emission of Hg-**2**. Further clarification of sample identity can be obtained by adding 100 equivalents of NaOAc to facilitate the coordination of **2** and Cd^{2+}. Both solutions display bright purple coloration in ambient light, due to their new keto absorption features from the addition of acetate. Finally, UV light reveals the deeper red emission of Cd-**2** which is easily distinguished from the brighter and yellower Zn-**2**.

In the present work we demonstrated the utility of **BPI-2** as a novel M^{II} sensor with the ability to differentiate Zn^{II}, Cd^{II}, and Hg^{II} from each other which is a typically difficult task. The

extreme quantum yield increase after Zn^{II} coordination from 0.25 to 0.6 is among the highest reported for ESIPT fluorophores.

CHAPTER 7

CONCLUSIONS

In chapter 3 we explored the utility of ESPT as an enantioselective proton source. The ability of the atropisomeric dye VANOL to donate a proton to several silyl enol ethers demonstrated that this class of compound shows great potential for use as a novel method for creating enantioenriched products. At present the utility of this work is primarily limited by the only moderate enantioselectivity as well as the non-catalytic nature of this system.

Previous work by Das et al utilized phenol as a sacrificial acid in order to use 2-naphthol as a catalytic photoacid. After the ESPT event irreversibly protonated a silyl enol ether, the dye would relax to the ground state anion where it was incapable of participating in another reaction cycle. With the addition of phenol, the anion could be protonated by accepting a hydrogen ion from the sacrificial acid. The sacrificial acid allows naphthol; to be used catalytically. However, when we attempted a similar sacrificial acid technique with the Br-VANOL system we observed no enantioselectivity. While phenol acts as a proton donor to deprotonated ground state photoacids, it can also act as a proton acceptor to the excited state enol. There is a strong likelihood that there is a hydrogen bond between phenol and VANOL in the ground state. This hydrogen bond would result in a preferential proton transfer to the phenol before proton transferring to the substrate, followed by a proton transfer event to the substrate. While the silyl enol ether is eventually converted to the ketone in both cases, enantioselectivity is eliminated when phenol acts as an intermediary proton source.

A potential solution to this problem would be the use of a non-hydrogen bonding sacrificial acid. While Bronsted-Lowry proton sources are typically capable of H bonding, the use of steric hindrance may be able to reduce or eliminate the intermolecular interaction. Phenol ortho substituted with either methyls, isopropyls, or tertbutyls are potential candidates for this purpose.

Another problem plaguing this system was identified above as the photo racemization of BINOL. Under UV-irradiation many atropisomeric compounds are known to racemize which limits their potential as enantiogenic compounds. While Br-VANOL was able to enantioselectively protonate our substrate, the scope of potential reagents is limited by the

necessity of finding other atropisomers that do not photo racemize. Future work on this project may include the use of a point chiral center as opposed to an axially chiral molecule, as this would inhibit the racemization in the excited state.

This system was relatively successful given the narrow scope of ESPT dyes explored. In enantioselective catalysis much thought is given to the chiral pocket which the substrate molecule interacts with before/during the protonation event. Modifying the steric hindering groups around the ESPT sites may improve the selectivity of this reaction. In other atropisomeric proton transfer catalysts, triisopropylphenyl, ditertbutylphenyl, and others are incorporated adjacent to the aromatic alcohols with very high ee reported.

In chapter 4 we were able to exploit what is typically regarded as a detrimental process to a productive one, by using the planarization event of excited state BINOL to enantioenrich a racemic mixture of the substance. Classic enantiopurification schemes involve removal of the unwanted enantiomer, which is both wasteful and time consuming. The most unique feature of our system relative to others is that the unwanted enantiomer is not removed, but rather converted into the desired one. For a compound such as BINOL this is largely unnecessary, due to the myriad of methods for both synthesizing enantiopure BINOL as well as the hundreds of known ways to separate enantiomers from each other.

However, what makes this work noteworthy is not BINOL itself but the novel possibility that atropisomeric compounds may be preferentially converted between one atropisomer and the other. Potentially this could be used to enantioenrich one of the many atropisomeric pharmaceutical products or it may be useful to enantioenrich more difficult to synthesize substituted BINOL compounds which are very expensive but also widely employed in asymmetric synthesis.

The most interesting observation through the course of this work was the photostationary equilibrium between S/R atropisomers. We found that both the degree and direction of enantioenrichment was an intrinsic property of the chiral auxiliary group used. While the ideal scenario would be to have a 100% ee, varying degrees of ee gives us a unique insight to the chiral induction capabilities of the amino acids. From the limited selection we tested it was fairly obvious that proximity of the point chiral center to the atropisomeric center had a large effect on the extent of enantioenrichment. We also observed that the rotational freedom of a specific amino acid was inversely correlated to the ee. Initially calculations demonstrated that it may be

possible to predict these effects which would have massive utility in designing similar systems, however further work is necessary to refine the technique.

One of the more interesting extensions of this project would be to expand the repertoire of atropisomers tested beyond BINOL to both 3,3' substituted BINOLs and other parent atropisomers. BINOL itself rarely finds utility in asymmetric catalysis anymore due to the higher stereoselectivity of its sterically hindered derivatives. Not only are these materials more expensive, and therefore more useful in their enantioenriched forms, but the added steric bulk near the chiral directing group will likely affect the extent of the enantioenrichment. Initial probes of this idea showed that 3,3''triisopropylphenyl-boc-pro-BINOL could be synthesized however resolving the material on SFC proved difficult to achieve.

In a world that is increasingly bathed in artificial light having access to a multitude of emissive materials is essential. To contribute to this body of technology, in chapter 5 we designed and synthesized new emissive MOFs based on ESIPT dyes. Our efforts to design and employ a new tunable emissive material proved modestly successful. Metal organic frameworks have only seldom been used as emissive materials in the past and this was the first example of a 3 component ESIPT MOF. The crystalline nature and stability of this framework is noteworthy and very important if these types of material are to have a practical application. Many MOFs made to date are not stable to air or moisture, however our system demonstrated excellent hydro and thermal stability.

Utilizing a 3-component system of red, green, and blue emissive linkers was intended to simulate the tricolor approach to color generation used by most emissive screens on the market today. Theoretically, every color contained within the triangle formed by the three points on the CIE coordinate diagram that correspond to the linker colors can be reproduced by this system. Therefore, selecting colors that exist close to the edge of the color coordinate plot is essential to a large range of color generation.

Initially it appeared from the high doping MOFs that we had excellent color purity for red, green, and blue due to the observed complete emission from the keto state. However, attempts to mix the colors resulted in unpredictable emission profiles. Later we found that the extremely high doping of 10% fluorophore was inner filtering the enol emission from the linkers instead of them exclusively emitting from the keto state. This energy transfer event resulted in highly unpredictable emission color and limited the range of colors we could reproduce.

Switching to lower doping systems resulted in a more reliable color generation and we were able to more or less predict the color of two component systems. The range of potential colors was somewhat diminished due to the increased presence of enol emission. Because the enol emission does not benefit from the large apparent Stokes shift of ESIPT all three dyes exhibited a blue shifted CIE coordinate. The innovation of using less concentrated MOFs accidentally led us to a two-component solution to obtaining white light. The enol emission from the green and red dyes allowed us to cover the entire visible spectrum with these fluorophores alone.

Of particular interest from this study was the high CRI values obtained from the substituted metal organic frameworks. It is very important in luminescent materials to be able to accurately reproduce the colors of different objects. A white light source may appear white if it activates each of our eyes cones the right amount, but if the bandwidth is very narrow then light reflected back at us will appear dull and washed out. The broadband nature of the 3 component white light emitters resulted in an extremely high CRI of 95 which is competitive with the highest industrial standard to date.

Finally, we close out this dissertation with a discussion of the sensing properties of the ESIPT fluorophore BPI-2 in chapter 6. Perhaps the most interesting feature of this system is the incorporation of a fluorophore and metal chelator into a single functional unit as opposed to many classical methods which covalently link two distinct pieces to achieve the same effect. It appears that having these two properties closely associated has caused a dramatic increase in its sensitivity. The ease of application for this system was demonstrated through it's ability to accurate detect metal analytes even in mixed solvent systems of water and DMSO, allowing it to be utilized in the field without lengthy lab preparations.

We have found that this system has an incredibly high quantum yield upon coupling to zinc and demonstrated that this may be used to create a "turn-on" sensing system where upon contact between the two materials the system brightly fluoresces in UV light. This property has also been demonstrated to be able to differentiate zinc, cadmium, and mercury from each other. These elements are notoriously difficult to separate and differentiate from one another. BPI-2 was shown to bind zinc and emit brightly with no other additions, while cadmium shows no binding or emission changes until after base is added. Mercury appears to bind without the need

of base, however the emission intensity decreases markedly. These features allow for a simple, albeit effective, determination of any of their presence in the target analyte.

The ability of the BPI ESIPT fluorophore to detect hydrazine is also worth noting. The BPI-4 system appears to be entirely non-emissive until addition of hydrazine cleaves the protecting groups from the alcohols, which increases or "turns-on" the emission by several orders of magnitude.

REFERENCES

(1)   L. T. M., *43-47*, 1923, **42**, 43-47.

(2)   L. M. Tolbert and K. M. Solntsev, *Acc. Chem. Res.*, 2002, **35**, 19-27.

(3)   A. P. Demchenko, K.-C. Tang and P.-T. Chou, *Chemical Society Reviews*, 2013, **42**, 1379-1408.

(4)   T. G. Kim and M. R. Topp, *J. Phys. Chem. A*, 2004, **108**, 10060-10065.

(5)   T. Kumpulainen, B. Lang, A. Rosspeintner and E. Vauthe, *Chem. Rev.*, 2017, **117**, 10826-10939.

(6)   E.-A. Gould, A. V. Popov, L. M. Tolbert, I. Presiado, Y. Erez, D. Huppert and K. M. Solntsev, *Phys. Chem. Chem. Phys.,*, 2012, **14**, 8964-8973.

(7)   M. Kasha, *Discuss. Faraday Soc.*, 1950, **9**, 14-19.

(8)   J. R. Lakowicz, *Principles of fluorescence spectroscopy*, Springer Science & Business Media, 2013.

(9)   K. Weber, *Z. Phys. Chem.   Abt. B*   1931, **15**, 18-44.

(10)   H. E. A. Kramer and P. Fischer, *Chem Phys Chem*, 2020.

(11)   T. Förster, *Z. Elektrochem. Angew. Phys. Chem.*, 1950, **54**, 531-535.

(12)   A. C. Sedgwick, L. Wu, H.-H. Han, S. D. Bull, X.-P. He, T. D. James, J. L. Sessler, B. Z. Tang, H. Tian and J. Yoon, *Chem. Soc. Rev.*, 2018, **47**, 8842-8880.

(13)   J. Zhao, S. Ji, Y. Chen, H. Guo and P. Yang, *Physical Chemistry Chemical Physics*, 2012, **14**, 8803-8817.

(14)   J. E. Kwon and S. Y. Park, *Advanced Materials*, 2011, **23**, 3615-3642.

(15)   J. Huang, A. P. Muliawan, J. Ma, M. D. Li, H. K. Chiu, X. Lan, D. Deodato, D. L. Phillips and T. M. Dore, *Photochem. Photobiol. Sci.*, 2017, **16**, 575-584.

(16)   V. S. Padalkar and S. Seki, *Chem. Soc. Rev.*, 2016, **45**, 169-202.

(17)   R. Das, G. Duportail, A. Ghose, L. Richert, A. Klymchenko, S. Chakraborty, S. Yesylevskyy and Y. Mely, *Phys. Chem. Chem. Phys.*, 2014, **16**, 776-784.

(18)   K. Jayaramulu, P. Kanoo, S. J. George and T. K. Maji, *Chem. Commun.*, 2010, **46**, 7906-7908.

(19)   P. Zhou and K. Han, *Acc. Chem. Res.*, 2018, **51**, 1681-1690.

(20)   A. Weller,   *Z. Elektrochem. Ber. Bunsenges. Phys. Chem.*   , 1964, **56**, 662 – 668.

(21)   M. Eigen, *Angew. Chem. Int. Ed.*, 1964, **3**, 1– 19.

(22)   M. Eigen, *Angew. Chem.*, 1963, **75**, 4 89 – 508.

(23)   N. Agmon, *J. Phys. Chem. A*, 2005, **109**, 13-35.

(24)   W. R. Laws and L. Brand, *J. Phys. Chem.*, 1979, **83**, 795-802.

(25)   E. C. Meister, M. Willeke, W. Angst, A. Togni and P. Walde, 2014, **97**.

(26)   B. Finkler, C. Spies, M. Vester, F. Walte, K. Omlor, I. Riemann, M. Zimmer, F. Stracke, M. Gerhards and G. Jung, *Photochem. Photobiol. Sci.*, 2014, **13**, 548-562.

(27)   L. M. Tolbert and J. E. Haubrich, *J. Am. Chem. Soc.*, 1994, **116**, 10593-10600.

(28)   I. Presiado, N. Karton-Lifshin, Y. Erez, R. Gepshtein, D. Shabat and D. Huppert, *J. Phys. Chem. A 116, 27, 7353-7363*, 2012, **116**, 7353-7363.

(29)   J. E. Kwon and S. Y. Park, *Advanced Materials*, 2011, **23**, 3615-3642.

(30)   D. D. Pant, H. C. Joshi, P. B. Bisht and H. B. Tripathi, *Chemical Physics*, 1994, **185**, 137-144.

(31)   P. T. Chou, M. L. Martinez and J. H. Clements, *The Journal of Physical Chemistry*, 1993, **97**, 2618-2622.

(32)   D. Y. Han, J. M. Kim, J. Kim, H. S. Jung, Y. H. Lee, J. F. Zhang and J. S. Kim, *Tetrahedron Letters*, 2010, **51**, 1947-1951.

(33)   M. H. Van Benthem and G. D. Gillispie, *The Journal of Physical Chemistry*, 1984, **88**, 2954-2960.

(34)   H.-W. Tseng, J.-Q. Liu, Y.-A. Chen, C.-M. Chao, K.-M. Liu, C.-L. Chen, T.-C. Lin, C.-H. Hung, Y.-L. Chou, T.-C. Lin, T.-L. Wang and P.-T. Chou, *The Journal of Physical Chemistry Letters*, 2015, **6**, 1477-1486.

(35)   O. K. Abou-Zied, R. Jimenez, E. H. Z. Thompson, D. P. Millar and F. E. Romesberg, *The Journal of Physical Chemistry A*, 2002, **106**, 3665-3672.

(36)   P. K. Sengupta and M. Kasha, *Chemical Physics Letters*, 1979, **68**, 382-385.

(37)   J. Seo, S. Kim and S. Y. Park, *Journal of the American Chemical Society*, 2004, **126**, 11154-11155.

(38)   Y. Marcus, *New York*, 1985.

(39)   K. M. Solntsev, D. Huppert and N. Agmon, *The Journal of Physical Chemistry A*, 1998, **102**, 9599-9606.

(40)   B.-Z. Magnes, N. V. Strashnikova and E. Pines, *Israel Journal of Chemistry*, 1999, **39**, 361-373.

(41)   N. Barrash-Shiftan, B. Brauer and E. Pines, *Journal of Physical Organic Chemistry*, 1998, **11**, 743-750.

(42)   M. J. Kamlet, J. L. M. Abboud, M. H. Abraham and R. W. Taft, *The Journal of Organic Chemistry*, 1983, **48**, 2877-2887.

(43)   B. J. Schwartz, L. A. Peteanu and C. B. Harris, *The Journal of Physical Chemistry*, 1992, **96**, 3591-3598.

(44)   G. A. Brucker, D. F. Kelley and T. C. Swinney, *The Journal of Physical Chemistry*, 1991, **95**, 3190-3195.

(45)   G. O. W. Lins, L. F. Campo, F. S. Rodembusch and V. Stefani, *Dyes and Pigments*, 2010, **84**, 114-120.

(46)   M. K. Nayak and S. K. Dogra, *Journal of Photochemistry and Photobiology A: Chemistry*, 2005, **171**, 281-290.

(47)   M. Mosquera, J. C. Penedo, M. C. Ríos Rodríguez and F. Rodríguez-Prieto, *The Journal of Physical Chemistry*, 1996, **100**, 5398-5407.

(48)   X. Shi, P. Abbyad, X. Shu, K. Kallio, P. Kanchanawong, W. Childs, S. J. Remington and S. G. Boxer, *Biochemistry*, 2007, **46**, 12014-12025.

(49)   Q. J. Meisner, A. H. Younes, Z. Yuan, K. Sreenath, J. J. M. Hurley and L. Zhu, *The Journal of Physical Chemistry A*, 2018, **122**, 9209-9223.

(50)   C. Azarias, Š. Budzák, A. D. Laurent, G. Ulrich and D. Jacquemin, *Chemical Science*, 2016, **7**, 3763-3774.

(51)   L. G. T. A. Duarte, J. C. Germino, C. d. Á. Braga, C. A. Barboza, T. D. Z. Atvars, F. d. S. Santos and F. S. Rodembusch, *Photochemical & Photobiological Sciences*, 2018, **17**, 231-238.

(52)   p.-P. MorletSavaryaPatriceJacquesaXavierAllonasaHélèneChaumeilbAlbertDefoinbChristiane Carréc, *Chemical Physics Letters*, 2008, **455Issues 4–6, 10 April 2008, Pages 238-241**, 238-241.

(53)   G. R. Colin J. Martin, Takuya Nakashima, Tsuyoshi Kawai,, *Journal of Photochemistry and Photobiology C: Photochemistry Reviews,*, 2018, **34**, 41-51.

(54) Y. Xia and L. Peng, *Chem. Rev.*, 2013, **113**, 7880-7929.

(55) X. Yue, C. O. Yanez, S. Yao and K. D. Belfield, *J. Am. Chem. Soc.*, 2013, **135**, 2112-2115.

(56) P. Yang and W. Yang, *Chem. Rev.*, 2013, **113**, 5547-5594.

(57) M. A. C. Stuart, W. T. S. Huck, J. Genzer, M. Müller, C. Ober, M. Stamm, G. B. Sukhorukov, I. Szleifer, V. V. Tsukruk, M. Urban, F. Winnik, S. Zauscher, I. Luzinov and S. Minko, *Nature Materials*, 2010, **9**, 101-113.

(58) F. Wendler, J. C. Tom and F. H. Schacher, *Polym. Chem.*, 2019, **10**, 5602-5616.

(59) F. Wendler, K. R. A. Schneider, B. Dietzek and F. H. Schacher, *Polym. Chem.*, 2017, **8**, 2959-2971.

(60) H. Kagel, F. F. Bier, M. Frohme and J. F. Glökler, *Scientific Reports*, 2019, **9**, 1-6.

(61) S. Kohse, A. Neubauer, A. Pazidis, S. Lochbrunner and U. Kragl, *J. Am. Chem. Soc.*, 2013, **135**, 9407-9411.

(62) A. Das, T. Banerjee and K. Hanson, *Chem. Commun.*, 2016, **52**, 1350-1353.

(63) M. R. Loken, J. W. Hayes, J. R. Gohlke and L. Brand, *Biochemistry*, 1972, **11**, 4779-4786.

(64) D. Yang, Z. Li, Y. Allan Diwu, H. Fu, J. Liao, C. Wei and Z. Diwu, *Curr Chem Genomics*, 2008, **2**, 48-50.

(65) V. Posey and K. Hanson, *ChemPhotoChem*, 2019, **3**, 580-604.

(66) M. D. McGehee and A. J. Heeger, *Advanced Materials*, 2000, **12**, 1655-1668.

(67) A. U. Khan and M. Kasha, *Proc Natl Acad Sci U S A*, 1983, **80**, 1767-1770.

(68) K.-Y. Chen, C.-C. Hsieh, Y.-M. Cheng, C.-H. Lai and P.-T. Chou, *Chem. Commun.*, 2006, 4395-4397.

(69) S. K. and, S. Y. Park*, Iori Yoshida, a. Hideki Kawai and T. Nagamura, *J. Phys. Chem. B*, 2002, **106**, 9291-9294.

(70) S. Park, J. E. Kwon, S. H. Kim, J. Seo, K. Chung, S.-Y. Park, D.-J. Jang, B. M. Medina, J. Gierschner and S. Y. Park, *J. Am. Chem. Soc.*, 2009, **139**, 14043-14049.

(71) A. Das, S. Ayad and K. Hanson, *Organic Letters*, 2016, **18**, 5416-5419.

(72) J. Halpern and B. M. Trost, *Proc. Natl. Acad. Sci. U. S. A.*, 2004, **101**, 5347.

(73) D. M. Schultz and T. P. Yoon, *Science*, 2014, **343**.

(74)   R. Brimioulle, D. Lenhart, M. M. Maturi and T. Bach, *Angew. Chem., Int. Ed.*, 2015, **54**, 3872– 3890.

(75)   M. Neumann, S. Füldner, B. König and K. Zeitler, *Angewandte Chemie International Edition*, 2011, **50**, 951-954.

(76)   Y.-Q. Zou, J.-R. Chen, X.-P. Liu, L.-Q. Lu, R. L. Davis, K. A. Jørgensen and W.-J. Xiao, *Angewandte Chemie International Edition*, 2012, **51**, 784-788.

(77)   J. Du, K. L. Skubi, D. M. Schultz and T. P. Yoon, *Science*, 2014, **344**, 392-396.

(78)   N. A. Romero, K. A. Margrey, N. E. Tay and D. A. Nicewicz, *Science*, 2015, **349**, 1326-1330.

(79)   H. Huo, X. Shen, C. Wang, L. Zhang, P. Röse, L.-A. Chen, K. Harms, M. Marsch, G. Hilt and E. Meggers, *Nature*, 2014, **515**, 100-103.

(80)   D. P. Hari, P. Schroll and B. König, *Journal of the American Chemical Society*, 2012, **134**, 2958-2961.

(81)   J. Eames and N. Weerasooriya, *Tetrahedron: Asymmetry*, 2001, **12**, 1-24.

(82)   C. H. Cheon and H. Yamamoto, *Journal of the American Chemical Society*, 2008, **130**, 9246-9247.

(83)   S. Nakamura, M. Kaneeda, K. Ishihara and H. Yamamoto, *Journal of the American Chemical Society*, 2000, **122**, 8120-8130.

(84)   T. Poisson, V. Gembus, V. Dalla, S. Oudeyer and V. Levacher, *The Journal of Organic Chemistry*, 2010, **75**, 7704-7716.

(85)   H.-L. Liu, H.-P. Zhu, X.-L. Hou and L. Pu, *Organic Letters*, 2010, **12**, 4172-4175.

(86)   F. Wang, R. Nandhakumar, Y. Hu, D. Kim, K. M. Kim and J. Yoon, *The Journal of Organic Chemistry*, 2013, **78**, 11571-11576.

(87)   C. Wang, E. Wu, X. Wu, X. Xu, G. Zhang and L. Pu, *Journal of the American Chemical Society*, 2015, **137**, 3747-3750.

(88)   Q. Wang, X. Chen, L. Tao, L. Wang, D. Xiao, X.-Q. Yu and L. Pu, *The Journal of Organic Chemistry*, 2007, **72**, 97-101.

(89)   S. P. Upadhyay, R. R. S. Pissurlenkar, E. C. Coutinho and A. V. Karnik, *The Journal of Organic Chemistry*, 2007, **72**, 5709-5714.

(90)   K. M. Solntsev, L. M. Tolbert, B. Cohen, D. Huppert, Y. Hayashi and Y. Feldman, *Journal of the American Chemical Society*, 2002, **124**, 9046-9047.

(91)   K. M. Solntsev, D. Huppert, N. Agmon and L. M. Tolbert, *The Journal of Physical Chemistry A*, 2000, **104**, 4658-4669.

(92)   N. Agmon, *The Journal of Physical Chemistry A*, 2005, **109**, 13-35.

(93)   Y. Chen, S. Yekta and A. K. Yudin, *Chemical Reviews*, 2003, **103**, 3155-3212.

(94)   M. Shibasaki and S. Matsunaga, *Chemical Society Reviews*, 2006, **35**, 269-279.

(95)   E. M. Vogl, S. Matsunaga, M. Kanai, T. Iida and M. Shibasaki, *Tetrahedron Letters*, 1998, **39**, 7917-7920.

(96)   D. Parmar, E. Sugiono, S. Raja and M. Rueping, *Chemical Reviews*, 2014, **114**, 9047-9153.

(97)   D. S. McClure, N. W. Blake and P. L. Hanst, *The Journal of Chemical Physics*, 1954, **22**, 255-258.

(98)   D. S. McClure, *The Journal of Chemical Physics*, 1949, **17**, 665-666.

(99)   K. M. Solntsev, E.-A. Bartolo, G. Pan, G. Muller, S. Bommireddy, D. Huppert and L. M. Tolbert, *Israel Journal of Chemistry*, 2009, **49**, 227-233.

(100) M. Flegel, M. Lukeman and P. Wan, *Canadian Journal of Chemistry*, 2008, **86**, 161-169.

(101) M. Cavazza, M. Zandomeneghi, A. Ouchi and Y. Koga, *Journal of the American Chemical Society*, 1996, **118**, 9990-9991.

(102) E. L. Tyson, M. S. Ament and T. P. Yoon, *The Journal of Organic Chemistry*, 2013, **78**, 2046-2050.

(103) S. Ayad, V. Posey, A. Das, J. M. Montgomery and K. Hanson, *Chemical Communications*, 2019, **55**, 1263-1266.

(104) J. Alemán and S. Cabrera, *Chemical Society Reviews*, 2013, **42**, 774-793.

(105) K. W. Quasdorf and L. E. Overman, *Nature*, 2014, **516**, 181-191.

(106) J. M. Brunel, *Chemical Reviews*, 2005, **105**, 857-898.

(107) J.-Z. Wang, J. Zhou, C. Xu, H. Sun, L. Kürti and Q.-L. Xu, *Journal of the American Chemical Society*, 2016, **138**, 5202-5205.

(108) H.-F. Chow, C.-W. Wan and M.-K. Ng, *The Journal of Organic Chemistry*, 1996, **61**, 8712-8714.

(109) J. Jacques, C. Fouquey and R. Viterbo, *Tetrahedron Letters*, 1971, **12**, 4617-4620.

(110) M. Juárez-Hernandez, D. V. Johnson, H. L. Holland, J. McNulty and A. Capretta, *Tetrahedron: Asymmetry*, 2003, **14**, 289-291.

(111) H. Wang, *Chirality*, 2010, **22**, 827-837.

(112) J. Brussee, J. L. G. Groenendijk, J. M. te Koppele and A. C. A. Jansen, *Tetrahedron*, 1985, **41**, 3313-3319.

(113) Y. Guan, Z. Ding and W. D. Wulff, *Chemistry – A European Journal*, 2013, **19**, 15565-15571.

(114) B. M. Panchal, C. Einhorn and J. Einhorn, *Tetrahedron Letters*, 2002, **43**, 9245-9248.

(115) L. Meca, D. Řeha and Z. Havlas, *The Journal of Organic Chemistry*, 2003, **68**, 5677-5680.

(116) Z. Li, X. Liang, F. Wu and B. Wan, *Tetrahedron: Asymmetry*, 2004, **15**, 665-669.

(117) W. J. Newsome, S. Ayad, J. Cordova, E. W. Reinheimer, A. D. Campiglia, J. K. Harper, K. Hanson and F. J. Uribe-Romo, *Journal of the American Chemical Society*, 2019, **141**, 11298-11303.

(118) D. Görl, X. Zhang and F. Würthner, *Angewandte Chemie International Edition*, 2012, **51**, 6328-6348.

(119) S. Huo, P. Duan, T. Jiao, Q. Peng and M. Liu, *Angewandte Chemie International Edition*, 2017, **56**, 12174-12178.

(120) J.-H. Ryu, D.-J. Hong and M. Lee, *Chemical Communications*, 2008, 1043-1054.

(121) A. Kaeser and A. P. H. J. Schenning, *Advanced Materials*, 2010, **22**, 2985-2997.

(122) A. R. West, *Solid State Chemistry and its Applications*, Wiley, 2014.

(123) T. H. Maiman, *Nature*, 1960, **187**, 493-494.

(124) S. Nakamura, T. Mukai and M. Senoh, *Applied Physics Letters*, 1994, **64**, 1687-1689.

(125) G. R. Desiraju, *Journal of the American Chemical Society*, 2013, **135**, 9952-9967.

(126) Y. Zhen, H. Tanaka, K. Harano, S. Okada, Y. Matsuo and E. Nakamura, *Journal of the American Chemical Society*, 2015, **137**, 2247-2252.

(127) S. L. Price, *Proceedings of the Royal Society A: Mathematical, Physical and Engineering Sciences*, 2018, **474**, 20180351.

(128) H. Deng, C. J. Doonan, H. Furukawa, R. B. Ferreira, J. Towne, C. B. Knobler, B. Wang and O. M. Yaghi, *Science*, 2010, **327**, 846.

(129) W. Schrimpf, J. Jiang, Z. Ji, P. Hirschle, D. C. Lamb, O. M. Yaghi and S. Wuttke, *Nature Communications*, 2018, **9**, 1647.

(130) J. Lippke, B. Brosent, T. von Zons, E. Virmani, S. Lilienthal, T. Preuße, M. Hülsmann, A. M. Schneider, S. Wuttke, P. Behrens and A. Godt, *Inorganic Chemistry*, 2017, **56**, 748-761.

(131) M. K. Nayak, *Journal of Photochemistry and Photobiology A: Chemistry*, 2012, **241**, 26-37.

(132) S. Park, J. E. Kwon and S. Y. Park, *Physical Chemistry Chemical Physics*, 2012, **14**, 8878-8884.

(133) J. E. Kwon, S. Park and S. Y. Park, *Journal of the American Chemical Society*, 2013, **135**, 11239-11246.

(134) S. Han, Y. Wei, C. Valente, I. Lagzi, J. J. Gassensmith, A. Coskun, J. F. Stoddart and B. A. Grzybowski, *Journal of the American Chemical Society*, 2010, **132**, 16358-16361.

(135) A. M. Ullman, J. W. Brown, M. E. Foster, F. Léonard, K. Leong, V. Stavila and M. D. Allendorf, *Inorganic Chemistry*, 2016, **55**, 7233-7249.

(136) X. Kong, H. Deng, F. Yan, J. Kim, J. A. Swisher, B. Smit, O. M. Yaghi and J. A. Reimer, *Science*, 2013, **341**, 882.

(137) B. Valeur, *digital Encyclopedia of Applied Physics*, 2009, 477-531.

(138) J. Zhao, S. Ji, Y. Chen, H. Guo and P. Yang, 2011.

(139) J. He, M. Zeller, A. D. Hunter and Z. Xu, *Journal of the American Chemical Society*, 2012, **134**, 1553-1559.

(140) G. Haider, M. Usman, T.-P. Chen, P. Perumal, K.-L. Lu and Y.-F. Chen, *ACS Nano*, 2016, **10**, 8366-8375.

(141) M. Qu, H. Li, Y. Zhao and X.-M. Zhang, *ACS Omega*, 2019, **4**, 3593-3600.

(142) C. Zhou, L. Yuan, Z. Yuan, N. K. Doyle, T. Dilbeck, D. Bahadur, S. Ramakrishnan, A. Dearden, C. Huang and B. Ma, *Inorganic Chemistry*, 2016, **55**, 8564-8569.

(143) D. B. Judd, D. L. MacAdam, G. Wyszecki, H. W. Budde, H. R. Condit, S. T. Henderson and J. L. Simonds, *Journal of the Optical Society of America*, 1964, **54**, 1031-1040.

(144) J. B. T. Azuma, FranceH.D. Einhorn, South AfricaM. Halstead, Great BritainC.W. Jerome, USAJ. de Kerf, BelgiumJ. Krtil, CzechoslovakiaW. Münch, Germany (Chair)J.L. Ouweitjes, The NetherlandsM. Richter, Germany (Secretary)G. Siljeholm, Sweden, *METHOD OF MEASURING AND SPECIFYING COLOUR RENDERING PROPERTIES OF LIGHT SOURCES*, 1995.

(145)   Color Rendering Index For White Light Sources. ,
         http://www.architecturalssl.com/sslinteractive/media/256/ArchLED%20CRI_CQS%20m
         ark.pdf, (accessed 3/2/2020).

(146)   G.-N. Liu, R.-Y. Zhao, R.-D. Xu, X. Zhang, X.-N. Tang, Q.-J. Dan, Y.-W. Wei, Y.-Y.
         Tu, Q.-B. Bo and C. Li, *Crystal Growth & Design*, 2018, **18**, 5441-5448.

(147)   J. Cornelio, T.-Y. Zhou, A. Alkaş and S. G. Telfer, *Journal of the American Chemical
         Society*, 2018, **140**, 15470-15476.

(148)   Y.-D. Yu, L.-B. Meng, Q.-C. Chen, G.-H. Chen and X.-C. Huang, *New Journal of
         Chemistry*, 2018, **42**, 8426-8437.

(149)   G. Hu, G. J. Mains and E. M. Holt, *Inorganica Chimica Acta*, 1995, **240**, 559-565.

(150)   K. A. White, D. A. Chengelis, K. A. Gogick, J. Stehman, N. L. Rosi and S. Petoud,
         Journal of the American Chemical Society, 2009, **131**, 18069-18071.

(151)   Y. Cui, Y. Yue, G. Qian and B. Chen, *Chemical Reviews*, 2012, **112**, 1126-1162.

(152)   K. A. White, D. A. Chengelis, M. Zeller, S. J. Geib, J. Szakos, S. Petoud and N. L. Rosi,
         Chemical Communications, 2009, 4506-4508.

(153)   B. C. McLellan, G. D. Corder, A. Golev and S. H. Ali, *Procedia Environmental Sciences*,
         2014, **20**, 280-287.

(154)   K. P. Carter, A. M. Young and A. E. Palmer, *Chem Rev*, 2014, **114**, 4564-4601.

(155)   N. De Acha, C. Elosúa, J. M. Corres and F. J. Arregui, in *Sensors (Basel)*, 2019, vol. 19.

(156)   L. Feng, H. Li, L.-Y. Niu, Y.-S. Guan, C.-F. Duan, Y.-F. Guan, C.-H. Tung and Q.-Z.
         Yang, *Talanta*, 2013, **108**, 103-108.

(157)   X. Liu, A. Li, W. Xu, Z. Ma and X. Jia, *Materials Chemistry Frontiers*, 2019, 620-625.

(158)   Jangwon Seo, a. Sehoon Kim and S. Y. Park*, *J. Am. Chem. Soc.*, 2004, **126**, 11154-
         11155.

(159)   B. Kaur, N. Kaur and S. Kumar, *Coordination Chemistry Reviews*, 2017, **358**.

(160)   W.-H. Chen, Y. Xing and Y. Pang, *Organic Letters*, 2011, **13**, 1362-1365.

(161)   A. P. d. Silva, T. S. Moody and G. D. Wright, *Analyst*, 2009, **134**, 2385-2393.

(162)   K. Hanson, N. Patel, M. T. Whited, P. I. Djurovich and M. E. Thompson, *Organic
         Letters*, 2011, **13**, 1598-1601.

(163)   C. Ma, Y. Yang, C. Li and Y. Liu, *The Journal of Physical Chemistry A*, 2015, **119**,
         12686-12692.

(164) S. Kataria, L. Rhyman, P. Ramasami and N. Sekar, *Journal of Fluorescence*, 2016, **26**, 1805-1812.

(165) R. Csonka, G. Speier and J. Kaizer, *RSC Advances*, 2015, **5**, 18401-18419.

(166) D. C. Sauer, R. L. Melen, M. Kruck and L. H. Gade, *European Journal of Inorganic Chemistry*, 2014, **2014**, 4715-N4725.

(167) K. Hanson, L. Roskop, N. Patel, L. Griffe, P. I. Djurovich, M. S. Gordon and M. E. Thompson, *Dalton Transactions*, 2012, **41**, 8648-8659.

(168) K. Hanson, L. Roskop, P. I. Djurovich, F. Zahariev, M. S. Gordon and M. E. Thompson, *Journal of the American Chemical Society*, 2010, **132**, 16247-16255.

(169) O. P. Anderson, A. la Cour, A. Dodd, A. D. Garrett and M. Wicholas, *Inorganic Chemistry*, 2003, **42**, 122-127.

(170) W.-H. Chen, Y. Xing and Y. Pang, *Organic Letters*, 2011.

(171) Y. Xu and Y. Pang, *Dalton Transactions*, 2011, **40**, 1503-1509.

(172) W. O. Siegl, *Journal of Organic Chemistry*, 1977, **42**, 1872-1878.

(173) E. Driscoll, S. Sorenson and J. M. Dawlaty, *The Journal of Physical Chemistry A*, 2015, **119**, 5618-5625.

(174) R. Welsch, E. Driscoll, J. M. Dawlaty and T. F. Miller, *The Journal of Physical Chemistry Letters*, 2016, **7**, 3616-3620.

(175) Y. Hao, Y. Zhang, K. Ruan, W. Chen, B. Zhou, X. Tan, Y. Wang, L. Zhao, G. Zhang, P. Qu and M. Xu, *Sensors and Actuators B: Chemical*, 2017, **244**, 417-424.

(176) S. Goswami, K. Aich, S. Das, S. Basu Roy, B. Pakhira and S. Sarkar, *RSC Advances*, 2014, **4**, 14210-14214.

(177) S. Goswami, S. Das, K. Aich, B. Pakhira, S. Panja, S. K. Mukherjee and S. Sarkar, *Organic Letters*, 2013, **15**, 5412-5415.

(178) H.-M. Wen, Y.-H. Wu, Y. Fan, L.-Y. Zhang, C.-N. Chen and Z.-N. Chen, *Inorganic Chemistry*, 2010, **49**, 2210-2221.

(179) J. C. Wang, K. Violette, O. O. Ogunsolu, S. Cekli, E. Lambers, H. M. Fares and K. Hanson, *Langmuir*, 2017, **33**, 9609-9619.

(180) R. R. Gagne, W. A. Marritt, D. N. Marks and W. O. Siegl, *Inorg. Chem.*, 1981, **20**, 3260-3267.

(181) J. S. Renny, L. L. Tomasevich, E. H. Tallmadge and D. B. Collum, *Angew Chem Int Ed Engl*, 2013, **52**, 11998-12013.

(182) W. Chen, S. Chen, B. Zhou, H. Wang, X. Song and H. Zhang, *Dyes and Pigments*, 2015, **113**, 596-601.

(183) I. C. Liverman CT, Fulco CE, et al., editors, *The National Library of Medicine's Toxicology and Environmental Health Information Program*, National Academies Press (US), 1997.

(184) Sarah Garrod, Mary E. Bollard, Andrew W. Nicholls, ‡, Susan C. Connor, John Connelly, §, a. Jeremy K. Nicholson and Elaine Holmes*, 2005, **18**, 115-122.

(185) U. Ragnarsson, *Chem. Soc. Rev.*, 2001, **30**, 205-213.

BIOGRAPHICAL SKETCH

Suliman Al-Hemali Ayad was born to Linda and Hemmali Ayad and raised in Sarasota Florida with three younger sisters. He did the majority of his early education at Pine View School for the Gifted, where in high school he first discovered his love and talent for chemistry. After receiving his high school diploma in June of 2010 he went to the University of Central Florida in Orlando Florida to continue his studies. During his tenure at UCF Suliman worked briefly with the Kuebler and Yuan research groups before settling into the Uribe-Romo group for the last year and a half of his bachelors' education. Upon receiving his Bachelor of Science in December of 2014 Suliman moved to Tallahassee to begin a PhD program in materials chemistry. In November of 2015 Suliman joined the Hanson research group where he conducted the entirety of the work presented in this dissertation.

Outside of his academic life, Suliman has maintained a passion and commitment to community service. At the age of 18 he obtained the rank of Eagle Scout by building a wheelchair accessible deck at the Crowley Nature Museum. While at UCF he served as treasurer, vice president, and president of the Knight Kiteboarding club which regularly orchestrated beach and highway clean up efforts in Cocoa Beach. During his time at FSU Suliman has served as treasurer, president, and vice president of the Cheminoles Graduate Student Association which has participated in community outreach events at science festivals and assisted with judging at local science fairs. From 2018-2020 Suliman founded and spearheaded the Grad Labs program which brought a graduate student volunteer led lab curriculum to Crossroads Academy Charter School.